Forschungszentrum Karlsruhe
in der Helmholtz-Gemeinschaft

Wissenschaftliche Berichte

FZKA 7460

Applied Particle Technology Proceedings of an International Seminar

September 22 – 28, 2008 at the Polytechnical University of Tomsk Russian Federation

H.-J. Ritzhaupt-Kleissl, A. A. Gromov

Institut für Materialforschung

Juli 2009

Forschungszentrum Karlsruhe
in der Helmholtz-Gemeinschaft
Wissenschaftliche Berichte
FZKA 7460

Applied Particle Technology
Proceedings of an International Seminar

September 22 – 28, 2008
at the Polytechnical University of Tomsk
Russian Federation

H. -J. Ritzhaupt-Kleissl
A. A. Gromov
Institut für Materialforschung

Forschungszentrum Karlsruhe GmbH, Karlsruhe
2009

Forschungszentrum Karlsruhe GmbH
Postfach 3640, 76021 Karlsruhe

Mitglied der Hermann von Helmholtz-Gemeinschaft
Deutscher Forschungszentren (HGF)

ISSN 0947-8620

urn:nbn:de:0005-074603

Introduction

The first international seminar “Applied Particle Technology” which took place at Tomsk Polytechnic University in September 2005 was a successful step to improve Russian-German collaboration and scientific progress in the field of heterogeneous systems and processes studies. The idea of such seminar was born as a result of a long-time collaboration in the field of nanopowders between Particle Technology and Fluid Mechanic Department of George-Simon-Ohm University of Applied Science in Nürnberg (Prof. Dr. U. Teipel) and Chemical Engineering Department of Tomsk Polytechnic University (Dr. A. Gromov).

The Second International Seminar “Applied Particle Technology 2008” was planned on the basis of the first seminar results and recommendations and was intended to intensify the international collaboration in the above mentioned field of science and technology. The second seminar gave an overview on the results of mutual and individual research and development activities of the colleagues from Germany, Italy and Russia and became an indicator of the interest and state of the art in the field of nanopowders production, processing, characterization and application. The results of the second seminar not only present a significant and actual impression in the understanding of the chemical and physical nature of nano materials’ processing but also demonstrate the growing of a close and fruitful collaboration between researchers from Western Europe and from Russia.

We would like to thank all the Seminar participants, for their presentations and for the fruitful scientific discussions with their colleagues. We also appreciate the contributions for these Seminar proceedings, thanks to the authors. Special thanks to Jana Herzog (Forschungszentrum Karlsruhe) and Ekaterina Kulinich (Tomsk Polytechnic University) for their kind assistance in the organization and preparation of the Seminar and of the proceedings.

H.-J. Ritzhaupt-Kleissl
A.A. Gromov

- editors -

Synthesis and Processing of New Ceramic Materials

J.R Binder, R. Knitter
Forschungszentrum Karlsruhe GmbH
Institute for Materials Research III
E-mail: joachim.binder@imf.fzk.de

Abstract

Ceramic materials play a key role in many technical fields. The particular importance of synthesis and processing for the fabrication of high quality ceramics is demonstrated here by three very different examples. First of all, some multinary nano-scaled ceramic powders exemplify the possibilities of wet-chemical synthesis methods. The influence of chemical composition and process conditions on the material properties is described for wet-chemical synthesised $Ba_{0.6}Sr_{0.4}TiO_3$ (BST) ceramics. The production of lithium orthosilicate pebbles by melt-spraying as well as their reprocessing is cited as second example. The third part of this short overview deals with the fabrication of dense shrinkage-free ceramics in the System Al_2O_3-SiO_2-ZrO_2, which are produced by reaction-sintering using intermetallic compounds.

Keywords: wet-chemical synthesis, tuneable dielectrics, lithium orthosilicate pebbles, reaction-sintering

Introduction

In a variety of technical applications, tailored ceramics, which are optimized for specific demands, are increasingly gaining in importance. They represent key materials for the realization of many new technologies. Material synthesis is a crucial aspect in the processing of ceramics, which are illustrated in this paper by means of the following three examples:

(I) Wet-chemical synthesis of nano-scaled multinary oxide ceramics

(II) Production of ceramic pebbles by melt-spraying

(III) Fabrication of shrinkage-free ceramics by reaction-sintering

It will be shown, that modern high-performance materials possess their particular properties through the use of synthetic starting materials as well as subsequent processing under controlled conditions.

Wet-Chemical Synthesis of Oxide Ceramics

In order to obtain nano-scaled multinary oxide ceramics of highest quality, a homogeneous distribution of the heterometallic components is crucial, particularly when using dopants. For this purpose, wet-chemical synthesis methods are especially suited. By the use of soluble starting materials, a homogeneous distribution in the molecular range can be achieved. For an optimum quality, it is absolutely essential to retain this homogeneity during the whole process.

In principle two edge cases can be distinguished at solution-based synthesis methods (figure 1). First and foremost there is the solution-sol-gel process (also known as sol-gel process). Hydrolysis, condensation and aggregation reactions lead to colloidal particles (sol) and if they reach macroscopic dimensions, extending throughout the solution, the substance is regarded as a gel. It consists of a continuous solid skeleton with an embedded liquid phase [1]. The formation of corresponding crystalline metal oxides is attained by drying and thermal decomposition of the gel. By contrast, no chemical reactions in the solution take place in the so-called metal-organic decomposition (MOD) process. In this case a rapid drying process is very important in order to avoid the separation of individual components.

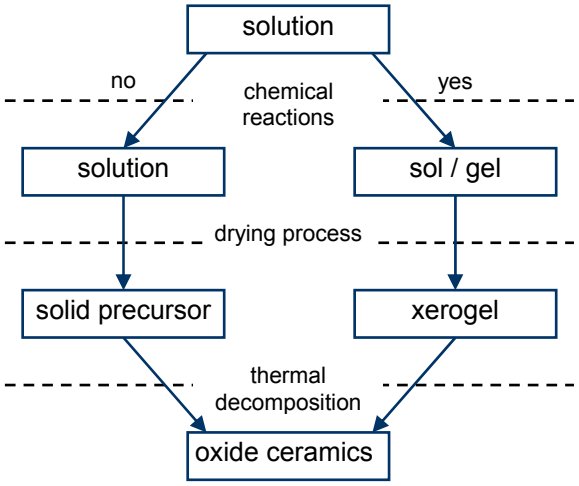

Fig. 1: Schematic diagram of two edge cases of wet-chemical synthesis methods: MOD process (left) and solution-sol-gel process (right).

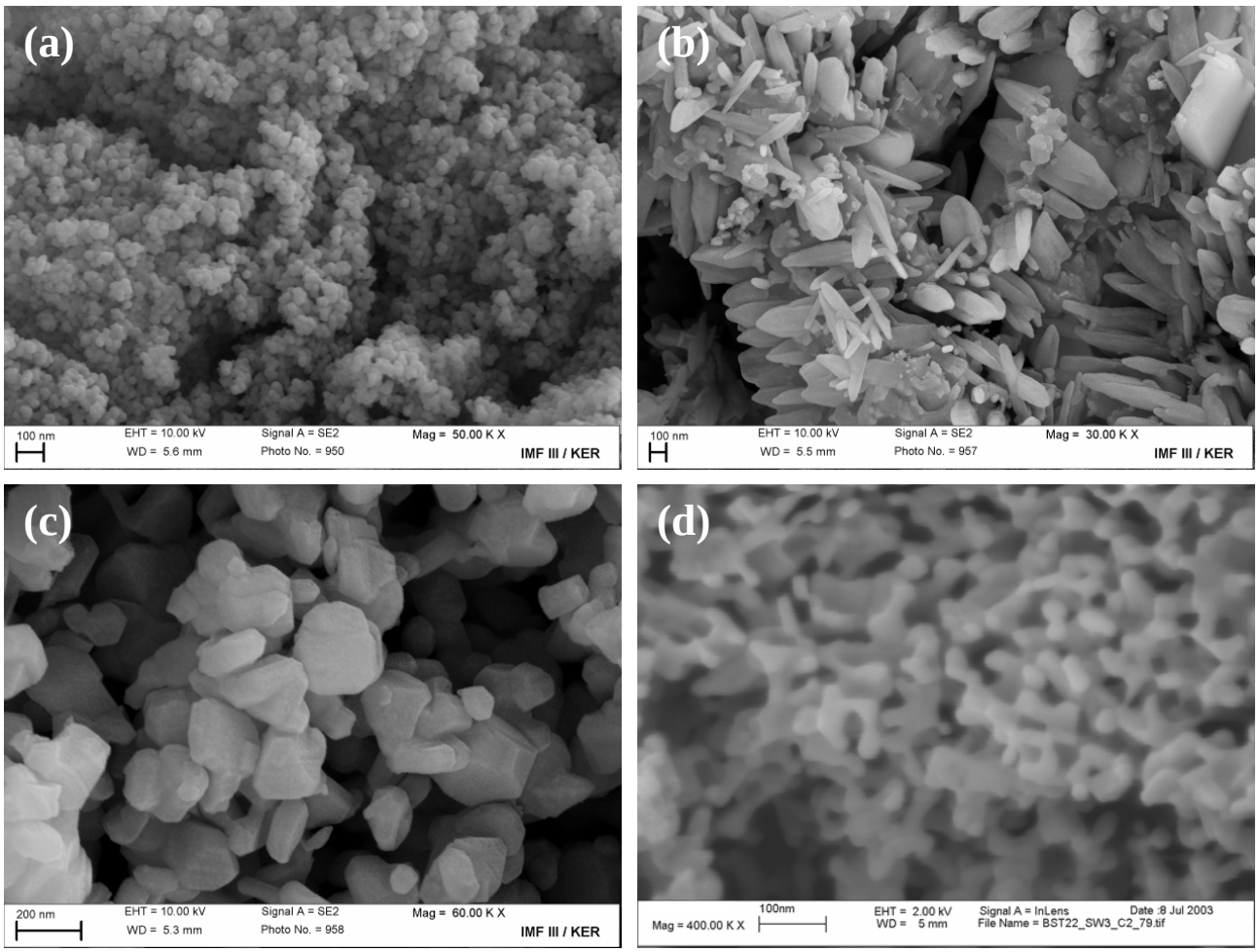

Fig. 2: SEM images of wet-chemically synthesized ceramic powders: (a) $In_{1.76}Sn_{0.18}O_3$, (b) $(Bi,Pb)_2Sr_2Ca_2Cu_3O_{10+x}$, (c) $LiMn_2O_4$, and (d) $Ba_{0.6}Sr_{0.4}TiO_3$.

Figure 2 shows some SEM images of wet-chemically synthesized oxide ceramics. For the synthesis of these powders metal alkoxides, acetates, hydroxides, and/or nitrates are used [2, 3]. The primary particles of the powders vary in size and shape. Nano-scaled multinary oxide ceramics in particular are exemplified in figures 2a and 2d, which display primary particle sizes in the range of 20-50 nm. The corresponding specific surface areas, S_{BET}, are 32 m^2/g ($In_{1.76}Sn_{0.18}O_3$) and 18 m^2/g ($Ba_{0.6}Sr_{0.4}TiO_3$). The primary particle diameters D_{BET} calculated from the specific surface area and the theoretical density ρ, using the equation $D_{BET} = 6 \cdot 10^3/\rho S_{BET}$ (assuming spherical particles), are 26 nm and 58 nm respectively. They are a little higher than the ones estimated from the SEM micrographs due to sintering neck formation during thermal treatment.

The superconducting $(Bi,Pb)_2Sr_2Ca_2Cu_3O_{10+x}$ powder shown in figure 2b points out the complexity of materials, which are available from wet-chemical synthesis methods. Though, it is also possible to synthesize $LiMn_2O_4$ (figure 2c) or more complex $LiAl_xMn_{2-x}O_{4-z}F_z$ spinels, which are promising cathode materials for lithium ion batteries. Through the usage of the dopants like Al^{3+} and F^-, the cycle life of corresponding batteries can be improved [4].

In the field of tuneable dielectrics, the use of dopants also results in a significant improvement of the properties, e.g. the dielectric losses of BST thick films are reduced from 0.078 to 0.022 at 10 GHz by Fe-F-co-doping [5] or even less then 2 % as demonstrated in recent investigations (figure 3). However, the dielectric RF-properties are not only influenced by dopants but also by the morphology. Based on nonlinear 3D FDTD (finite difference time domain) simulations and first experimental studies, the dependency between dielectric performance and the morphology of BST thick films could be shown [6]. The diameter of the sintering necks is a very important parameter. Hence, the performance of porous BST thick films can be enhanced by optimized thermal processing.

Independent from the field of application, whenever the quality of multinary ceramic materials plays a decisive role for the performance of corresponding components or devices, wet-chemical synthesis methods are advantageous for the development and optimization of these complex materials. Yet, for a successful application of new ceramic materials powder conditioning and processing are admittedly at least as important as high-quality synthesis methods.

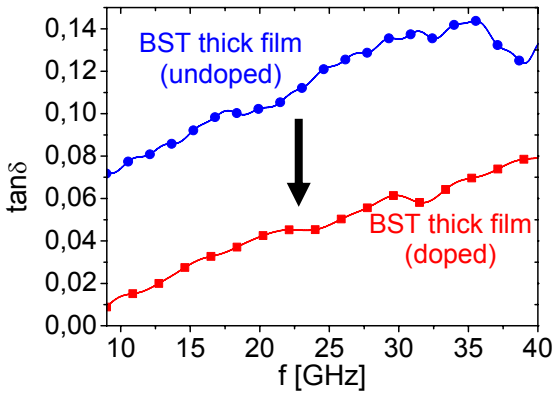

Fig. 3: The dielectric losses of BST thick films can be reduced by using suitable dopants, e.g. with Fe-F-co-doping.

Ceramic Materials for Fusion Technology

Lithium containing ceramics, e.g. lithium orthosilicate (Li_4SiO_4) and lithium metatitanate (Li_2TiO_3), are under development to be used as a tritium source in future nuclear fusion reactors, where the fusion of tritium and deuterium at very high temperatures is expected to gain a high excess of energy. As an unstable isotope of hydrogen, tritium has to be produced inside the reactor under neutron irradiation by the transmutation of the lithium-6 isotope into tritium and helium.

In the present design of the so-called solid breeder concept, lithium ceramics will be inserted in the plasma surrounding blanket modules as pebble beds with pebble diameters ≤ 1 mm. While most approaches to fabricate ceramic pebbles are based on powder technology or sol-gel methods [7], a melt-spraying process has been developed in cooperation with Schott AG (Mainz, Germany) to produce lithium orthosilicate pebbles [8]. These pebbles were chosen as a possible tritium breeder material for the European Helium Cooled Pebble Bed (HCPB) blanket, which will be tested in the international fusion device ITER that is under construction in Cadarache, France [7, 9].

Fig. 4: Lithium orthosilicate pebbles with sizes of 250-630 µm fabricated by melt-spraying.

The lithium orthosilicate pebbles with a surplus of 2.5 wt% SiO_2 are fabricated by melting a mixture of lithium hydroxide hydrate and silica powders and then spraying the liquid material in air [8]. The sprayed droplets solidify during the flight and result in pebbles with a broad size distribution and sizes up to ca. 1 mm. As only pebbles with a diameter in the range of 250–630 µm (figure 4) have been selected for the use in the blanket, the yield of the melt-spraying process is only about 50 wt%.

Due to the surplus of SiO_2 and the rapid quenching of the droplets, the as prepared pebbles consist of Li_4SiO_4 as the main phase and the metastable high-temperature phase $Li_6Si_2O_7$ as a minor phase. The high-temperature phase is decomposed into the thermodynamically stable phases lithium ortho- and metasilicate (Li_2SiO_3) during a subsequent thermal annealing step at 970°C (figure 5). The melt-spraying also generates some pebbles, especially with very small diameters, which solidify amorphously and crystallize only during thermal annealing.

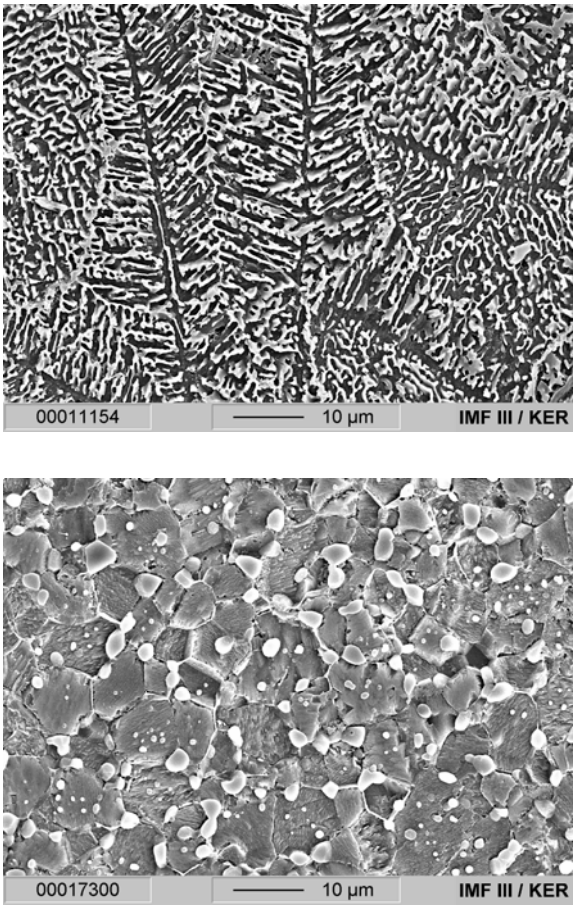

Fig. 5: Microstructure of lithium orthosilicate pebbles at etched cross-sections (SEM), top: dendritic solidification microstructure of Li_4SiO_4 (dark) and $Li_6Si_2O_7$ (light) of the initial pebbles, bottom: microstructure of thermally annealed pebbles with ~10 µm grains of Li_4SiO_4 (dark) and smaller inclusions of Li_2SiO_3 (light).

A detailed quality control of these pebbles, comprising chemical and phase analysis, measurement of density and porosity as well as mechanical properties, is carried out before the material is used in any experiment to investigate the irradiation behaviour, the tritium release or the thermomechanical performance of the pebbles.

For the application of these breeder materials in future fusion technology, the recycling is an important issue due to the high costs of Li-6-enriched materials as well as waste considerations. For lithium orthosilicate pebbles, fabricated by a melt-spraying process, the direct remelting without any additional wet-chemical recycling step has been proposed as a facile reprocessing process [8].

Restrictions for the reprocessing follow from the activation of the material under neutron irradiation. It has been shown that impurities like Al and traces of Co, originating from the raw materials, as well as impurities of Pt from the crucible may dominate the long-term activation [10]. To limit the possible activation, very pure raw materials should be used and any contaminations by processing or handling have to be reduced as far as possible.

Reaction-sintered Ceramics

In contrast to the above mentioned methods for the synthesis of ceramic powders and pebbles, this topic describes an alternative ceramic processing method for the fabrication of dense shrinkage-free ceramic parts. Compared to conventional ceramic processing routes, the so-called reaction-sintering techniques allow the minimization or compensation of the inevitable sinter shrinkage by volume expansion reactions. Intermetallic compounds such as $ZrSi_2$, Zr_2Si or $ZrAl_3$ are especially suited to produce reaction-sintered ceramics in the system Al_2O_3-SiO_2-ZrO_2. Due to their high volume increase during oxidation in comparison to pure metals (table 1), intermetallic phases enable the fabrication of dense, true net-shape sintering ceramic parts, i.e. after sintering they exhibit exactly the same dimension and shape as in the green state, which is exemplary shown in figure 6 for ceramic nuts.

Tab. 1: Oxidation reactions of Al, $ZrAl_3$, Zr_2Si, and $ZrSi_2$ and their relative increase in volume.

	rel. change in volume
$2\ Al + 3/2\ O_2 \rightarrow Al_2O_3$	29 %
$2\ ZrAl_3 + 13/2\ O_2 \rightarrow 2\ ZrO_2(t) + 3\ Al_2O_3$	42 %
$Zr_2Si + 3\ O_2 \rightarrow ZrSiO_4 + ZrO_2(t)$	71 %
$ZrSi_2 + 3\ O_2 \rightarrow ZrSiO_4 + SiO_2(c)$	121 %

t: tetragonal modification; c: cristobalite

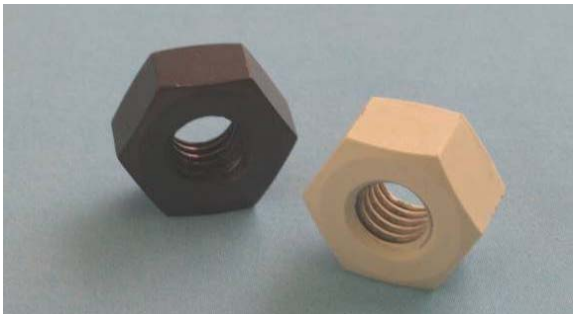

Fig. 6: Ceramic nuts manufactured by mechanical machining methods, before reaction-sintering (left) and after (right).

Besides the well investigated green machining techniques [11-13], there are some other shaping processes such as pressing, embossing, electrophoretic deposition, or injection moulding, which are generally suited to produce shrinkage-free ceramics. The drawbacks and possibilities are described in detail in [14]. Independent from the shaping process, the basic conditions to realize zero-shrinkage can be calculated according to the following equation:

$$\Delta\tilde{V} = (1 + \Delta\tilde{m}) \cdot \frac{\rho_{green\,compact}}{\rho_{ceramic}} - 1$$

with

$\Delta\tilde{V}$: relative volume change (-)

$\Delta\tilde{m}$: relative weight change (-)

ρ : green and sinter density (g/cm^3)

There is one obvious condition that has to be fulfilled to exactly compensate the sintering shrinkage during thermal processing and to achieve true net-shape ceramic parts. The green density has to be adjusted to the ratio of sinter density to the relative weight change:

$$\rho_{green\,compact} = \frac{\rho_{ceramic}}{(1 + \Delta\tilde{m})}$$

This ratio is predominantly given by the composition of the starting materials. This largely applies also for the microstructure and material properties. By using the above mentioned intermetallic compounds as well as suitable metal oxides such as ZrO_2, Y_2O_3, or Al_2O_3, ceramic materials in the phase fields of the ternary system Al_2O_3-SiO_2-ZrO_2 can be produced. These varying ceramics possess different material properties. For instance the mechanical strength varies between 300 MPa for zircon-based ceramics and approximately 630 MPa for mullite-zirconia or AMZ (alumina-mullite-zirconia) ceramics depending on the composition of the starting materials and the processing conditions [15-17]. Figure 7 shows the microstructure of AMZ ceramic with submicron-sized ZrO_2 and Al_2O_3 grains and the elongated

morphology of the mullite particles. For reaction-sintered ZTA (zirconia toughened alumina) ceramics flexural strength values up to 780 MPa could be reached [17], but up to now no true net-shape ZTA ceramics with this high flexural strength could be realized. For this purpose a further material and process development is absolutely essential.

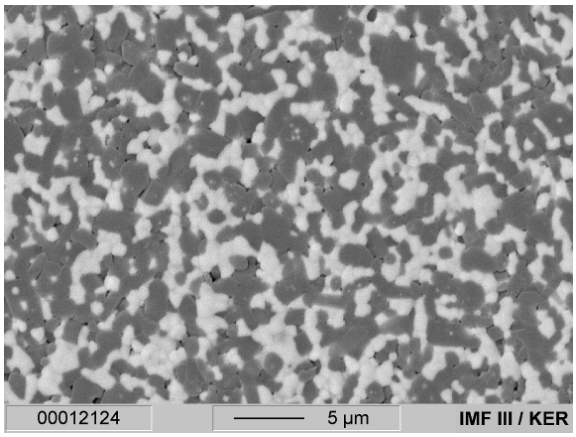

Fig. 7: SEM image (material contrast) showing the microstructure of a reaction-sintered Al_2O_3-mullite-ZrO_2 ceramic; composition: the dark grey phases are alumina (roundish) and mullite (elongate) and the light grey phase is zirconia.

Conclusions

All three examples demonstrate the particular importance of the interplay of synthesis and processing in order to develop new advanced materials. A high-quality synthesis is needed for very different reasons, to achieve improved physical properties, to avoid activation, or to gain net-shape sintering. Yet in all cases a proper processing is additionally necessary to realize the desired performance of the material.

References

[1] C. J. Brinker, and G.W. Scherer, *Sol-gel science: the physics and chemistry of sol-gel processing*, Academic Press, San Diego 1990.

[2] E. Günther, and R.A. Dorey, *Wet chemical synthesis for multinary oxide ceramics*, in H.-J. Ritzhaupt-Kleissl, and P. Johander (eds.), *Ceramic processing in microtechnology*, Whittles Publishing, in press.

[3] F. Paul, J.R. Binder, H. Gesswein, H.-J. Ritzhaupt-Kleissl, and J. Hausselt, *Synthesis of doped $Ba_{0.6}Sr_{0.4}TiO_3$ ceramic powder via a sol-freeze-granulation and freeze-drying process*, Ceram. Intern. **35** (2009) 479-486.

[4] G.G. Amatucci, and N. Pereira, *Fluoride based electrode materials for advanced energy storage devices,* J. Fluorine Chem. **128** (2007) 243-262.

[5] F. Paul, A. Giere, W. Menesklou, J.R. Binder, P. Scheele, R. Jakoby, and J. Haußelt, *Influence of Fe-F-co-doping on the dielectric properties of $Ba_{0.6}Sr_{0.4}TiO_3$ thick-films*, Int. J. Mat. Res. **99** (2008) 1119-1128.

[6] A. Giere, X. Zhou, F. Paul, M. Sazegar, Y. Zheng, H. Maune, J.R. Binder, and R. Jakoby, *Barium strontium titanate thick-films: dependency between dielectric properties and their morphology*, Frequenz **62** (2008) 47-51.

[7] A. Ying, M. Akiba, L.V. Boccaccini, S. Casadio, G. Dell'Orco, M. Enoeda, K. Hayashi, J.B. Hegeman, R. Knitter, J. van der Laan, J.D. Lulewicz, and Z.Y. Wen, *Status and perspective of the R&D on ceramic breeder materials for testing in ITER*, J. Nucl. Mater. **367-370** (2007) 1281-1286.

[8] R. Knitter, and B. Löbbecke, *Reprocessing of lithium orthosilicate breeder material by remelting*, J. Nucl. Mater. **361** (2007) 104-111.

[9] http://www.iter.org/

[10] R. Knitter, U. Fischer, S. Herber, and C. Adelhelm, *Reduction of impurities and activation of lithium orthosilicate breeder materials*, J. Nucl. Mater. **386-388** (2009) 1071-1073.

[11] H.-J. Ritzhaupt-Kleissl, J.R. Binder, Th. Gietzelt, and J. Kotschenreuther, *Net shape reaction bonded ceramic micro parts by mechanical microstructuring,* Adv. Eng. Mater. **8** (2006) 983-988.

[12] J.R. Binder, N. Schlechtriemen, S. Jegust, A. Pfrengle, H. Geßwein, and J.-H. Ritzhaupt-Kleissl, *Green machining of net-shape reaction-bonded ceramics: materials and applications*, cfi/Ber. DKG **84** (2007) E57-E60.

[13] A. Pfrengle, J.R. Binder, H.-J. Ritzhaupt-Kleissl, J. Haußelt, C. Müller, and Th. Gietzelt, *Optimizing net-shape ceramics for green machining*, Int. J. Appl. Ceram. Technol., accepted.

[14] J.R. Binder, R.A. Dorey, M. Müller, H. Geßwein, S.A. Rocks, and D. Wang, *Near net shaping of ceramics in microsystems technology*, in H.-J. Ritzhaupt-Kleissl, and P. Johander (eds.), *Ceramic processing in microtechnology*, Whittles Publishing, in press.

[15] H.-J. Ritzhaupt-Kleissl, J.R. Binder, E. Klose, and J. Haußelt, *Net-shape ceramic microcomponents by reaction bonding*, cfi/Ber. DKG **79** (2002) E9-E12.

[16] H. Geßwein, J.R. Binder, H.-J. Ritzhaupt-Kleissl, and J. Haußelt, *Fabrication of net shape reaction bonded oxide ceramics*, J. Eur. Ceram. Soc. **26** (2006) 697-702.

[17] H. Geßwein, *Entwicklung hochfester Net shape Oxidkeramiken im System Al_2O_3-SiO_2-ZrO_2*, PhD thesis, University of Freiburg (2005).

Ceramics Processing in Microtechnology

H.-J. Ritzhaupt-Kleissl
Forschungszentrum Karlsruhe GmbH, Institut für Materialforschung III
P.O. Box 3640, D-76021 Karlsruhe, Germany
Phone: +49 7247 823727; Fax: +49 7247 824612; E-mail: ritzhaupt-kleissl@imf.fzk.de

Abstract

Besides polymers and metals ceramics play an important role in microtechnology because of their outstanding properties. They are not only characterized by high hardness, wear resistance, high temperature stability and chemical inertness, but ceramics also show special functionalities, e.g. sensor and actuator properties, ferroelectricity or electric conductivity ranging from insulators via semiconductors to metal-like conductors. Special material development is necessary nevertheless, to meet the requirements of microtechnology. This is especially true for the synthesis of multinary oxides as functional ceramics or for new net shape ceramic materials, which compensate the sintering shrinkage by a reaction bonding process. Ceramic processing also bears challenges in order to meet the microstructural, dimensional and accuracy requirements of microtechnology. Standard shaping processes have to be focussed to the fabrication of microparts, or even new processes have to be established. A further aspect is the design of ceramic microcomponents, which requires approaches quite different from designing polymer or metal microparts. As a resume the development of ceramic microcomponents requires research and development in the field of materials research as well as in processing and designing of the components. These development areas are obviously strongly interconnected with each other. The current contribution will give an overview over the research work performed in these fields in the Institute for Materials Research III at the Forschungszentrum Karlsruhe.

Key Words: Ceramics, synthesis, sol-gel, nanopowders, ferroelectrics, mesoporous granulates, electroconductive ceramics, microheaters, reaction bonding, net-shape ceramic, ceramic processing, ceramic injection molding, HPIM, LPIM, microcomponents, micro reactor, PZT, micro turbine.

1 Introduction

Besides polymers and metals there is an increased importance of ceramic materials in modern technology. This is because of their outstanding properties, such as hardness, high-temperature applicability, abrasion resistance and chemical inertness. But also outstanding physical properties such as di-, ferro- and piezoelectricity as well as conductivity and sensor properties open a wide field of application for modern ceramic materials. Taking into account the need for miniaturization of technical devices and the growth of Microsystem Technology (MST) there is an increasing requirement for ceramic microcomponents like microparts or microstructured parts. Examples of ceramic microcomponents are high precision parts for medical and dental application with tolerances in the micrometer range, microstructured piezo components, gas sensors or parts for micro reaction technology. To meet these requirements it is necessary to develop new materials and to establish new manufacturing routes and so to generate ceramic components in microdimensions, or with microdetails or with accuracies in the micrometer range. This is still more important as a final shaping or finishing of the microcomponents after the molding and sintering processes is either very expensive or even technically impossible.

There is great challenge in order to meet these microstructural, dimensional and accuracy requirements. Molding processes have to be developed further for the fabrication of microcomponents, or even new processes have to be established. An additional aspect is the design of ceramic microcomponents, which requires approaches quite different from designing polymer or metal microparts. Experience shows that the mentioned development areas are strongly interconnected with each other, making it sometimes necessary to establish an integrated line from material development via processing to component design.

2 Material development

2.1 Nanopowder synthesis

Although powder-free fabrication routes exist for the generation of small-sized ceramic parts, e.g. routes

based on preceramic polymers, which can be lithographically structured [1, 2], the great majority of ceramic parts is made by powder technology.
This is why powder synthesis and processing is of great importance for ceramic technology. Especially in the field of microtechnology where development tends towards smaller parts and finer details there is an urgent need for still finer and more homogeneous powders. Nanopowders, which are aimed at opening new fields of technology due to their unique properties, are nowadays either already commercially available or in different states of development at many research institutions. The most important processes for the production of ceramic nanopowders are gas phase syntheses, wet chemical or laser ablation processes.

Gas phase processes, including flame pyrolysis and chemical vapor synthesis, lead to nanopowders which are often highly agglomerated. There are process modifications, however, where almost agglomeration-free powders can be synthesized [3]. With the so-called Karlsruhe microwave-plasma gas process not only agglomeration can be avoided but also nanocomposite powders with interesting physical properties can be synthesized, the ceramic particles being coated in situ with an additional ceramic or polymer layer [4]. The agglomeration tendency can also be reduced by the laser ablation process as was shown e.g. for ZrO_2, [5, 6].

Other methods to produce submicron to nanosized ceramic powders are chemical syntheses, mainly based on sol-gel or sol-gel related processes. These methods are especially appropriate for the synthesis of high quality functional ceramics, which are mainly multinary oxide ceramics. For these materials the most homogeneous distribution of the constituents including even very small quantity of additives is of high importance for their functionality. This fact favors the use of liquid educts because herewith a homogeneous element distribution down to the molecular region is possible. By sol-gel or sol-gel related processes ceramic powders can be derived whose primary particles are nanosized but which also can be handled rather conveniently. One example is the sol-gel synthesis of a nanoscale ferroelectric ceramic on barium-strontium-titanate basis with Fe- or Ta-additives in the tenth-percent region in order to improve their properties [7, 8]. The process is as follows: The liquid precursors are mixed, followed by spray freezing and freeze drying. This intermediate freeze dried granulate is then calzined. Though the resulting ceramic powder, with a particle size of about 40 nm, is agglomerated as can be seen in fig.1, the agglomerates can easily be destroyed by ultrasound agitation. From these powders screen printing pastes are fabricated and microstructured thick-film patterns are printed (fig.2) e.g. as tunable elements for microwave antenna application.

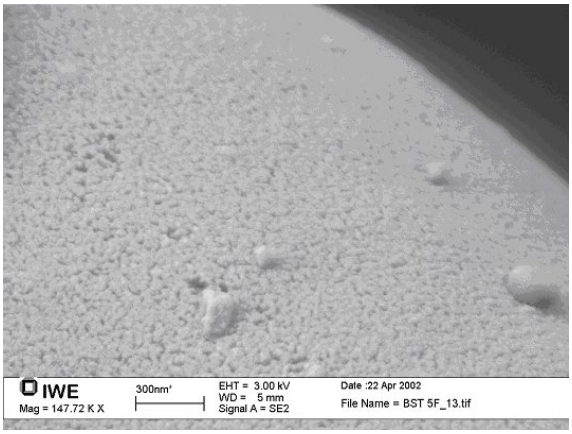

Fig. 1: Surface of Nano-$Ba_{0.6}Sr_{0.4}TiO_3$ (BST) powder [8].

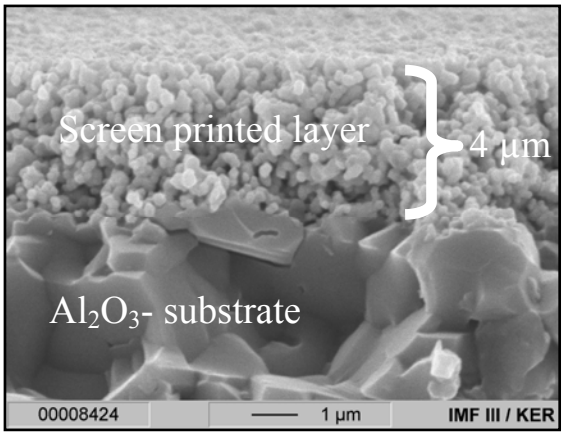

Fig. 2: BST-layer from nanoscale powder screen printed on an Al_2O_3-substrate [8].

A sol-gel related process is the Thermal Two Stage Process for the synthesis of multinary oxide ceramic powders [9, 10]. Comparable to sol-gel processing the educts are liquid metal precursors, mainly alcoholates or acetates. They are intensively mixed followed by spray drying in order to produce a solid granulate. In a second step this intermediate, still organic granulate is then ceramized in a fluidized bed furnace. A lot of multinary oxide ceramics have been synthesized by this process, such as lead zirconate-titanate (PZT) [11], lead niobate (PN) [12], indium-tin oxide (ITO) and others [10]. Besides the already mentioned homogeneous distribution of the constituents in the powder there are still other advantages of

this type of process. Though the resulting product shows the typical structure of a spray dried powder with a granulate size of about 20 – 50 µm, the size of the primary particles is in the nanometer range and the granulate is so soft agglomerated that these agglomerates can be easily destroyed by further processing, e.g. when preparing an injection molding feedstock, a screen printing paste or a slurry for tape casting. Due to the final treatment in the fluidized bed furnace there is no baking together of the single granulates. They are very smoothly flowing, e.g. into a mold for compaction by dry pressing. Because of the fine particle size sintering is improved and especially for the ITO-powder pressureless sintering is possible.

2.2 Mesoporous granulates for composites

Agglomerated ceramic nanopowders as they are commercially available can also be useful for microtechnical or medical applications. One example is the preparation of mesoporous granulates [13, 14, 15]. Starting with sols of pyrogenic silicid acid these mesoporous granulates with tailored properties can be generated by a modified sol-gel process and final spray drying. The types of Aerosil® used in this process define the structure of the open porosity, i.e. dependent of different Aerosils® porous granulates with different pore radii in the region of about 10 nm to 50 nm can be realized, see fig.3. Furthermore, pore diameter, amount of porosity and granulate diameter can be controlled by the processing conditions. These porous granulates can be used as anorganic filling materials in organic matrix composites. Hereby the organic matrix material can pour into the open porosity and in this way leads to a mechanical interlocking between the matrix and the filling material. It could be shown that this results to an improved abrasion resistance of the composite. As it is furthermore possible to vary the refractive index of the granulates e.g. by adding elements with higher refractive indices to the SiO_2-sol, as it has been realized by addition of defined amounts of zirconia sol, the refractive index of the anorganic component of the composite can be adjusted to that of the organic matrix, giving transparent or translucent ceramic-polymer composites as it is shown in fig.4.

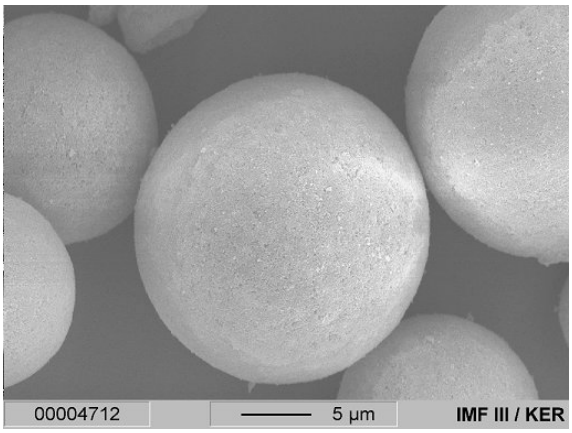

Fig. 3: Ceramic granulates with monomodal open porosity in the nanometer range [13].

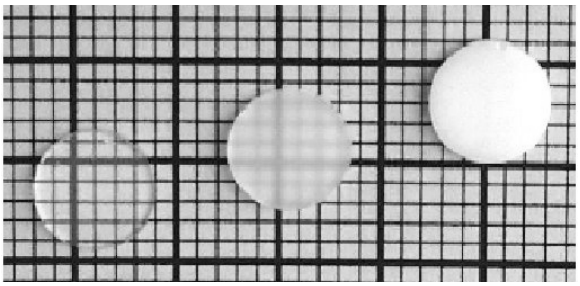

Fig. 4: Ceramic-polymer composites with adjustable refractive index [13].

Composites like these can be structured by the standard microstructuring techniques available for polymer microstructuring. The mentioned characteristics and advantages of these composites could be made apparent for a special medical application, i.e. for dental restoration. During the development of dental filler materials it was possible to realize composite fillers with an anorganic amount of about 25 vol% showing the translucent characteristic of natural teeth and also showing increased abrasion resistance.

2.3 Electroconductive ceramics

A more conventional method is performed for the generation of an electroconductive ceramic of the basis of Al_2O_3-TiN (ATN) or Si_3N_4-TiN /SNTN) [16, 17], i.e. the mixture of a metal-like electric conductor – TiN – and an isolator. Here the single constituents are intimately mixed in a planetary ball mill. There are several advantages of this type of material, especially for microcomponents. The resistivity of the material can be individually adjusted over several orders of magnitude by simply adjusting the conduc-

tor/isolator ratio. Gradient materials can easily be realized. This is important e.g. for microheaters, as the heated zone can be locally defined not by changeing the cross section as it is commonly done and might be sometimes difficult for microparts, but by locally adjusting the composition. A physical advantage is the metal-like characteristic of the resistivity, which is linearly increasing with temperature (PTC-characteristic). This enables a rather easy controlling behaviour. A favorable processing aspect is the sinterability of this material. Pure TiN cannot be compacted to reasonable densities by sintering without an additional external pressure. The ATN- and SNTN-mixtures, however, can be sintered though under cover gas atmosphere but at ambient pressure. Further processing can be done by dry pressing of the powder, e.g. for ceramic heaters/igniters for automotive application (see fig. 5 right), by fabrication of a screen printing paste and screen printing of microelement, (fig. 5 left) or by setting up a ceramic feedstock for injection molding [18]. As TiN oxidizes in open air at temperatures higher than about 400°C a protective coating is necessary for high temperature operation. This can be achieved by coating the components with an alumina layer, e.g. by dipping in an alumina suspension or by simply painting with a suspension. Cracking of the protective layer during operation is avoided, because Al_2O_3 and TiN have nearly the same thermal expansion coefficient.

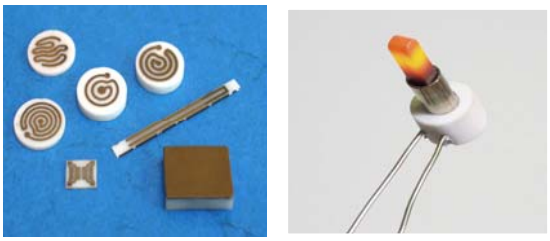

Fig. 5: Types of ceramic microheaters: screen printed patterns on ceramic substrates (left), heating plug in operation at about 1200°C (right)

2.4 Net shape ceramics by reaction bonding

One of the main disadvantages of ceramic components, especially in microtechnology, is their shrinkage during sintering. Up to 20% linear shrinkage is typical. To obtain the required component size after sintering, the green body must be formed with correspondingly larger dimensions or there must be some finishing after sintering, i.e. in the sintered, hard state. Although compensation of the shrinkage and thus net-shape sintering are state of the art in large scale production, for narrow dimensional tolerances, final shaping by e.g. grinding is still necessary after sintering. In the case of ceramic microcomponents, with minimal detail dimensions in the range of certain micrometers such finishing is extreme difficult and expensive, if not completely impossible. One potential solution for this problem is provided by reaction bonding. In this process precursors of the required ceramic are transformed into the ceramic by an additional reaction during the sintering process. If the precursors are selected to ensure the reaction product has a larger volume than the starting components, it is possible to compensate for the inevitable shrinkage in order to obtain dense and net-shape ceramic microcomponents. It has been shown that reaction bonding techniques such as Reaction Bonding of Alumina (RBAO) or the Reaction Bonding of Mullite (RBM) are interesting alternative ceramic processing methods offering some advantages compared to conventional processing routes. One of the greatest advantages is the possibility to generate ceramics with low to zero shrinkage during sintering [19 – 21].

Intermetallic phases e.g. the silicides of titanium and zirconium offer a great potential as anorganic precursors for reaction bonding as they show, compared to metallic precursors, a rather large volume increase combined with a well controllable oxidation reaction.

For example, according a summary reaction equation for the oxidation of zirconium disilicide, $ZrSi_2$, yields:

$$ZrSi_2 + 3O_2 \rightarrow ZrO_2 + 2\ SiO_2 \quad \text{or}$$
$$ZrSi_2 + 3O_2 \rightarrow ZrSiO_4 + SiO_2$$

This reaction results in a volume increase of about 100% from 1 cm³ $ZrSi_2$ to 2 cm³ ($ZrSiO_4 + SiO_2$). So, when starting with a defined green density, which is relatively easy to obtain, e.g. by powder pressing, shrinkage can be compensated and exact net shape ceramic components can be achieved after sintering.

$ZrSiO_4$, which results from the reaction, is better known as a gemstone – zircon – than as an engineering ceramic. Its density is about 4,70 g/cm³ and it has a very low linear thermal expansion coefficient of about 4x10-6 K-1. Mori [22] measured bending strengths of around 400 MPa and crack toughness values in the range of 3.4-4 MPa√m, the Youngs modulus is 130 GPa [23] and the Vickers hardness is about 1300 HV. Different compositions of the sintered ceramic - pure $ZrSiO_4$ or $ZrSiO_4$-ZrO_2 composites – can be achieved by adjusting the Zr/Si ratio, i.e. by adding ZrO_2 to the precursor. Though the result of the addition of "inert" ZrO_2 leads to a reduced volume increase and must be compensated by a higher green density, the mechanical properties of the ceramic can be improved, resulting in bending strengths of about 350-400 MPa.

Another aspect which must be taken into account in the course of ceramic processing are organic pressing aids and binders, which are added to the starting powder in order to improve shaping and processing. Generally, these organics must be burnt out during the sintering process. They do not contribute to densification during sintering. On the contrary, they cause new pores after their burnout also influencing the volume change when they are removed. The use of so-called "low loss binders" improves the situation as they take part in the reaction and ceramize to a certain extent. For example, a certain polysiloxane as a low-loss binder yields about 80% ceramic, i.e. after oxidation about 80% of this organic is transformed to SiO_2, which again together with ZrO_2 can react to $ZrSiO_4$.

The complete thermal process consists of three steps: pyrolysis of the low-loss binder, oxidation i.e. the expansion of the intermetallic phase and the sintering step. Fig. 6 shows a schematic view of the reaction process and the associated length change of a sample.

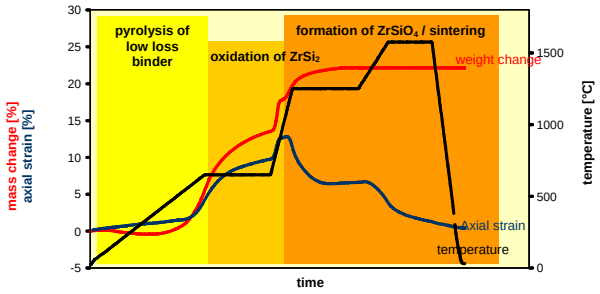

Fig.6: Reaction bonding process for the $ZrSiO_4$-based ZircoDur® ceramic [28].

A further beneficial effect of the binder addition is that this material can be mechanically microformed well in the green state either by turning or milling with standard hard-metal tools or by embossing with a (microstructured) die. Intensive studies have been performed in the last years to develop a $ZrSiO_4$-based non-shrinking ceramic material together with the appropriate microforming technologies [24-28]. Besides the compliance with the high accuracy zero-shrinkage characteristics in order to meet microtechnical requirements, special emphasis was laid on relevant processing routes. These developments resulted in the microstructuring of green blanks either by embossing by a microstructured die, which is appropriate for components with low aspect ratios, or in mechanically microstructuring the green blanks, e.g. by micromilling. The technique last mentioned is very favorable, as it allows the fabrication of real net shape 3-dimensional microparts in any shape.

Current studies [29] show that also zero-shrinkage mullite-ZrO_2 composites can be synthesized from the appropriate intermetallic phases $ZrAl_3/ZrO_2$ and $ZrAl_3/ZrSi/ZrO_2$. Noticeably higher strengths up to about 630 MPa could be realized with these ceramics.

The possibility to shape these types of ceramics in the green state with high accuracy to the final dimensions opens up interesting fields of application. Among these are, besides universal application in microtechnology, especially applications in medical or dental technologies. As examples figs.7 and 8 show parts from this ZircoDur® material in the green and in the sintered state, shaped in the green state by embossing (fig 7) and dental crowns shaped by micromilling (fig. 8).

Fig.7: ZircoDur®-replicas of a coin (upper left) by embossing showing the green body (upper right) and the sintered part (bottom).

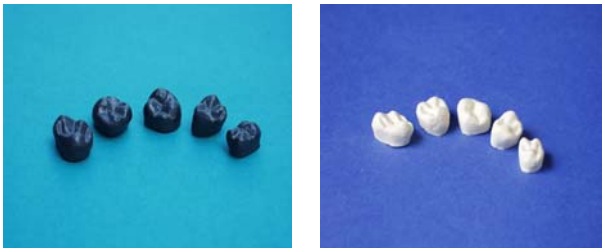

Fig.8: Ceramic dental crowns milled in the green state (left) and sintered net shape with µm accuracy (right) [28].

3 Processing routes for the fabrication of ceramic microcomponents

3.1 General aspects

Apart from the above mentioned microforming by mechanical machining, ceramic forming is mostly performed by replication techniques. These techniques have in common that ceramic replicas are generated by filling molds, while the mold materials and the method how the molds or the original masterpatterns are fabricated may differ. For replication the ceramic material must be in a moldable state, i.e.

- it must fill the mold completely down to details in the micrometer range
- it must be consolidated in the mold
- it must be demoldable after filling so that the structured details are kept and not destroyed
- it must be sinterable to the desired density without cracking or fragmentation.

These requirements can best be met by colloidal techniques [30, 31, 32]. Various replication techniques have been developed for the fabrication of ceramic microparts [33], e.g. gelcasting [34, 35], soft molding [36], direct coagulation casting (DCC) [37], tape casting [38, 39], screen printing [40, 41], electrophoretic deposition (EPD) [42, 43, 44], lithographic structuring of pre-ceramic polymers [1, 2, 45] etc. Among these techniques micro ceramic injection molding (MicroCIM) is of great interest for economic production with available equipment.

3.2 Micro Powder Technology

One of the reasons for the development of powder injection molding (PIM) for microparts is the fact that conventional, i.e. macroscopic PIM is a widespread manufacturing technology for metallic and ceramic parts. As another advantage this technique can cover the whole field from development studies, prototyping or small number fabrication to medium or large scale series production. This is enabled by the fact that there are two variants of ceramic injection molding which are both suitable for the fabrication of ceramic microcomponents: low pressure injection molding (LPIM), also called hot molding, and the more well-known high pressure injection molding (HPIM). While for macroscopic parts the entire process chain is well established, new challenges arise with respect to the miniaturization of PIM for applications in microtechnology. Generally injection molding consists of the following process steps: feedstock preparation, injection molding, debinding and sintering.

Feedstock preparation is an essential step because very fine ceramic powders are necessary for MicroCIM. With only very few exceptions the powders in commercial feedstocks are too large. Because of the small cross sections of micro-parts and their high surface-to-volume-ratio, wall friction during mold filling and demolding becomes important and requires low viscosity for mold filling, and high strength feedstocks and perfectly smooth tool inserts for demolding. For a perfect flow of a feedstock during mold filling each particle has to be completely coated with binder. So with decreasing powder particle size the viscosity of a feedstocks sharply increases and the maximum powder fraction in the feedstock significantly decreases. As in CIM the powder content in the feedstock is identical to that in the green part, a reduction of the particle size inevitably results in a reduced green density and in a reduced density after debinding. Therefore the shrinkage during sintering to full density is increased [46]. Thus, despite the fact that sub-µm-powders are desirable for µCIM the usage of nanopowders with particle sizes below 100 nm seems to be limited.

3.3 Injection molding

To meet all these requirements the feedstocks for MicroPIM consist of fine powders and a multicomponent binder system. For the mass production (HPIM) of microparts or micropatterned parts, they contain a significant amount of at least one thermoplastic component providing sufficient green strength for a damage-free demolding of the green parts. They are often combined with waxes and further additives to form binder systems consisting of at least 3 components [47]. These binder systems are preferred to realize a stepwise debinding process in order to avoid stress in the green compacts during debinding. The waxes reduce the feedstock's viscosity for a complete mold filling [48] and provide a better debinding behavior [49, 50]. Improved wetting of the polar surfaces of ceramic powders with the non-polar binder can be achieved by using surfactants.

For mold filling the micropatterned mold inserts with high aspect ratios are heated to temperatures often above the melting points or even above the no-flow temperatures of the molding materials. As a consequence of the thin walls and large surfaces of micropatterns compared to their volume the temperature of the molding materials adapts to that of the mold within milliseconds. Despite the fact that binders have a low thermal conductivity and usually show a „self-isolating" effect, the injected materials would freeze on the molding tool's wall and the microcavities would not be filled completely. Therefore the mold and the feedstock have to be heated to achieve complete mold filling even in the microcavities. To ensure a deformation-free demolding the feedstock has to have a high mechanical strength. For demolding the feedstock and the mold insert have to be

cooled down. In consequence the mold inserts are exposed to a variation of temperature during a process cycle which is called the Variotherm process [51, 52]. If mold cavities contain micropatterns which are so small that they cannot be vented in the classical way, i.e. through the parting plane or special bore holes, an evacuation of the cavities prior to injection is necessary [51, 52, 53]. Evacuation of the cavity prevents compression-induced defects in the molding material and in the pinhole-like micropatterns of the mold inserts.

After the patterning by injection molding the binder has to be removed and the parts must be sintered to obtain dense microcomponents. Depending on the binder system, debinding can be carried out by thermal degradation, solvent extraction or catalytic decomposition of the binder components or by a combination of these methods, respectively. Prior to the described debinding steps, a wax or an oily component of the binder can be absorbed by wicking in a powder bed. A preliminary solvent extraction of some binder components creates an open porosity in the green compact, thus reducing the time required for the thermal debinding step and allowing higher heating rates and shorter residence times. For microcomponents with a wall thickness significantly below 1 mm, debinding times are still in the range of 8 to 24 hours. For microparts one cycle in the debinding facility will result in a larger number of parts. Preventing an interaction of the ceramic with the sintering tray and the conservation of the shape is more important than shortening the debinding cycle. The temperature profiles during debinding have to be controlled very accurately to avoid distortion and the formation of cracks and bubbles. When an open porosity has been achieved after the initial debinding stage, the polymeric component should still bind the powder particles together while the temperature is increasing slowly. The part should be completely free of organics as soon as the first sinter necks have formed. Binder residues have be avoided to prevent influences on the base ceramics or the microstructure of the final parts. In the case of carbon removal, this process can be assisted and accelerated to a certain extent by flushing air through the debinding furnace.
To avoid an additional handling step combined with cooling and heating the parts one more time, it is advantageous when the subsequent sintering process can be carried out directly after the debinding step using the same tray and furnace.

The sintering conditions, like temperature profile and atmosphere, mainly depend on the type of ceramic processed. Batch furnaces running under inert or oxidizing atmospheres are quite common. More recently semi-continuous running beam furnaces with separated but queued compartments for debinding and sintering were introduced. During the sintering process the parts usually show a linear shrinkage between 15% and 22%, depending on the powder loading in the feedstock, the powder used and the sintered density reached [54]. Exemplary temperature-time profiles for debinding and sintering of CIM parts with a preliminary solvent extraction are shown in fig. 9.

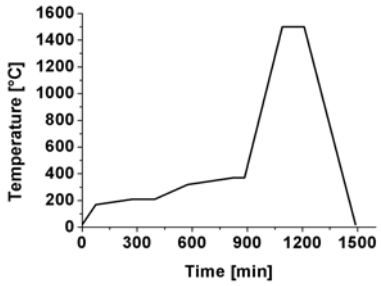

Fig. 9: Representative temperature-time profile for the thermal decomposition of residual binder after partial debinding of the feedstock with a solvent, followed by the sintering procedure (ZrO_2).

Figures 10 to 12 show a variety of injection molded ZrO_2 microcomponents. The ceramic rings (fig. 10) are injection molded in a fully automated process using a fan gate and an automated separation of a micropart from the runner system. The diameter of the hole is 160 µm in the green state. The scale of the ruler in fig. 11 is in centimeters. On the left side in the center a base plate of a planetary gear can be seen, the central planetary gear is located on the ruler in the lower right. A tensile test bar is shown on the upper border, surrounded by nozzle plates of a micro turbine. The smallest channels of these nozzle plates are 25 µm in width. The ceramic ferrule, fig. 12, is an example of a microstructured part with micro precision. Important features here are the diameter of the central hole of 160 µm, and the tolerances of the outer diameter in the micrometer range.

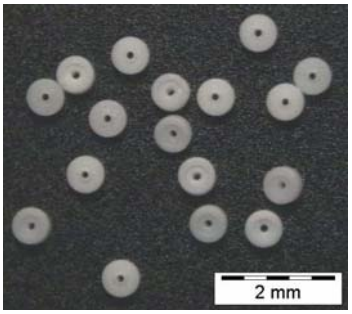

Fig.10: Ceramic microrings, made by HPIM (ZrO_2, green parts)

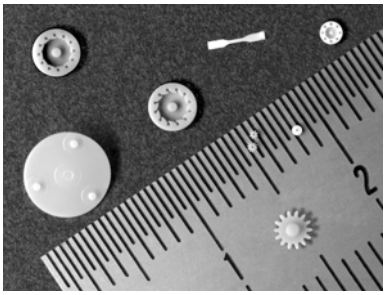

Fig.11: Various sintered ZrO_2 microparts, made by HPIM

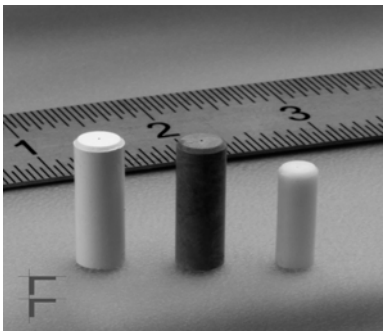

Fig.12: From left to right: HPIM molded green compact, debindered brown compact and sintered example of a ceramic ferrule with an outer diameter of 2 mm for the connection of optical glass fibers. By grinding, a tolerance of about 1 µm in diameter can be achieved [55].

While for series production high pressure injection moulding is the preferable technique, low pressure injection moulding (LPIM) at pressures below 5 bar, where paraffine is used as binder, is a promising technique for small series and for rapid prototyping [56].

Because of the low viscosity of paraffine relatively high amounts of ceramic powders can be added without exceeding the acceptable maximum viscosities. Whereas for polymer-based feedstocks the maximum powder loading is in the range of about 55 vol.%, wax-based feedstocks allow powder loadings of up to 70 vol.%, resulting in a reduced sintering shrinkage.

The low viscosity of the wax-based feedstocks also facilitates the preparation of nanopowder-filled feedstocks with reasonable powder loadings without exceeding the tolerable viscosity limit.

So far mainly metallic tools made by micromilling or by the LIGA process have been used for micro injection molding. For low viscosity binders such as paraffine and for low pressure injection molding even silicone moulds can be used. They are cheap and they can be directly copied from existing specimens, e.g. from polymer parts made by rapid prototyping techniques. The demolding of the green parts from the silicone is possible even with complicated shapes.

4 Component development, prototyping and design

The versatility of the LPIM-process does not only allow the preparation of feedstocks and the fabrication of ceramic microcomponents from a great variety of ceramic materials, see fig. 13, but is also a basis for a complete process chain for prototypes and small scale production [57].

Fig.13: Variety of ceramic microcomponents from different materials made by low-pressure injection molding (LPIM).

Especially in the micrometer range there is still a lack of suited methods for the quick manufacturing of ceramic prototypes. A Rapid Prototyping Process Chain (RPPC), combining the fabrication of a polymer master model by rapid prototyping methods like microstereolithography and the replication of this model into the ceramic part by LPIM using silicone molds, allows closing this gap [56, 58], see fig. 14.

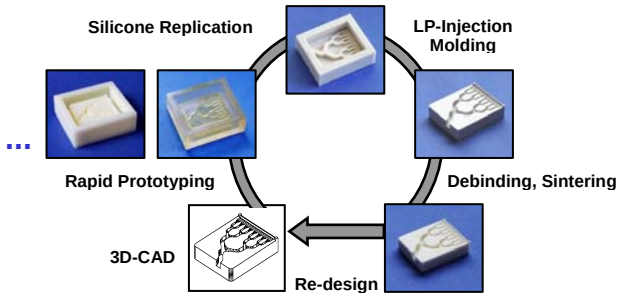

Fig.14: Rapid prototyping process chain for ceramic microcomponents, adapted from [56].

With this process chain it is possible to produce ceramic microparts with full functionality from single prototypes to preliminary or small lot series cost-effectively and in short time. This is possible even for microparts with fine details or with high aspect ratios as it is shown in fig. 15.

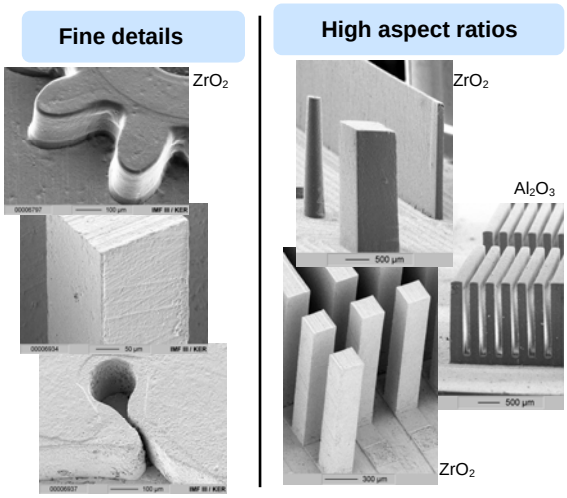

Fig.15: ZrO_2- and Al_2O_3-microcomponents made by the RPPC-process

Furthermore this process chain allows the realization of fast design changes of ceramic microparts. The possibility of fast and uncomplicated design adaptions is still more important, as due to the material characteristics of ceramics some basic design rules should be taken into consideration which differ from those well-known for metallic or polymer materials. So, from the mechanical point of view, tension loads, sharp edges or grooves should be avoided as far as possible. Bending stresses can be tolerated and compressive loads are no problem. Due to the brittle nature of ceramic the thermal shock resistance of actual material must be considered. To avoid distortion during sintering there should be no abrupt changes of the wall thickness or of the mass distribution within the ceramic part. As especially for ceramic microcomponents up to now there are no standardized design rules but only best estimates by the designer, proof testing and design optimization is an important development feature. For this RPPC is an adequate tool. At Forschungszentrum Karlsruhe, the RPPC was developed for the manufacturing of microparts from a great variety of ceramic materials, e.g. for elements of a ZrO_2 microturbine (fig. 16) or for an Al_2O_3-microreactor system (fig. 17), which was developed und manufactured with a RPPC within reasonable time and at acceptable costs [59, 60]. More details on the ceramic micro turbine and on micro gears are given in [61].

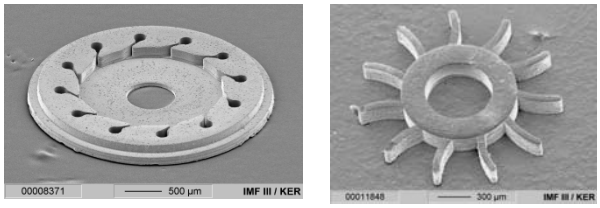

Fig.16: Components of a ZrO_2-micro turbine: nozzle plate (left) and turbine wheel (right) [61].

A whole family of ceramic microreactors has been developed by LPIM and fabricated for operation at high temperatures and/or in harsh environments. The modular design and the easy changeability of the micropatterned internal reactor components predestinates these reactors for testing high temperature reactions or for catalyst screening.

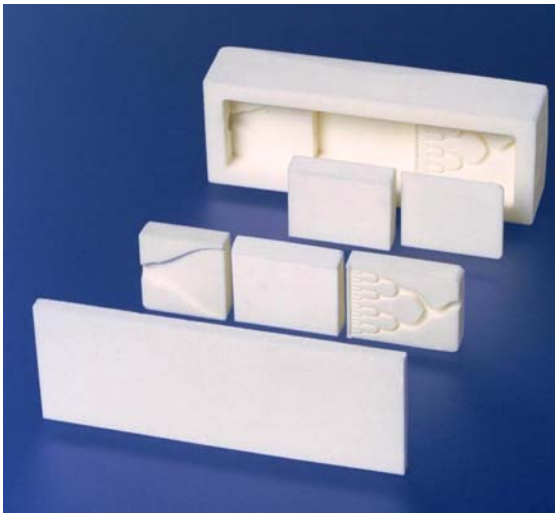

Fig. 17: Modular Al_2O_3 micro reactor system with exchangeable components made by RPPC [59]

Another example for the suitability of RPPC is the development and optimization of microstructured piezoelements from PZT for ultrasonic applications, see fig.18. Here LPIM proved to be superior to the standard dice-and-fill technique, not only because of the fast fabrication of the demonstrators but also because special element geometries can be realized which are impossible to fabricated by dice-and-fill.

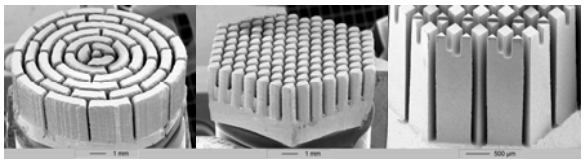

Fig.18: PZT-components for ultrasonic application made by LPIM.

5 Summary and Conclusions

It could be shown that ceramics cover a wide range of application in microtechnology. This holds for structural ceramics – the most widespread materials here are Al_2O_3 and ZrO_2 – as well as for functional ceramics. There are a lot of ceramic materials and processing techniques which can fulfill microtechnical requirements. Of great importance, however, for an efficient development of ceramic microcomponents is an integrated concept reaching from the design idea and the selected material to the final microcomponent especially with respect to the desired functionality, the material characteristics and quality and the suitable processing route. These requirements gain even more significance when keeping in mind the shift from micro- to nanotechnology where still markedly smaller details shall be realized.

6 Acknowledgement

The R+D work presented in this article has been performed in the Institute for Materials Research III by the following scientists (in alphabetical order): W. Bauer, M. Beck, J.R. Binder, H. Geßwein, E. Günther, U. Kaufmann, R. Knitter, L. Merz, M. Müller, G. Örlygsson, F. Paul, V. Piotter, S. Rath, S. Stolz, V.D. Szabo. The support of the work by the technical staff of the institute is gratefully acknowledged.

7. References

[1] T. Hanemann, J. Hausselt, German Patent DE-PS 19 815 978 (15.7.2003), US Patent US-PS 6 573 020

[2] T. Hanemann,M. Börner, J. Göttert,.R. Heldele, G.Motz, M. Schulz, J. Hausselt, Materials Week, München, Germany, September 16-18, 2003

[3] H. Hahn, Adv. Eng. Mat. **5** (2003), 277-284

[4] D. Vollath, D.V. Szabo, S. Fuchs, Nano Structured Materials **12** (1999), 433-438

[5] E. Müller, Ch. Oestreich, U. Popp, G. Michel, G. Staupendahl, K.-H. Henneberg, KONA- powder and particle, **13** (1995) 79-90

[6] E. Müller, Fortschrittsberichte der DKG, Verfahrenstechnik, **17** [1] (2002) (ISSN 0173-9913) 18 – 27

[7] J. R. Binder, F. Paul, S. Werner, Materials Week 2004, München

[8] F. Paul, J.R. Binder, W. Menesklou, J. Haußelt, Annual Meeting of the German Ceramic Soc. Karlsruhe, Germany, Oct. 11-13, 2004

[9] E. Günther, Forschungszentrum Karlsruhe, Nachrichten **30** (1998), 175-182

[10] E. Günther, J. Haußelt, H.-J. Ritzhaupt-Kleissl, German Patent No. DE-OS 1975080, 1999

[11] A. Weddigen, V.D. Hennige, E. Günther, H.-J. Ritzhaupt-Kleissl, J. Mat. Sci. **34** (1999), 3461-3465.

[12] S. Ray, E. Günther, H.-J. Ritzhaupt-Kleissl, J. Mat. Sci. **35** (2000) 6221-6224

[13] J.R. Binder, H.-J. Ritzhaupt-Kleissl, H. Rentsch, K. Dermann, Materials Week 2000, München, Germany, Sept. 25-28, 2000

[14] J. Alkemper, K. Dermann, H. Rentsch, H.-J. Ritzhaupt-Kleissl, J. Haußelt, P. Albert, C. Gall, German Patent No. DE 19846556 A1

[15] J. Alkemper, J.R. Binder, H. Rentsch, H.-J. Ritzhaupt-Kleissl, J. Haußelt, German Patent No. DE 10042050 A1

[16] V. Winter, R. Knitter, Micro Materials 97', Berlin, Germany, April 16-18, 1997

[17] U. Kaufmann, S. Stolz, Annual Meeting of the German Ceram. Soc. 2004, Karlsruhe, Germany, Oct. 11-13, 2004

[18] S. Stolz, W. Bauer, H.-J. Ritzhaupt-Kleissl, J. Haußelt, J. Eur. Ceram. Soc. **24** (2004), 1087-1090.

[19] N. Claussen, T. Le, S. Wu, J. Eur. Ceram. Soc, **5** (1989), 29-35.

[20] D. Holz, S. Pagel, C. Bowen, S. Wu, N. Claussen: J. Europ. Ceram. Soc, **16** (1996), 255-260.

[21] J. H. She, H. Schneider, T. Inoue, M. Suzuki, S. Sodeoka, K. Ueno: Materials Chemistry and Physics **68** (2001), 105-109.

[22] T. Mori, M. Hoshino, H. Yamamura, H. Kobayashi, T. Mitamura: J. Ceram. Soc. Japan, Int. Ed. **98** (1990), 1023-1028.

[23] Ullmanns Enzyklopädie der Technischen Chemie, 4. Auflage, Band 24, S. 696, VCH Weinheim 1984

[24] V. D. Hennige, H.-J. Ritzhaupt-Kleissl, J. Haußelt: Keram. Z. 50 (1998), 262 – 265.

[25] V. D. Hennige, J. Haußelt, H.-J. Ritzhaupt-Kleissl, T. Windmann: J. Eur. Ceram. Soc. **19** (1999) 2901 - 2908

[26] V.D. Hennige, H.-J. Ritzhaupt-Kleissl, J. Haußelt: German Patent DE 195 47 129, 1995, and European Patent EP 0779 259.

[27] J. R. Binder, H.-J. Ritzhaupt-Kleissl, J. Haußelt: dental dialogue 6 (2001) 684 – 686.

[28] H.-J. Ritzhaupt-Kleissl, J. R. Binder, E. Klose, J. Haußelt: cfi/Ber. DKG **79** (2002) E9 –E12

[29] H. Geßwein, J.R. Binder, H.-J. Ritzhaupt-Kleissl, J. Haußelt: J. Eur. Ceram. Soc., in press

[30] J.A. Lewis, J. Am. Ceram. Soc. **118** (2000), 2341-2359

[31] F.F. Lange, J. Am. Ceram. Soc. **72** (1989), 3-15

[32] C.R. Martin and I.A. Aksay, J. Electroceramics **12** (2004), 53-68.

[33] H.-J. Ritzhaupt-Kleissl, H. von Both, M. Dauscher, R. Knitter in H. Baltes, O. Brand, G.K. Fedder, C. Hierold, J. Korvink, O. Tabata (eds.) Advanced Micro- and Nanosystems Vol. 3, "Microengineering of Metals and Ceramics" Wiley VCH 2005, ISBN 3-527-31208-0.

[34] O.O. Omatete, M.A. Janney, R.A. Strehlow, Ceram. Bull (ACerS) **70** (1991), 1641-1649

[35] M.A. Janney, US Patent No. 4894 194, 1990

[36] Y. Xia, G.M. Whitesides, Angew. Chem. Int. Ed. **37** (1998), 550-575.

[37] L.J. Gauckler, T. Graule, F. Baader, Mater. Chem. Phys., **61** (1999)**,** 78-102

[38] R. Knitter, C. Odemer, E. Günther and U. Maciejewski, DE-PS 43 10 068, **1994**.

[39] R. Knitter, E. Günther, U. Maciejewski and C. Odemer, cfi/Ber. DKG **1994**, 71, 549-556.

[40] S. Stolz, FZKA-report, FZKA-6906, Forschungszentrum Karlsruhe, D (2004).

[41] S. Stolz, W. Bauer, H.-J. Ritzhaupt-Kleissl, J. Hausselt, J. Eur. Ceram. Soc. **24** (2004) 1087-1090

[42] J. Tabellion, R. Clasen, Am. Ceram. Soc., (2000), 185-196.

[43] R. Claasen, cfi/Ber. DKG **81** (2004), D12

[44] H.-J. Ritzhaupt-Kleissl, J. Laubersheimer, German Patent No. DE 44 25 978 C1, (1994).

[45] T. Hanemann, M. Ade, M. Börner, G. Motz, M. Schulz, Adv. Eng. Mat., **4** (2002), 869

[46] J. Haußelt, HARMST 2001, 17.-19.06.2001, Baden-Baden, FRG, pp.125-127

[47] R. M. German, Powder Injection Molding, Metal Powder Industries Federation, Princeton, New Jersey, 1990

[48] J. H. Song, J. R. G. Evans, Ceram. Int. **21** (1995), 325-333

[49] J. H. Song, J. R. G. Evans, J. Rheol. **40** (1996), 131-152

[50] B. O. Rhee, M. Y. Cao, H. R. Zhang, E. Streicher, C. I. Chung, in Advances in Powder Metallurgy, Vol. 2: Powder Injection Moulding, Princeton, NJ, 1991, 43-58

[51] F. Nöker, L. Keydel, Kunststoffe **82** (1992) 798-801.

[52] R. Ruprecht, V. Piotter, T. Benzler, J. Hausselt, FZKA-report 6080, Forschungszentrum Karlsruhe, D, (1998) 83-88.

[53] P. Hagmann, W. Ehrfeld, Int. Polymer Processing IV **3** (1989), 188-195.

[54] G. Örlygsson, V. Piotter, G. Finnah, R. Ruprecht, J. Haußelt, Euro PM2003 Conference Proceedings, European Powder Metallurgy Association, Shrewsbury, UK, 2003, 149-154.

[55] M. Beck, V. Piotter, R. Ruprecht, J. Hausselt, Junior EuroMat 2004, Lausanne, CH, September 6-9, (2004).

[56] W. Bauer, R. Knitter, J. Mater. Sci., **37** (2002), 3127-3140

[57] W. Bauer, J. Haußelt, L. Merz, M. Müller, S. Rath, in H. Baltes, O. Brand, G.K. Fedder, C. Hierold, J. Korvink, O. Tabata (eds.) Advanced Micro- and Nanosystems Vol. 3, "Microengineering of Metals and Ceramics" Wiley VCH 2005, ISBN 3-527-31208-0.

[58] R. Knitter, W. Bauer, D. Göhring, J. Mech. Eng. Sci. **217 C1** (2003) 41-51

[59] R. Knitter, M. Liauw, Lab on a Chip **4** (2004) 378-383

[60] R. Knitter, D. Göhring P. Risthaus, J. Haußelt, Microsystems Technologies 7 (2001) 85-90

[61] M. Müller, W. Bauer, H.-J. Ritzhaupt-Kleissl, CICMT 2005, Baltimore US, April 10-13, 2005

Application of metal nanopowders in ceramic technologies

T. A. Khabas

Tomsk Polytechnic University, Tomsk, Russia

Abstract

The specifics of using ultrafine electroexplosive metal powders in powder metallurgy and ceramic technology are considered. The possibility of activating the processes of sintering and synthesis of certain complex oxides and silicates is demonstrated. The effect of metallic additives on hardness, strength, and other properties of materials are established. Reinforced powdered and solid composites are produced in the combustion of oxide-metal mixtures.

The obvious advantages and prospects of highly disperse materials for ceramic productions are discussed in many publications [1]. The biggest part of them currently concentrates on studying nanodisperse (cluster less than 10 nm) powders produced by different methods and products based on these powders [2, 3]. There are significantly fewer studies focusing on the possibilities of coarser and technologically more effective powders [4] obtained by electric explosion of conductors (EEC) [5]. These materials are more frequently classified as superfine or ultradisperse powders and their particle sizes range from 0.03 to 0.10 μm. The studies carried out at the Silicate Technology Department of Tomsk Polytechnic University and at the Research Institute of High Voltage demonstrated the potential of using these powders for a whole spectrum of functional materials: disperse-strengthened metals, antifriction and superhard materials, intermetallic, heat- and electroconducting materials, dielectrics, etc.

The present study considers some specifics of behavior of electroexplosive superfine powders (SFP) in the heat treatment of metallic and oxide-metal mixtures and possibilities of producing intermetallic, metal-ceramic, and ceramic-metal composites.

The EEC method is used to obtain superfine powders of aluminum, iron, copper, nickel, titanium, tungsten, silver, and some other metals, as well as their oxides, carbides, and nitrides. The substantial energy-saturation of such powders [6, 7] and at the same time their sufficient resistance to oxidation in normal conditions under high dispersion (specific surface area of 5 – 20 m^2/g) should be noted. Figure 1 shows the heating curves of ultradisperse copper powder in nitrogen medium that clearly illustrate the emission of excessive energy. The exothermic effect correlating to this process (570°C) is not accompanied by a change in the powder weight and is equal to 16.7 kJ/mole. The accumulated energy of some metals after pulse spraying of conductors and stabilization of SFP is equal to 10 – 60 kJ/mole [6]. These properties contribute to a rapid expansion of application areas of electroexplosive powders. They are promising for ceramic technology [8] and for powder metallurgy.

Electroexplosive metallic SFP in heating (400 – 600°C) react chemically and by diffusion virtually with all known materials, including inert and low-activity ones, such as Pt or Al_2O_3. The unique reaction capacity of SFP, which is related to the dimensional factor as well as to the state of the structure, is used in various processes, including solid-phase processes. Studies demonstrate that metallic SFP under thermal treatment can easily form intermetallic compounds and solid solutions at lower temperatures and at a higher rate. Energy saturated powders of pure metals sinter in a way resembling self-propagating high-temperature synthesis (SHS).

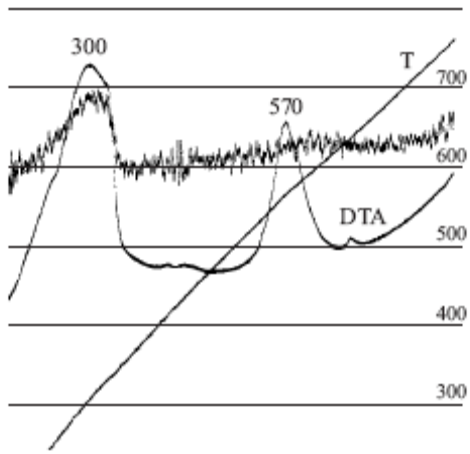

Fig. 1. Thermogram of ultradisperse electroexplosive copper powder in nitrogen medium.

Figure 2 shows a sample made of pure electroexplosive aluminum that was sintered in vacuum on a belt heater heated from beneath up to 250°C. The sintering lasted 1.5 sec. The sintering front has passed via the sample in the form of a luminescent spiral-shaped wave; therefore the sample exhibits spiral stratification.

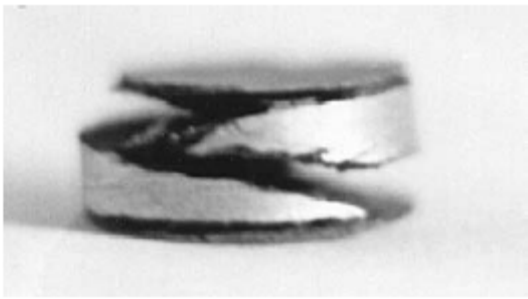

Fig. 2. Sample made of aluminum SFP sintered with self-heating.

In the course of sintering composites containing ultradisperse copper and aluminum, iron and aluminum, iron and nickel, and even such seemingly incompatible metals as high-melting tungsten and aluminum using electroexplosive SFP, disperse-strengthened intermetallics and oxides were identified. Thus, as a consequence of x-ray photoelectron spectroscopy, compounds of the type of WAl4 and WAl2 were registered after sintering in the W – Al system. Abnormally high microhardness values of the sintered composites (Fig. 3) were registered with the atomic ratio W : Al equal to 5 : 1, 1 : 1, 1 : 2, and 1: 20.

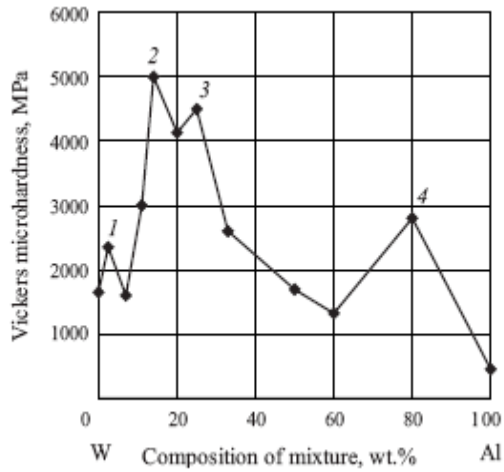

Fig. 3. Microhardness of sintered tungsten-aluminum powder composites: Atomic ratio W/Al = 5:1 (*1*), 1:1 (*2*), 1:2 (*3*), and 1:20 (*4*).

The reaction capacity of superfine metallic powders can be used in the production and strengthening of metal – metal, metal – glass, and ceramic – metal soldered composites to replace low-melting transitional glasses [9]. Thus, a composite containing finely dispersed powders of tungsten (d_{av} = 0.3 – 0.4 μm), copper (d_{av} = 0.1 μm), and aluminum (d_{av} = 0.12 μm) together with coarse industrially produced tungsten and molybdenum powders (d_{av} = 5 – 40 μm) was tested for attaching quartz to tungsten to make current inputs for gas-discharge bulbs. The component that ensures improved adhesion in this case is not only the SFP of relatively low-melting copper but finely dispersed tungsten as well, which already at 1000°C actively adheres to the bulk metal.

Electroexplosive ultradisperse powders can be successfully used to solve such problems of powder metallurgy as increasing hardness and strength of sintered articles made of stainless steel, as well as recycling grinding and cutting waste of expensive alloys. For instance, the hardness of alloy based on steel ShKh15 is only 30 – 36 *HRC* and its bending strength 170 – 190 MPa. The use of a small amount of ultradisperse electroexplosive iron powder (d_{av} = 0.2 μm) allows to raise the hardness of this alloy. Furthermore, this method permits the addition of hard minerals such as corundum or quartz without impairing the mechanical strength of the sintered sample. The effect of STP – Fe additives on the properties of dispersion-strengthened powder alloys is shown in table 1. The average diameter of sintered steel powder particle was 25 μm, the one of introduced oxides 6 – 10 μm.

TABLE 1

Sample	Mixture composition, wt.%*		Sintering temperature, °C	Hardness, *HRC*	Bending strength, MPa
	ShKh15	Fe_{SFP}			
1	67.0	0	1250	34	180
2	66.8	0.2	1250	37	190
3	66.6	0.4	1200	46	230
4	66.5	0.5	1200	48	255
5	66.4	0.6	1200	50	240

* In all cases SiO_2 content was 8.0% and Al_2O_3 content 25.0%.

As the material sinters, a small quantity of mullite $Al_6Si_2O_{13}$ is formed, which additionally increases its hardness. However, the introduction of oxides in this case does not increase the brittleness of the material due to the sintering effect of ultradisperse iron. This is manifested in the increasing strength of contact between the steel particles and in the formation of transitional reaction zones in the form of the fayalite phase on the surface of the quartz grains. The emerging dispersion-strengthened alloy is a finely crystalline structure with a homogenous distribution of oxide and metallic components. Furthermore, the introduction of ultradisperse metal allows the decrease of the sintering temperature.

In utilization of grinding waste, ceramic (containing abrasive waste of Al_2O_3 and SiC), ceramic-metal (WC – Co), and purely metallic materials with satisfactory properties were synthesized using SFP of iron, copper,

and nickel. The introduction of electroexplosive nickel powder (d_{av} = 0.15 μm) is especially effective for sintering cutting tool powders, including those obtained by separation of slime waste. The use of this powder allows for additional dispersion strengthening of sintered materials using oxide powders such as silicon and aluminum oxides and aluminomagnesium spinel without a loss in mechanical strength (Table 2).

TABLE 2

Sample	Mixture composition, wt.%			Microhardness, MPa
	cutting material waste	nickel SFP	$MgAl_2O_4$	
1	100	0	0	1887
2	98	2	0	2318
3	93	2	5	2867
4	88	2	10	4983
5	83	2	15	4872
6	78	2	20	3022

A small quantity of metallic SFP (in this example from 0.4 to 2.0%) is sufficient to achive the strengthening effect. Although electroexplosive powders are inferior to nanopowders obtained by other methods (plasma-chemical, etc.) in dispersion, they are no less active and, which is very important, more convenient to use. They are less aggregated and their agglomerate sizes are smaller by an order of magnitude than those of plasma-chemical powders. They have virtually no hollow particles. When produced in the special explosion chamber, electroexplosive SFP particles are coated in a gaseous cover and have a double electron layer, which in passivation becomes chemically stabilized and has high pseudocapacity [6]. In contrast to colloid particles, electroexplosive particles are hard to polarize and have a total charge approaching zero. All these characteristics facilitate the homogeneous distribution of superfine powder particles over the matrix of coarse industrial powders with formation of their own layer not more than 0.7 μm. When heated to 250 – 400°C (depending on the chemical type), metallic SFP rapidly enter in reactions with oxides or with the ambient medium and have virtually no melted yield of their own.

Based on the performed studies, it is possible to trace several directions in ceramics technology, in which the use of electroexplosive powder appears promising:

- activation of ceramic mixture sintering;
- activation of solid-phase synthesis processes;
- modification of the structure of ceramic materials, including production and stabilization of certain polymorphic forms;
- SHS process;
- synthesis of ceramic mixture components in combustion;
- production of ceramic – metal and metal – ceramic composites in a reducing medium and by hot molding.

The activating effect of additives such as Cu, Ni, Al, and Al_2O_3 – Al composites obtained also by the EEC method is manifested primarily in the sintering of high-melting oxides: Al_2O_3 and ZrO_2. The materials sharply differ in their physicochemical parameters depending on the sintering conditions, the main of which is the firing medium. Sintering of Al_2O_3 and ZrO_2 with SFP metal additives in an oxidizing atmosphere results in the nearly total transformation of metals into oxides. Furthermore, with a corresponding selection of mixture components and a high density of molded samples, metallic SFP enter into chemical reactions with the matrix oxides.

It was experimentally demonstrated in solid-phase synthesis of complex compounds that aluminum SFP forms a highly active ultradisperse oxide and, consequently, acts as the activator of synthesis of complex compounds (Figs. 4 and 5). Multiple experiments in different furnaces showed that the essential condition is a sufficient content of oxygen in the furnace atmosphere. A decrease in the partial pressure of oxygen to $0.103 \cdot 10^5$ Pa virtually completely stops the process. Consequently, the metal (Al) in synthesis first has to pass via the oxidation stage and only afterwards or, possibly simultaneously, the metal occupies in the form of an ion a position in the respective sublattice of the new compound, in our case, cordierite or aluminomagnesium spinel. The latter assumption of the highest activity of metal additives at the moment of their oxidation correlates with the fact that in the case of introducing an equivalent amount of ultradisperse aluminum oxide, which is more disperse than the metal, the yield of the products of synthesis is lower.

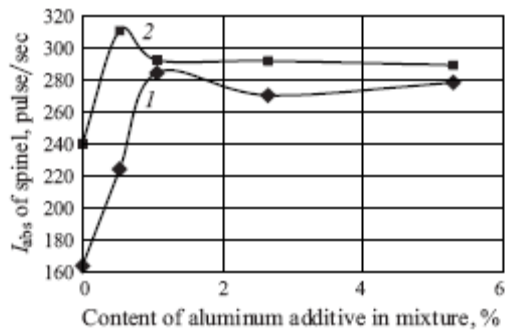

Fig. 4. The effect of ultradisperse aluminum additive on the synthesis of aluminomagnesium spinel at 1200°C (*1*) and 1250°C (*2*): I_{abs} - absolute intensity of x-ray maximum of spinel (d = 0.285 nm).

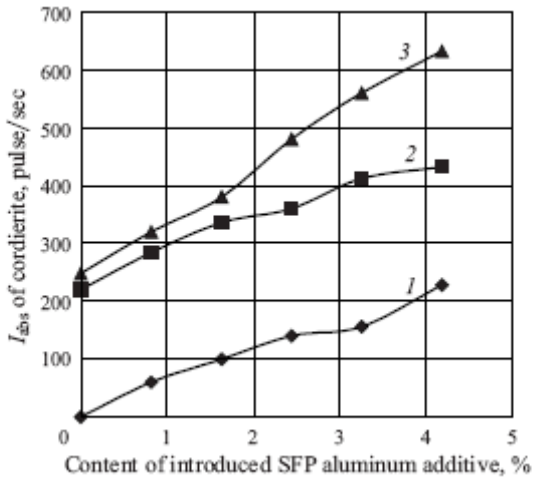

Fig. 5. The effect of SFP aluminum additive on the synthesis of cordierite in a mixture of natural silicates at 1150 (*1*), 1200 (*2*), and 1250°C (*3*): *I*abs) absolute intensity of x-ray reflection of cordierite (*d* = 0.854 nm).

The efficiency of synthesis and sintering of ceramic materials using SFP metals as activators depends also on the dispersion of the matrix material. When ultradisperse metallic powder is introduced into the sintering system, the optimum amount of the additive slightly decreases with increasing size of the main oxide particle. If the sizes of the sintering oxide and the activator additive particles are comparable (for instance, powdered obtained by plasma-chemical synthesis and by the EEP method in sintering of aluminum oxide), the optimum weight content of the activator metal lies within the limits of 0.50 – 1.75% (Fig. 6, curves *1* – *4*). When the activated process consists in sintering of a more coarsely disperse oxide (milled in a ball mill or a vibration mill), the optimum quantity of the additive does not exceed 0.25% (Fig. 6, curves *5* and *6*).

This regularity is caused by the necessity of developing a thin transitional layer in the space between the grains of the sintering oxide, taking into account the geometric ratio of particles of heterogeneous materials. As the content of the metallic additive grows above the optimum value, the emerging transitional layer becomes excessively loose due to its own phase rearrangement, which has no time to be completed in the short sintering interval. The condensation effect in this case would be completely lost.

Rapid heating in vacuum or hot molding in a reducing medium, in contrast to the above described process, facilitates the preservation of the additive in its metallic form, and therefore the high activity of metallic SFP can also be used in the production of metal ceramics. In these processes it is advisable to use relatively inert metals (Cu, Ni, Ag), whose sintering role is based on the formation of liquid-phase interlayers with good adhesion to the sintering oxides (Al_2O_3, ZrO_2, etc.). Such chemically active additives as aluminum or titanium SFP are less effective in these firing conditions, since in the absence of a sufficient amount of oxygen, the reactions and the phase-stabilizing processes of newly formed oxides and compounds do not have time to take place during the short firing interval. The bending strength of such materials does not exceed 200 MPa. By contrast, aluminum and zirconium oxides with a metallic copper additive are sufficiently strong (380 and 320 MPa, respectively, at a firing temperature of 1550°C).

Metal ceramics with ultradisperse copper additives can be used as an antifriction material. Copper powder that is industrially produced has weak adhesion to aluminum oxide. Moreover, aluminum oxide and copper have significantly different sintering temperatures, and therefore it is difficult to obtain a ceramic-metal material with prevalence of aluminum oxide and a slight additive of copper based on industrial powder by using traditional sintering. The use of superfine energy-saturated copper powder permits, due to the high diffusion activity of the latter, to obtain cermets with a uniform distribution of metal on the surface and inside the volume of aluminum oxide grains (USSR Inventor's Certif. No. 1733427). Copper in friction forms a dense plating layer which decreases the friction coefficient and improves the wear resistance of the loaded friction pairs. The specific wear of ceramics with 2% copper SFP and a friction coefficient of 0.08 – 0.09 does not exceed 2.1 x10^{-6} g/h. The material was obtained by hot molding in graphite molds at a temperature of 1500°C.

Recently a new aspect of using superfine electroexplosive metallic powders as materials capable of reinforcing ceramics has been discovered. It concerns the process of synthesis in combustion of aluminum mixed with minerals [10]. The high-temperature oxidation and the binding of air nitrogen from the gas-vapor phase lead to the formation of mono- and polycrystals of aluminum oxide, oxynitride, and nitride. The crystals have an elongated needle or filament shape and virtually pierce the silicate matrix (Fig. 7). In this way the effect of self-reinforcement of material is achieved.

The process can be implemented as combustion of freely poured batch with subsequent molding and sintering or as SHS producing a finished or an intermediate product.

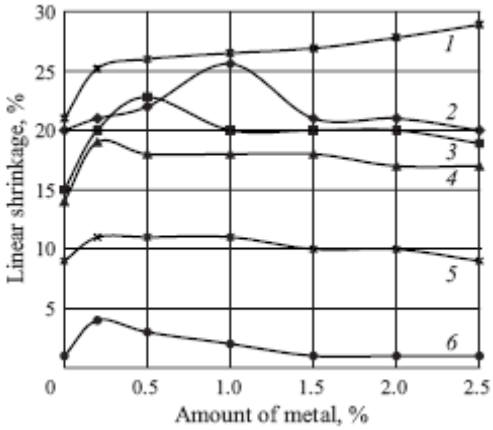

Fig. 6. Sinterability of composites with SFP metal additives: *1*) $Al_2O_3 – ZrO_2$ with Ni additive; *2*) $ZrO_2 – Al_2O_3 – Y_2O_3$ with Al additive; *3*) $ZrO_2 – Y_2O_3$ with Al additive; *4*) ZrO_2 – CaO with Al additive; *5*) ZrO_2 with Al additive; *6*) Al_2O_3 with Ni additive; *1 – 4*) composites based on plasma-chemical oxide powders; *5* and *6*) vibration-milled oxides.

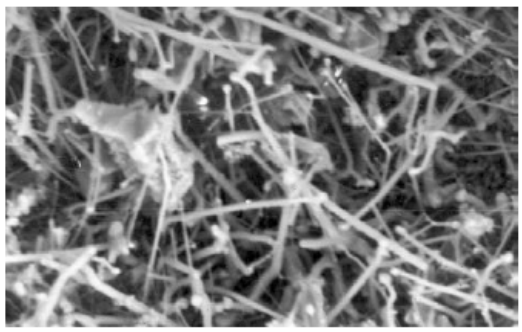

Fig. 7. Reinforcement of silicate matrix by aluminum oxide and nitride crystals.

Powder with reinforced particles can be used as a reinforcing additive in usual batch materials, for instance in clay-talc mixture for producing cordierite. The use of such additives significantly lowers sintering shrinkage (up to zero shrinkage), enables to obtain materials of diverse porosity, and increases the bending strength 1.5 – 2 times.

Thus, despite their rather high cost, the use of small quantities of electroexplosive powders as activators in synthesis and sintering is promising for decreasing energy and metal consumption in the production of ceramic and composite materials. Furthermore, it is obvious that their use opens new possibilities for designing materials with diverse properties for different areas of application.

References

[1] R. A. Andrievskii, "Production and properties of nanocrystalline high-melting compounds," *Usp. Khim.*, **63**(5), 431 – 448 (1994).

[2] I. D. Morokhov, L. I. Trusov, and V. I. Lapovok, *Physical Phenomena in Ultradisperse Media* [in Russian], Énergoatomizdat (1984).

[3] A. I. Gusev and A. A. Rempel', *Nanocrystalline Materials* [in Russian], Fizmatlit, Moscow (2001).

[4] B. S. Bal'dzhinimaev, "Structural and catalytic properties of energy-saturated ultradisperse materials," *Ross. Khim. Zh.*, **45**(3), 59 – 65 (2001).

[5] E. I. Azarkevich, A. P. Il'in, D. V. Tikhonov, and G. V. Yablunovskii, "Electroexplosive synthesis of ultradisperse powders, alloys, and intermetallic compounds," *Fiz. Khim. Obrab. Mater.*, No. 4, 85 – 88 (1997).

[6] A. P. Il'in, "On excessive energy of ultradisperse powders obtained by the wire-explosion method," *Fiz. Khim. Obrab. Mater.*, No. 3, 94 – 97 (1994).

[7] M. M. Mench, K. K. Kuo, C. L. Yeh, and Y. C. Lu, "Comparison of thermal behavior of regular and ultrafine aluminum powders (alex) made from plasma exlosion process," *Combust Sci.Techn.*, **135**, 292 (1998).

[8] T. A. Khabas, "Energy-saturated ultradisperse metal powders in technology of ceramic materials," *Steklo Keram.*, No. 11, 27 – 30 (1997).

[9] T. A. Khabas, A. P. Il'in, and L. A. Lukovskaya, "A study of characteristics of metal-oxide composites for soldering in the W – SiO2 system," *Adgez. Raspl. Paika Mater.*, No. 22, 92 – 95 (1989).

[10] T. A. Khabas, A. P. Il'in, V. I. Vereshchagin, and E. M. Popenko, "Synthesis of ceramic powders in combustion of aluminum with silicate materials," in: *Proc. All-Russia Conf. "Combustion and Explosion Processes in Physical Chemistry and Technology of Inorganic Materials,"* Moscow (2002), pp. 497 – 500.

Passivation and stabilization of aluminum nanoparticles, produced by the electrical explosion of wires (EEW) technology

A.A. Gromov[1], Yu.I. Strokova[1], H.-J. Ritzhaupt-Kleissl[2]

[1]Tomsk Polytechnic University, Chemical Technology Department,
Lenin prospekt, 30, Tomsk, 634050, Russia, gromov@tpu.ru
[2]Forschungszentrum Karlsruhe GmbH, Institut für Materialforschung III,
Hermann-von-Helmholtz-Platz 1,
Eggenstein-Leopoldshafen, 76344, Germany

Abstract

Chemical and physical mechanisms of the formation of passivation coatings on aluminum nanoparticles were studied in this work. Passivation process of coatings on nanoparticles formation were analyzed by SEM, TEM, XRD, EDS, DTA-TG and chemical analysis. Inorganic passivation coatings for aluminum nanopowders are more effective because of their thermal stability than organic ones. The stability of organic passivation coatings to further oxidation does not depend on the type of coating, but depends on the particle size of the passivated powders.

Introduction

Electrical explosion technology for the production of aluminum nanopowders.

Nowadays aluminum nanopowders (a_s=30-300 nm) are produced in a large scale by the European and USA industry [1, 2]. Plasma-chemical synthesis of metal nanopowders based on the evaporation of micron sized powders or bulky metals in the plasma jet [3], and electric explosion of wires (EEW) have become the most widespread technologies for aluminum nanopowders production during the last 20 years [1, 4-11].

The technology of the aluminum nanopowder production by the EEW method was developed at Tomsk Polytechnic University in the seventies of the 20th century and later industrially applied in Russian enterprises and in the few foreign ones [9]. At the present time the price of the aluminum nanopowders, produced with EEW technology is comparable to the price of micron-sized metal powders in the world market [1, 9]. The doubtless advantage of EEW metal nanopowders is their high reactivity at high temperatures (by burning) and stability of their properties during storage [9]. The EEW as a metallic wire destruction method is characterised by the following parameters:

- time of explosion 10^{-5} - 10^{-7} s;
- temperature at the explosion >10^5 K;
- pressure in the explosion wave 10^9 Pa;
- energy, entered into the conductor is comparable with the wire sublimation energy;
- particle formation by gas-like phase condensation and via liquid metal stage.

Aluminum nanopowders (ANPs) obtained with the experimental set-up UDP-4G were investigated in this work. The scheme of the experimental set-up is presented on fig. 1 [12]. The productivity of the set-up UDP-4G is ~100 g/hour for aluminium nanopowders [11].

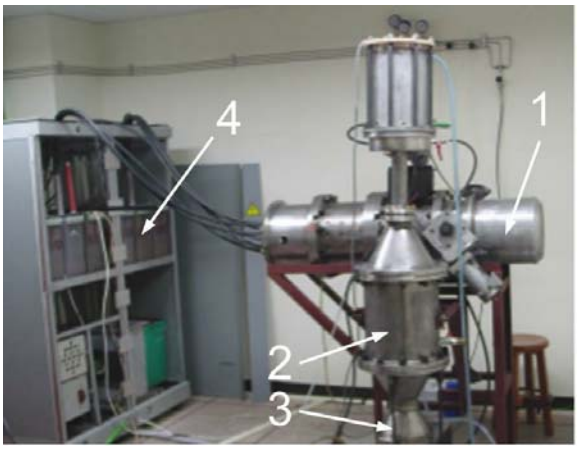

Fig. 1*. UDP-4G facility for the EEW nanopowders production:*
1 – explosion chamber; 2 – powder deposition system; 3 – powder collector; 4 – high voltage unit

Stabilization of Aluminum nanopowders.

The mechanism of ANPs' passivation and stabilization in different gas and liquid media is widely discussed [13-18]. The thickness, the composition and the structure of the passivating layer on particles are the main difference between ANP's and micron-sized powders regarding their oxidation in heterogenic media because they define the diffusion rate of an oxidizing gas at low temperatures and, therefore also define the ignition temperature and the delay period when the ignition of the particles start.

Until now the chemical and physical mechanisms of the formation of passivating coatings on metal nanoparticles are little investigated. In spite of the great number of publications on this subject, the most results, as a rule, are unrepresentative unfortunately. The only few research results are given in [14-17] and these results are not related to the technological scale as a rule.

Aluminum powders (micron-sized and ANPs), obtained in inert gas media (argon, nitrogen or their mixes), are normally pyrophoric, that is why the particles' surfaces are passivated for their stabilization. The passivation for ANPs defines their chemical stability and activity in a following oxidation processes. The traditional method of the passivation of micron-sized powders is coating with hydrocarbons. For example, industrial aluminium powder PAP-2 produced by Russian standard GOST No.5494-95 contains 2-3 wt% of paraffin.

The particles of ANPs are passivated, as a rule, with oxide layers having an amorphous or crystal structure [19-20]. The oxide layers are forming on the ANPs particles by slow oxidation by air during the passivation process. The layers may have a different thicknesses and chemical compositions, dependent on the powders production and passivation methods. For electro-explosive ANPs (fig. 2a, the microscope JEOL 6500 F), the ratio of the oxide layer thickness (2-8 nm) to the particle diameter during air passivation is minimal. This could be shown by transmission electron microscopy (fig. 2b, the microscope PHILIPS CM 200 FEG). Spherical aluminum nanoparticles have amorphous oxide layers which crystallize at a defined thickness (7-8 nm) during a storage period of 2-3 years at room temperature in air. The metal content in the powder substantially is reduced (up to 30-50 wt %) when the ANP particle size decreases. This is shown for a particle size of about ~30 nm in fig. 3. Thus, the combination of optimal properties of the metal nanopowders during the oxidation and burning processes is achieved for particles with a_s=100-200 nm (high enough metal content and thin enough oxide layers). Any oxide component is energetic ballast when a burning of the powders is aimed at. Nevertheless, the aluminum oxide content for most of ANPs is more than 10 wt%, while micron-sized aluminum powders contain only 0.5-2.5 wt% of oxide. As a rule, the smaller particle diameter results in the lower metal content, and the metal content is only 30 wt% for the particle size of 10 nm. The aluminum content is 80-90 wt% in ANPs stabilized with organic reagents [21-22]. This is due to insufficient passivating by particles' coating. Thus, the investigations of improving the quality of ANPs by passivation processes should be concentrated on two directions: searching for effective passivating reagents and simultaneously increasing the metal content in ANPs. An interesting method for the solution of this problem is the passivation of the powders not with oxide layers, but with active reagents which do not reduce the powder burning enthalpy.

Non-oxide passivating coatings should be applied on the particles either during the ANPs' synthesis process or after the particles' cooling but before their contact with air [23], because the particles are immediately oxidized at their first contact with air. Organic and non-organic compound layers can be applied on the ANP particles as non-oxide coatings. As a rule, the ANPs coated with aluminum oxide are used as reference samples.

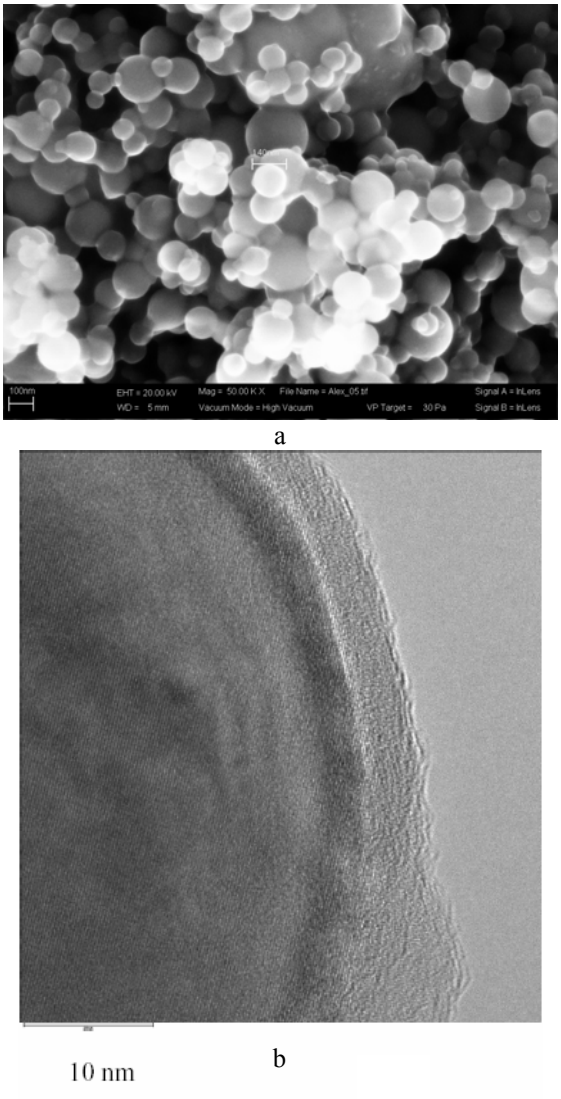

***Fig. 2**. SEM image of EEW aluminum nanopowder (a, ×50000) and aluminum nanoparticle, coated by oxide layer (b, ×1000000)*

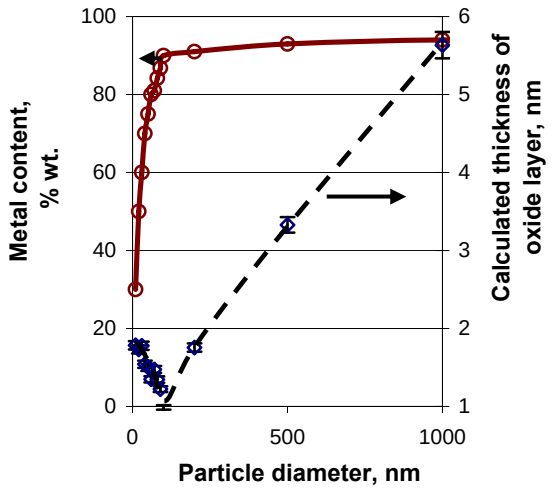

***Fig. 3**. Experimentally determined metal content in aluminum nanopowder and calculated thickness of oxide layers on particles*

Theoretical and experimental background

Chemical and pphysical processes in aluminum nanoparticles during their passivation by slow oxidizing under air atmosphere.

Directly after the wire explosion, Al nanoparticles coagulate and precipitate in the collector [11] or are exposed to the cyclone-type unit for powders fractions of different size separation [1]. Self-sintering of nanoparticles was not observed as it is observed for aluminum nanoparticles synthesized under equilibrium conditions [24]. When the electric explosion is performed under overpressure the nanoparticles have adsorbed argon gas on their surface which does not allow the particles to build contacts and prevent them from sintering in the first minutes after synthesis [18]. Aluminum nanoparticles were exposed to the oxidation of their surface by slow reaction with air for 72 hours during the passivation process. The ANPs placed into a hermetic box filled with argon (air concentration ~0.1 vol%) were periodically mixed at room temperature. The air concentration was kept constant in the passivation box. The temperature control of the passivation process was realized with Alumel/Chromel thermocouples placed into the powder.

Immediately after their formation the particles start to adsorb Argon. As Argon desorption is an endothermic process, the temperature decreases. In the following argon was gradually replaced by atmospheric components. At first these components adsorb on the particles surface, and then they chemically interact leading to the protective oxide-hydroxide layer formation. This is accompanied by a temperature increase.

The result of the mass-spectrometric analysis of the gases isolated from ANPs after prior incomplete passivation by air is presented in the table 1. Gaseous N_2, CO_2 and water are the main constituents evolved from the mentioned fractions during heating. Hydrogen evolving started at 200°C and then became more intensive from 600°C on. The gas with the ratio m/z=17 appeared in the thermal desorption spectra at 770°C; the gas peak intensity exceeded the water one. If the intensity ratios of the water peak (m/z =18) and OH ion peak (m/z =17) must be equal to 3/1, than the exceeding species, obviously, can be correlated with the NH_3 appearance in the mixture of the thermo-escaped gases. The ammonia appearance was possible due to AlN hydrolysis which takes place by ANP reaction with air nitrogen during the passivation. The catalytic reaction of nitrogen and hydrogen on the aluminum or aluminum oxide surface could be another way of ammonia formation. The hydrogen presence in the composition of thermo-desorbed gases was probably caused by hydrogen accumulation at the aluminum oxidizing by water fume during the passivation process (protonic mechanism of oxidation). The sharp increase of the hydrogen emission rate was observed at temperatures higher than 200°C. It could be attributed to hydride decomposition or to hydrogen desorption.

Thus, oxide and hydroxide layers were generated on the surface of the aluminum nanoparticles during the passivation process. These layers can adsorb atmospheric gases in large quantities.

The EDS data of the ANP samples after passivation showed the presence of the aluminum compounds with oxygen deficiency in the surface and near-surface layers of the particles. The atomic concentration ratio Al/O changed from 0.42/1 up to 0.61/1 for partially passivated ANPs (table 2). The oxygen content on the particles' surface increased during the last stage of the passivation. The singlet signal was observed in the spectrum of ANPs according to electronic paramagnetic resonance data [19]. This signal intensity was dependent on the oxygen partial pressure over the particles' surface. In accordance with the infrared spectroscopy data, the absorption bands with maximum in the range 950-1440 sm^{-1} could be related to chemisorbed oxygen molecule. Semi-empirical calculations with the data from infrared spectroscopy and electronic paramagnetic resonance were performed. They lead to the assumption that the oxygen molecule join with the particle surface by the one linkage (Al-O-O$^{\bullet}$) and a paramagnetic radical remains with the corresponding singlet signal.

The processes in the oxide-hydroxide layer were studied for ANP samples subjected to incomplete passivation (№ 6, table 2). This nanopowder specific surface measurement during the passivation process showed that the specific surface was relatively fast increasing during the initial passivation stage – maximum on 30-40 % for 2 h. After that the specific surface was slowly decreasing on 20-30% for a few days. Probably, the increase of the specific surface resulted from the formation of the oxide-hydroxide layer with the friable structure on the metal surface. Later, the layer condensed and crystallized and the specific surface decreased.

The growth of the protective oxide-hydroxide layers on the metal nanoparticles was satisfactorily corresponding to the model of the formation of very thin layers [25]. The nanoparticles had amorphous oxide layers according to XRD data (fig. 4) and transmission electron microscopy data (fig. 2, b).

Table 1 – Mass-spectrometric analysis of gases evolved from ANPs, obtained in H_2

T, °C	T gas evolving, °C			
	m*/z**=28 (CO^+, N_2^+)	m/z=44 (CO_2^+)	m/z=18 (H_2O^+)	m/z=17 (OH^+, NH_3^+)
240-460	460	400	240	400

*m – ion weight in atomic units,
**z – ion charge.

Table 2 – XPS data for passivated ANPs

№	Powder	Binding energy, eV		Storage time, min	Atomic ratio Al/O (related formula)
		O 1s	Al 2p		
1	ANP	531.7	74.3	800	0.44/1 ($Al_2O_{4.5}$)
2		531.8	74.3	700	0.61/1 ($Al_2O_{3.3}$)
3		531.6	74.2	400	0.71/1 ($Al_2O_{2.8}$)
4		531.9	72.7	300	0.95/1 ($Al_2O_{2.1}$)
5		531.1	73.0	200	0.94/1 ($Al_2O_{2.1}$)
6		530.9	72.2	48	0.86/1 ($Al_2O_{2.3}$)
7	ASD-4 (etalon)	531.6	74.3	15000	0.53/1 ($Al_2O_{3.7}$)

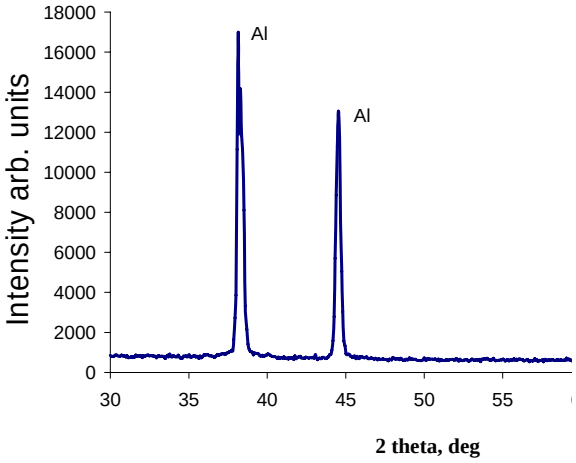

Fig. 4. *XRD pattern for passivated ANP*

The only metallic aluminum reflexes were on the XRD pattern. The oxide layer thickness was calculated based on the specific surface values of the oxides and the masses of metal and oxide (table 3) by equation (1).

The calculated thickness of the oxide layer (φ) shows minimum values for particles with ~100 nm in diameter. These particles had optimal combination of the most important physical properties i.e. high stability and high metal content. The smaller aluminum particles had a lower metal content and, consequently, a thicker oxide layer. For the large particles the oxide layer thickness increased up to 80 nm for particles with the diameter 1 mm. For ANP (a_s = 140-290 nm) obtained in Ar+H_2 mixture, the calculated oxide layer thickness was 0.8-1.7 nm at the oxide content 1.1-3.7 wt% For ANP (a_s = 120-160 nm) obtained in gaseous Ar. The calculated oxide layer thickness was 1.5-2.1 nm and the aluminum oxide content 8.4-8.8 wt% For ANP (a_s = 210-290 nm) obtained in the Ar+N_2 mixture (table 4), the calculated oxide layer thickness was 1.63-2.20 nm and the aluminum oxide content – 6.0-9.1 wt%. Thus, the EEW aluminum nanoparticles showed oxide layers, which are about 500 % thinner, compared to particles of industrial spherical aluminum powders (table 4). This fact was confirmed by electron microscopy data (fig. 2, b). The real thickness of the oxide layer on the ANP particles was twice as thick as calculated. This was caused by the friability and partial loss of the passivating layers.

$$\varphi = R - r = \sqrt[3]{\left(\frac{m_{Al} + m_{Al2O3}}{(\rho_{Al} \cdot x_{Al} + \rho_{Al2O3} \cdot x_{Al2O3})(4/3 \cdot \pi)}\right)} - \sqrt[3]{\frac{m_{Al}}{4/3 \cdot \pi \cdot \rho_{Al}}}, \quad (1)$$

where φ - oxide layer thickness, R – particle radius (outer), r – metal nucleus radius (inner), m_{Al} and m_{Al2O3} – metal and oxide weights in the particle, ρ_{Al} and ρ_{Al2O3} – metal and oxide density in the particle, x_{Al} and x_{Al2O3} – metal and oxide weight parts in the particle.

Table 3 – ANP characteristics (exploded in Ar + N_2)

№	Voltage, kV	Entered energy, e/e_c	C_{Al}, %	S_{sp} (BET), m^2/g	a_s, nm	Oxide content, % wt.	Oxide layer thickness (φ), nm
1	30	1.82	88.0±1.4	10.8±0.3	210	9.0	1.84
2	28	1.71	87.9±0.3	9.9±0.3	220	9.1	1.96
3	26	1.62	88.1±1.1	9.9±0.9	220	8.9	1.91
4	24	1.45	88.5±0.9	9.3±0.3	240	8.4	1.95
5	22	1.30	90.9±0.8	8.8±0.25	250	6.1	1.43
6	20	1.13	90.0±0.6	6.7±0.2	330	7.0	2.20
7	18	0.92	91.0±0.7	7.7±0.25	290	6.0	1.63

Table 4 – Calculated oxide layer thickness for aluminum particles

Particle diameter, nm	Powder	S_{sp} (BET), m^2/g	Oxide content, % wt.	Calculated particle density, kg/m^3	Oxide layer thickness (φ), nm
10	ANP	222.2	70	3603	1.78
20		111.1	50	3345	1.73
30		74.1	40	3216	1.78
40		55.6	30	3087	1.54
50		44.4	25	3023	1.5
60		37.0	20	2958	1.35
70		31.8	19	2945	1.47
80		27.8	16	2904	1.34
90		24.7	13	2870	1.22
100		22.2	10	2829	0.99
200		11.1	9	2816	1.76
500	ANP(“tails”)	4.4	7	2790	3.33
1000	ASD -8 (fine fraction)	2.2	6	2777	5.63
10000	ASD -4	0.2	2	2726	17.90
100000	ASD -1	0.02	1	2713	88.10
1000000	ASD -1 (“tails”)	0.002	0.1	2701	87.10

Chemical mechanism of aluminum nanopowders' passivation by slow oxidation in air.

If one takes the oxide layer (thickness 20-40 nm) covering the particle of micron-sized powder (a_s = 10 μm) and calculates the residual metal content for spherical nanoparticles with equal thickness of oxide layer, the metal content would be more than 40-60 wt% The real metal content for ANP is 95 wt%. This indicates the mechanism of the inhibition of the oxidation process in ANP. In the thin layer case [25], the oxidation process is limited by the electric charge of double electric layer (DEL) [26-27]. Thus, the oxidizer diffusion to the metal surface is controlled by DEL charge. Being different from inert substances, metals in the colloid condition form oxide-hydroxide layers on their surface [26]. The DEL structure will have some features dependent on the chemical processes proceeding on the metal particles [28-29]. Metals are reducing agents and they are charged positively in red-ox processes. The electric current running during the electro-chemical reaction – metal oxidation by oxygen or water (Faraday current) – gives the extra potential [29], larger “capacity” which is named “pseudo-capacity” in contrast to ordinary DEL capacity. Thus, the total polarization capacity of the interfacial boundary “metal-gas” could be calculated using the equation (2).

$$C_{total} = C_{DEL} + C_{pdc}, \quad (2)$$

where C_{DEL} – DEL capacity; C_{pdc} – pseudo-capacity, caused by chemical reaction proceeding.

In contrast to bulk aluminum (electrically neutral), aluminum nanoparticles produced by the EEW method were separated by charge in the electric filter. During the EEW, the particle charge could be formed as a result of thermo-emission and ionization by electric field, and the charge structure stabilization was a result of a high cooling rate of the products and of the presence of an electro-magnetic field [29]. In comparison with neutral particles, charged ones hold the polarized Ar molecules stronger due to the stronger “dipole – induced dipole” interaction (fig. 5). The uncharged particles will interact with argon due to the weaker dispersion attraction mechanism. The electron transfer (penetration through oxide) from metal to oxidizer or the oxidizer drift (H^+ protons) to interface “metal-oxide” occurs during the passivation by slow oxidation in air. The charge of the positively charged particle increases and reaches the electro-

static potential, which is necessary for the inhibition of the oxidation process faster than the uncharged particles. In the case of negatively charged particles, the oxidation process intensively proceeds till this charge's complete compensation.

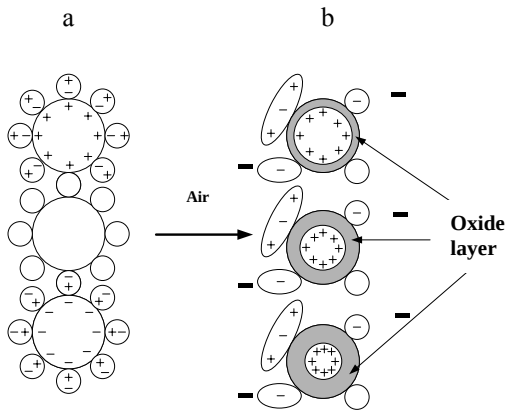

Fig. 5. *Chemical diagram of aluminum nanoparticle passivation: a – particle structure (not in a real scale) before passivation; b – particle structure after passivation*

The main reason for the deposition of ANP on electric filter electrodes is the particles' static charge arising directly in the time of conductor explosion. Both the ANP fractions from positively and negatively charged electrodes and the fraction non-settled on the electrodes were studied by bomb calorimetry (table 5). The data show the ANP fractions non-settled on the electric filter electrodes. They have the highest specific surface value and the lowest calorific value during the combustion in the bomb. The least oxide formation enthalpy (less than standard one) was typical for aluminum in this kind of fraction. The calorimetric data of aluminum fractions obtained by charge separation in the electric filter confirmed the suggested scheme of the electric explosive particles structure (fig. 5). The energy content was higher for negatively charged particles (table 5). The positively charged nanoparticles had higher stability against oxidation in comparison with the particles having not enough charge. It can be assumed that the possibility of the formation of complicated (flaky) charging structures, depend only on the conductor material and is initiated by the dispersion mechanism of the conductors during the EEW process (wire disintegration to cluster and gas-alike phases) [29]. Based on the EEW mechanism the gas-like phase had a negative charge in the primary stage of dispersion, and being the lightest one, it disappears from the conductor axle faster and is broken faster too. In a next step the positively charged liquid-like phase overtakes and permeates the gas products' layers. Regarding the fact that the EEW products show a markedly temperature decrease during the period of their relatively separate existence, there is an increased possibility of the stabilization of charging structures.

The stability of EEW nanoparticles during the storage is mostly determined by their synthesis conditions. Optimal electrical explosion regime and passivation conditions are necessary to get powders with a high metal content. The increase of the extra metal content in nanopowders is possible because of their passivation with the layer-formative liquids. The choice of the optimal passivation method of metal nanopowders is determined by their application field [30, 31]. When the ANP shall be used in high-temperature processes it is necessary to keep the layer-protected particles away from interaction with environment.

At present time the majority of EEW ANPs (a_s = 30-300 nm) on the world market are passivated with oxide layers formed during the slow ANP oxidation by air [32]. In fact, this method of passivation can be considered as a process of "passivation till self-saturation" including the reactions (3-4).

$$2\,Al(s) + 3/2\,O_2(g) \rightarrow Al_2O_3(s) \quad (3)$$

$$2\,Al(s) + 3\,H_2O(g) \rightarrow Al_2O_3(s) + 3\,H_2(solved) \quad (4)$$

Then the additional metal quantity is subjected to oxidation to achieve a positive potential, necessary for stabilization. So, the nature of a potential barrier providing the stability of aluminum nanoparticles is connected with the electric static field of the surface and above-surface particles layers having different charges.

It is obvious that the water vapor contained in air is a more reactive passivating agent than oxygen. Therefore aluminum nanoparticles passivated by air contain up to 2 wt% of hydrogen (hydrogen analyser RHEN 602). The main idea of the use of the non-oxide passivating layers applied on the electroexplosive ANP particles is the possibility to increase the metal content in them.

Results and discussion

In the present work the EEW ANPs[♣] after obtaining and before contact with air were passivated by the following substances: 1) liquids – nitrocellulose (NC), oleic acid (Ol Ac, $C_{17}H_{33}COOH$) and stearic acid (St Ac, $C_{17}H_{35}COOH$) dissolved in the kerosene and ethanol; fluorine-polymer; 2) solids – amorphous boron, nickel; 3) gases – N_2, CO_2 and air (for comparison). The ANP passivation method was chosen reasoning from prior experiment results – if the nanoparticles after formation come in contact with air, the formed oxide layers (~10 wt% Al_2O_3 for particles with the diameter ~ 100 nm) could not be removed by any subsequent treatment.

The characteristics of studied ANP samples are presented in the table 6. The specific surface of the powders was determined by BET method, metallic aluminum content by volumetric analysis [33].

[♣] ANP samples were obtained in the High Voltage Research Institute of Tomsk Polytechnic University and the Institute of High-Current Electronic Institute (Siberian Branch, Russian Academy of Science).

The powder ALEX (sample № 1, table 6) with known characteristics [34] was chosen as a comparison sample. The samples № 2 and 3 were obtained from the composite wires Al-Ni and Al-B, correspondingly [23]. During the EEW process H_2 was added to Ar for the sample № 4 obtaining, N_2 for the sample № 5 and (N_2+CO_2) mixture for the sample № 6. The ANP passivation by gases was carried out for 72 hours at T = 30±2ºC and p = 0.11 MPa (samples № 2-6). The samples № 7-11 were passivated before the contact with air by the following organic substances:

- 7 - 0.1 wt% stearic acid in ethanol;
- 8 - 0.1 wt% stearic acid in kerosene;
- 9 - 0.1 wt% oleic acid in ethanol;
- 10 - 0.1 wt% fluorine-polymer solution;
- 11- 0.1 wt% nitrocellulose solution in ethanol.

Ethanol and kerosene were chosen as solvents because they didn't react with ANPs. The passivating reagents' solutions were added to the just obtained powders and were mixed for ~2 hours. The passivation temperature was kept at 30±5°C to prevent the powder from self-heating. The solvent residue was removed from ANP by vacuum drying at room temperature. All powders after passivation were kept at open air for two months to reproduce industrial production conditions. The samples after the first stage of analysis (table 6) were kept in air at room temperature and at a relative humidity ~70 % for two months. The particles' composition and morphology (table 7) were studied by XPS (PHILIPS CM 200 FEG) and XRD (Rigaku "MAX-B", CuK_α-radiation). The methods of the differential scanning calorimetry and thermogravimetry (thermal analyzer Universal 2.4 F TA Instruments) were used to test the ANP regarding their non-isothermal oxidation (table 8).

Table 5 – Enthalpy for ANP combustion

Sample (gas media)	S_{sp} (BET), m^2/g	ΔH^{298} (Al_2O_3), kJ/mole
1. ANP (H_2) average:	7.4	1728.4±6.0
- from the positively charged electrode;	5.4	1804.1±6.0
- from the negatively charged electrode;	6.1	1737.5±6.0
- neutral fraction.	9.0	1595.2±5.5
2. ASD-4 (etalon)	0.8	1667.7±5.0

Table 6 – ANP characteristics

№	Sample	Wire composition	Gas media	Passivation condition	S_{sp} (BET), m^2/g	C_{Al}, % wt.	C_{Al}, % wt. (1 year age)
1.	ALEX	Al	Ar	Air	11.3	86	85
2.	Al (Ni)	Al (Ni)	Ar	Air	40.7	53	53
3.	Al (B)	Al (B)	Ar	Air	12.0	84	82
4.	Al (Ar+H_2)	Al	Ar + 10 % vol. H_2	Air	9.4	92	92
5.	Al (N_2/CO_2)*	Al	N_2	CO_2	19.5	84	n/a
6.	Al (N_2+CO_2/N_2)*	Al	N_2+CO_2	N_2	30.1	67	n/a
7.	Al (St Ac) etanol	Al	Ar	Stearic acid in etanol	12.1	74	70
8.	Al (St Ac) kerosene	Al	Ar	Stearic acid in kerosene	7.3	79	59
9.	Al (Ol Ac) etanol	Al	Ar	Oleic acid in etanol	14.3	45	43
10.	Al (F)	Al	Ar	Fluoropolymer	11.6	81	81
11.	Al (NC)	Al	Ar	Nitrocellulose in etanol	12.6	68	58

* Ref. [35].

Powder ppassivation by Al_2O_3 is the most suitable way to realize ANP with non-oxide protective layers. Thermal properties of such powders are ellknown [36, 37]. That is why all EEW ANP properties were compared with the industrial aluminium powder ALEX (tables 6-8). All experimental ANP samples excepting № 4 and 8 had larger specific surface values than ALEX powder. "Non-oxide" passivation has a stronger influence on the metal content in ANP. Metallic aluminum remained in quantity of 45-81 wt% in the samples passivated by organic substances. The reduction of metallic aluminum content was maximal (up to 45 wt %) for ANP passivated by oleic acid. Ttherefore, the passivation by liquid organic reagents resulted in a considerable decrease of metal content in the powder (table 6). Besides, the material of the passivating layer permanently reacted with ANP, e.g., the metallic aluminium content reduction after 12 months of storage for samples № 7-11 was higher for the samples passivated by the gaseous and solid substances.

The XPS and XRD results of the ANP samples are presented in the table 8. All samples contained more than 10 wt% of oxygen (in the form of

γ-Al_2O_3) on the particles surface. The aluminum carbide traces were in the samples № 7 and 9, although carbon was not found by XPS method as the carbon layers were used as samples substrates only.

Table 7 – Elemental and phase composition

№	Sample	Element content, % wt. (XPS data)*		Phase composition (XRD data)**
		O	Al	
1.	ALEX	10±2	90±5	Al (04-0787)
2.	Al (Ni)	22±3	74±2 %+4 % Ni	Al
3.	Al (B)	11±2	89±4	Al
4.	Al ($Ar+H_2$)	9±2	91±5	Al
5.	Al (N_2/CO_2)	18±3	82±3	Al, γ-Al_2O_3 (47-1308)
6.	Al (N_2+CO_2/N_2)	33±4	67±2	Al, γ-Al_2O_3
7.	Al (St Ac) etanol	15±2	85±3	Al, traces of Al_4C_3 (35-0799)
8.	Al (St Ac) kerosene	15±2	85±3	Al
9.	Al (Ol Ac) etanol	18±3	82±3	Al, traces of Al_4C_3
10.	Al (F)	12±2	88±4	Al
11.	Al (NC)	n/a		Al, γ-Al_2O_3

* Powders surface for analysis ~20 x 20 μm. XRD pattern for sample № 4 and corresponding analyzed surface is on fig. 6.

** No. of JCPDS card (PCPDFWIN v.1.30).

Table 8 – Parameters of reactivity for ANPs with non-isothermal oxidation in air (Table 6)

№	Sample	T_{on}, °C	Weight of coating (adsorbed gases), %	+Δm (до 660°C), %	+Δm (до 1400°C), %	ΔH_{ox}^{Al} up to 660°C, Дж/г	α* (500÷1400°C), %
1.	ALEX	597	2	26	68	5465	89
2.	Al (Ni)	655	9	13	43	n/a	88
3.	Al (B)	601	2	24	63	6232	84
4.	Al ($Ar+H_2$)	606	2	25	75	4730	92
5.	Al (N_2/CO_2)	564	2	27	62	n/a	83
6.	Al (N_2+CO_2/N_2)	551	4	16	32	2784	54
7.	Al (St Ac) etanol	643	5	23	58	5997	88
8.	Al (St Ac) kerosene	631	6	27	74	6282	100
9.	Al (Ol Ac) etanol	653	10	15	38	4875	95
10.	Al (F)	636	6	21	68	5184	94
11.	Al (NC)	645	24	10	24	н/о	40

$$*\alpha\ (Al \rightarrow Al_2O_3) = \frac{+\Delta m}{C_{Al} * 0{,}89} * 100,\ \%$$

Where C_{Al}, % - Al metal content in ANP (Table 6); +Δm – weight increase with metal oxidation.

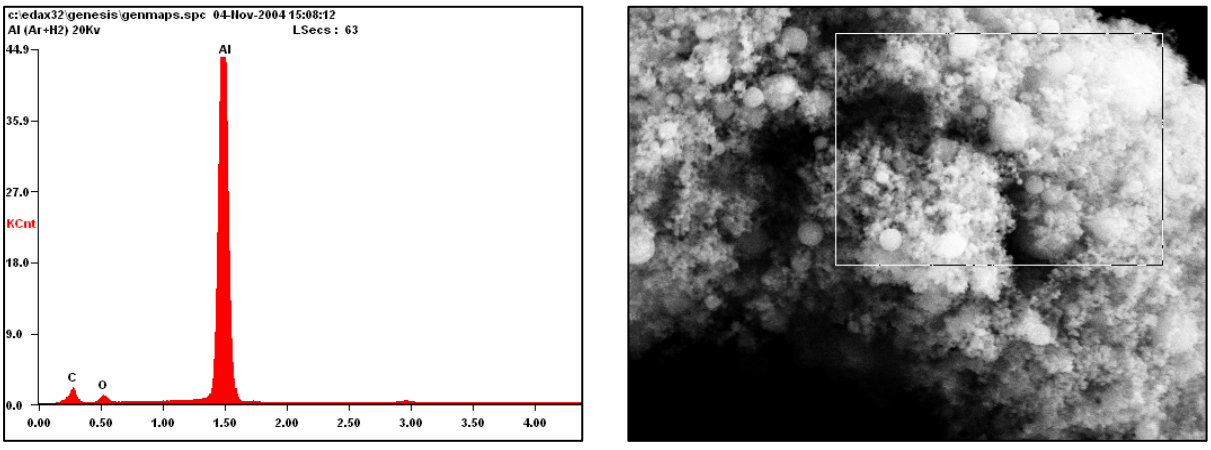

a *b*

Fig. 6. *XPS spectrum (a, sample 4 table 7) and corresponding surface of the analyzed sample (b)*

Boron was not found in the sample № 3 probably because of its low molecule weight and, as a consequence, a low sensitivity of XPS method. Nitrogen was also not displayed in the samples № 5 and 6 by the XPS method. Crystalline phase γ-Al_2O_3 (5-9 wt %) was disclosed in the samples Al (NC), Al (N_2/CO_2) and Al (N_2+CO_2/N_2).

The results of the ANP analysis by the DSC-TG method in air are presented in the table 8. The intensive oxidation of ANP in air started below the aluminum melting temperature (660 °C). The DSC and TG curves were similar for all ANP samples. The were two stages of reaction: at first an intensive oxidation before Al melting accompanied by a sharp mass increasing followed by a second less intensive stage of a total oxidation up to ~1400 °C [38].

The temperature of the intensive oxidation onset was maximum for the sample Al (Ni) (table 8), that can probably be attributed to the refractory nickel presence in the composition of the passivating layer on the particle surfaces (see table 6). The temperature of the oxidation onset varied in the range 597-655 °C for the samples passivated in air, in the range 551-564 °C for the samples passivated by CO_2 and N_2 and was not dependent on other powder characteristics and type of passivating layer. Such behaviour of the ANPs was caused by the fine fraction presence in the powder which strongly influences the powder reactivity in total. The temperature of the oxidation onset was lower on 33-46 °C for powder ALEX than for the samples № 5 and 6. The weight of the adsorbed gases was not more than 4 % for "dry" ANP samples № 1-6 except for the sample Al (Ni). The weight of the organic cover (samples № 7-11) was 3-4 times higher then for the "dry" ANP samples № 1-6. It should be noted the total cover weight was even higher than that, which could be attributed to the cover oxidation process and "aluminium-cover" interaction simultaneously proceeding with desorption during the heating.

The maximum value ΔH_{ox}^{Al} was found for the samples covered with boron and stearic acid in kerosene (6232 and 6282 J/g, correspondingly). Probably, boron and residual kerosene introduced the additional heat contribution to the oxidation process.

The fractional conversion (α) for the ANP samples was relatively high for all samples up to T = 1400 °C (table 8) except for the fully oxidized sample № 6 and for sample № 11 in which Al interacted with nitrocellulose (table 7).

Characteristics of ANPs passivated by gaseous and solid reagents (samples № 1-6, table 6).

The highest metallic aluminum content was in the samples ALEX, Al ($Ar+H_2$) and Al (N_2/CO_2) (table 6). The specific surface of the sample № 4 (Al ($Ar+H_2$)) was two times higher than for Al (N_2/CO_2), i.e. for powder formation with larger particles (tables 6 and 7) the EEW (electrical explosion of wires) in the ($Ar+H_2$) medium resulted in less oxidation after passivation by air. The parameters C_{Al} and S_{sp} had the inverse correlation – the higher S_{sp} the less C_{Al} (especially for the samples № 2 and 6). The ANPs passivated by N_2 and CO_2 contained Al_2O_3 (table 7). Hence, the metastable compounds "Al-N" and "Al-C" formed on the particles surface at the production and storage in N_2 and CO_2 mediums oxidized at the following powder contact with air. Therefore, the starting temperature for intensive oxidation was minimal for the samples № 5 and 6 (table 8). Both very fine and coarse fractions were contained in the sample Al (Ni). According XPS, nickel (4 wt %) didn't accumulate on the ANP particle surface but settled in the form of a fine NiO powder. Thus, the "Al-Ni" wire explosion resulted in the formation of finer particles than aluminum wire without cover and the particle size was less than the ANPs stability boundary (~ 30 nm). The residual non-oxidized aluminium particles completely reacted with air at temperatures T < 1000°C and Ni used in this case did not increase the stability of the fine aluminium fraction against oxidation in air.

All powders contained 2-4 wt% of adsorption gases (table 8). But the sample Al (Ni) contained 9 wt% of gases that was the result of its high specific surface value. Besides, the dissolved hydrogen evolving from ANPs particles could be the reason for a low oxidation starting temperature (~190°C) for the sample Al ($Ar+H_2$) in comparison with the ALEX one. The stabilisation of ANPs by boron [23] leads to a promising fuel component because the particles coated with boron are able to increase the powder burning enthalpy. The C_{Al} and S_{sp} values for the sample (covered with boron) were comparable to the values for the sample № 1 (ALEX, table 6) and to its average value of fractional conversion up to 1400°C (table 8). The powder covered with boron had the highest value of ΔH_{ox} among "dry" samples № 1-6 (table 8).

Characteristics of ANPs passivated in the liquid mediums (samples № 7-11, table 6).

Stearic and oleic acids as passivating reagents reacted chemically with aluminum of ANPs. The deeper chemical interaction was in the case of oleic acid, the aluminum content decreased to 45 wt% after passivation (sample № 8) and kept to decrease at the storage (table 6). The aluminum interaction with stearic and oleic acids resulted in particles surface carbonization (see table 7). Nitrocellulose was permanently oxidizing the ANP particles – the powders contained the metallic aluminum on 10 wt. % less after one year storage than just-obtained ones. Regarding the use in fuels the samples Al (F) and Al (NC) are most promising because of the composition of their components. Nnevertheless, they have a sufficiently low metal content. Adsorbed organic layers on the powder particles did not protect them from the following oxidation for

ANPs passivated in organic liquids; intrinsic oxide layers grow below the organic layer (fig. 7).

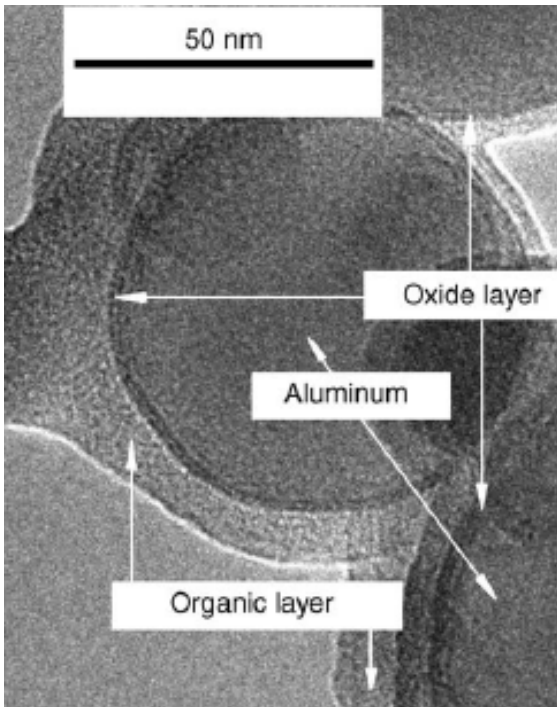

Fig. 7. *TEM image of aluminum nanoparticle, passivated with stearic acid (×500000)*

The oxygen content in the form of Al_2O_3 was higher for the sample № 9 than for the other ones passivated by the liquids (table 7).

Conclusion

This work gives a review on the results of the complex investigations of metal nanoparticles (Al and other active metals), produced by EEW technology and passivated in different media. Gaseous, liquid and solid passivative reagents (11 types) were investigated. Recommendations regarding their applications were given [39, 40]. The advantages of "non-oxide passivation" are the potentially higher combustion heat of fine powders covered by organic passivating layers. The advantages of aluminum nanopowders could be clearly shown in comparison with the commercially produced powder ALEX®. The ΔH_{ox}^{Al} (J/g) and α (%) values obtained from DSC-TG data are very important characterization parameters because they can be correlated to ANPs' combustion enthalpy. The particle size of ANPs was inversely dependent on the metal content in the powder. The samples № 3-5 passivated by boron, air and CO_2 had the best characteristics taking into account the parameters ΔH_{ox}^{Al}, α, S_{sc} and C_{Al} (table 6-8). Thus, the EEW in the ($Ar+N_2$) or ($Ar+H_2$) media or the application of the refractory and high-exothermic reagents on the surface of the nanoparticles resulted in improvement of the characteristics of ANPs. Organic layers, covering the nanoparticles, did not provide a total protection from the following oxidation. Oxide layers were found on the nanoparticles below the organic layers.

Acknowledgement

This work has been performed with the financial support of Russian Foundation for Basic Research (project 08-08-12013) and under the collaboration between Tomsk Polytechnic University and Forschungszentrum Karlsruhe. Authors appreciate kind consultations of Prof. A.P. Il'in.

References

[1] Lerner M.I. Doctoral thesis. Tomsk: Tomsk Polytechnic University, 2007. [in Russian]
[2] Ivanov Yu.F., Osmonoliev M.N., Sedoi V.S. et al. // Propellants, Explosives, Pyrotechnics. 2003. Vol. 28. Is. 6. P. 319-333.
[3] Gusev A.I. Nanocrystalline materials – methods of production and properties. - Ekaterinburg: Russian Academy of Sciences, 1998. [in Russian]
[4] Yavorovkii N.A. Candidate thesis. Tomsk: Tomsk Polytechnic University, 1982. [in Russian]
[5] Rahel A.D. // Journal of Technical Physics. 1995. Vol. 65. No. 12. P. 27-38. [in Russian]
[6] Sedoi V.S., Valevich V.V. // Letters to Journal of Technical Physics. 1999. Vol. 25. No.7. P. 584-585.
[7] Semkin B.V. Electrical Explosion in Condensed Medias // Tomsk: Tomsk Polytechnic University, 1979. [in Russian]
[8] Chase W. Exploding Wires. Wiley, 1963.
[9] Ilyin A.P. // Izvestiya Tomskogo Polytehnicheskogo Universiteta, 2003. Vol. 306. No 1. P. 133-139. [in Russian]
[10] Burtsev V.A., Kalinin N.V., Luchinskii A.V. Wires Electrical Explosion and its Application in Electric Physical Facility. Moscow: Energoatomizdat, 1990. [in Russian]
[11] Tikhonov D.V. Candidate thesis. Tomsk: Tomsk Polytechnic University, 2000. [in Russian]
[12] Kwon Y.S., Gromov A.A., Strokova J.I. // Applied Surface Science. 2007. Vol. 253. No. 12. P. 5558-5564.
[13] Gromov A.A., Ilyin A.P., Tikhonov D.V. // Prospective Materials. 2003. No. 2. P. 95-101. [in Russian]
[14] Liangui Guo, Wulin Song, Mulin Hu, Changsheng Xie, Xia Chen // Applied Surface Science. 2008. Vol. 254. Is. 8. P. 2413-2417.
[15] Liangui Guo, Wulin Song, Changsheng Xie, Xiaota Zhang, Mulin Hu // Materials Letters. 2007. Vol. 61. Is. 14-15. P. 3211-3214.
[16] Sanchez-Lopez J.C., Caballero A., Fernander A. // J. Eur. Ceram. Soc. 1998. Vol. 18. P. 1195-1200.
[17] Sanchez-Lopez J.C., Fernandez A., Conde C.F., Conde A., Morant C., Sanz M.J. // Nanostructured Materials. 1996. Vol. 7. № 8. P. 813-822.
[18] Kwon Y.S., Gromov A.A., Ilyin A.P., Rim G.H. // Applied Surface Science. 2003. Vol. 211. No. 1-4. P. 57-67.
[19] Ilyin A.P., Lyashko A.P., Fedushchak T.A., Barbashin Ya.E. // Physics and Chemistry of

Materials Treatment. 1999. No 2. P. 37-42. [in Russian]
[20] Zelinskii V.Yu., Yavorovskii N.A., Proskurovskaya L.T., Davidovich V.I. // Physics and Chemistry of Materials Treatment. 1984. No 1. P. 57-59. [in Russian]
[21] Bellito V.J., Russell J.N. // Materials of 36th International Annual Conference of ICT and 32nd International Pyrotechnics Seminar "Energetic Materials. Performance and Safety", FRG, Karlsruhe. June 28-July 1, 2005. P. (137-1) - (137-11).
[22] Jigatch A.N., Leipunskii I.O., Kuskov M.L. et al. // Chemical Physics. 2002. Vol. 21. No. 4. P. 72-78.
[23] Ilyin A.P., Krasnyatov Yu.A., Tikhonov D.V. A Method for Powders Obtaining. RF patent 2139776. 1999. [in Russian]
[24] Gleiter H. // Acta mater. 2000. Vol. 48. P. 1-29.
[25] Hauffe K. Oxydation von Metallen und Metallegierungen. Berlin: Springer. 1957.
[26] Frolov Yu.G. Colloidal Chemistry. Surface Phenomenas and Dispersed Sysytems // Textbook for High Schools. M.: Chemistry, 1989. 464 p. [in Russian]
[27] Mulvaney P. in: Nanoscale Materials in Chemistry // Ed. K. Klabunde. John Wiley and Sons. 2001. P. 121-167.
[28] Zelinskii V.Yu., Yavorovskii N.A., Proskurovskaya L.T., Davidovich V.I. // Physics and Chemistry of Materials Treatment. 1984. No. 1. P. 57-59. [in Russian]
[29] Ilyin A.P. // Physics and Chemistry of Materials Treatment. 1994. No. 3. P. 94-97. [in Russian]
[30] Granier J.J., Plantier K.B., Pantoya M.L. // Journal of Materials Science. 2004. Vol. 39. P. 6421-6431.
[31] Kwon Y.S., Gromov A.A., Ilyin A.P. // Combustion and Flame. 2002. Vol. 131. No. 3. P. 349-352.
[32] Kwok Q.S.M., Fouchard R.C., Turcotte A.-M. // Propellants, Explosives, Pyrotechnics. 2002. Vol. 27. P. 229-240.
[33] Fedotova T.D., Glotov O.G., Zarko V.E. // Propellants, Explosives, Pyrotechnics. 2000. Vol. 25. P. 325-332.
[34] Energetic Materials. Ed.: Teipel U. Wiley-VCH. 2004.
[35] Chemezova L.I., Ivanov Yu.F., Osmonaliev M.N. et al. // European Conference for Aerospace Science (EUCASS), July 4 - July 7, 2005, Moscow, Russia, Rep. 5.03.05, P. 1 – 7.
[36] Eisenreich N., Fietzek H., Juez-Lorenzo M.M. et al // Propellants, Explosives, Pyrotechnics. 2004. Vol. 29. № 3. P. 137-145.
[37] Mench M.M., Kuo K.K., Yeh C.L., Lu Y.C. // Combustion Science and Technology. 1998. Vol. 135. P. 269-292.
[38] Physics and Chemistry of Metal Nanopowders Combustion in Nitrogen-contained Medias. Ed.: A.A. Gromov. TSU press. 2007. [in Russian]
[39] Arhipov V.A., Korotkih A.G., Kuznetsov V.T., Savelieva L.A. // Chemical Physics. 2004. Vol. 23. No. 9. P. 18–21. [in Russian]
[40] Gromov A.A., Popenko E.M., Il'in A.P., Vereshtchagin V.I. // Chemical Physics. 2005. Vol. 24. No. 4. P. 66–79. [in Russian]

The Phenomenon of Chemical Binding of Air Nitrogen with the Formation of Nitride Phases in the Process of Burning of Metals, Boron and Silicon Powders

A.P. Ilyin, L.O. Tolbanova, A.V. Mostovschikov
Tomsk Polytechnic University

Abstract

The research stages of nitrogen chemical accumulation during metals, boron and silicon powders burning in air, with the formation of independent crystal phases of nitrides are presented in the paper. The extraordinary characteristic of this phenomenon is connected with a contradiction: thermodynamic calculations show that nitrides are being oxidized by oxygen. It has been shown that the phenomenon is interdisciplinary: its manifestations are applicable in many spheres of science and technique. A probable mechanism is proposed regarding the formation of nitrides under high temperature conditions in the presence of air oxygen.

Introduction

The problem of reactivity of molecular nitrogen remains urgent for a number of reasons [1]. It is the basic component of the earth's atmosphere and participates in biochemical processes. The use of air in high-temperature processes in recent years sharply grows: during the combustion of fuels at the thermal power plants, in the internal combustion engines, with the large technogenic and natural fires, in a number of industrial productions etc.

For a long time the problem of nitrides formation and stabilization through air nitrogen binding has being solved in the direction of catalysts and strong reducer search in order to obtain nitrogen-containing compounds at room temperature [2, 3]. However, any substantial results were not achieved: even in the reducing atmosphere the yield of nitrogen-containing compounds was extremely small.

In a number of works [4, 5] it was noted that in the composition of condensed combustion products of solid rocket propellants nitrogen in trace quantities was found, but the form in which compounds were binding was not clarified.

The absence of interest in the problem of high-temperature binding of air nitrogen was also caused by the traditional point of view, which allows the possibility of the formation of nitrides only as intermediate substances, but supposing their further oxidation to oxides [6]. Actually, elementary calculations and calculations with the help of contemporary software applications show that nitrides must not be stabilized as the end-products. According to the accepted point of view, with obtaining of nitrides even small admixtures of oxygen are inadmissible [7].

The purpose of this work is the experimental and theoretical proof of the before unknown phenomenon of the chemical binding of air nitrogen resulting in the formation of nitride phases in the burning process of metals, boron and silicon powders.

Experimental results

For the first time formation and stabilization of nitrides were found as a result of burning of aluminum nanopowders produced from aluminum wires by electric explosion in argon, hydrogen, and helium media [8-10]. Already the first experiments showed that the end-products of burning contained up to 40 % wt. of aluminum nitride as the basic crystal phase. In 1998 a paper was published [11] which stated that there had also aluminum nitride was found in the burning products of aluminum, but in the roentgenogram reflections of aluminum nitride were absent. By that time we had also obtained nitrides of boron, silicon, titanium, and zirconium [12, 13, 14]. Besides, as a confirmation of the nitride formation, there was published the information on obtaining lanthanum nitride in the process of metallic lanthanum burning in air [15]. The processes of aluminum and other metals burning were thoroughly studied [16-17]. It was established that in the burning process of small dispersive powders, aged and covered by a thick oxide shell, in the end-products there also were stabilized corresponding nitrides [18]. Research activities on how additions of various nanopowders influence the yield of aluminum nitride during aluminum nanopowders burning in air were conducted [19]. There was established the dependence of aluminum nitride yield on burning sample mass [20], on air volume in the closed chamber [21], on air pressure in the chamber [22], on degree of agglomeration, and on passive functional coating nature [23]. Dependent on the burning conditions, maximum yields of nitrides were reached (% wt.): AIN -69; BN – 52; ZrN – 90; TiN – 88.

Apart from the known nitrides of elements of the 3-rd and 4-th groups of the Periodic system,, recently nitrides of chrome and, possibly, molybdenum, and tungsten have been obtained by burning of their

mixtures together with aluminum nanopowders in air [24, 25].

Burning of mixtures of oxides (TiO_2 and ZrO_2) with aluminum nanopowder in air also leads to binding of air nitrogen with the formation of stoichiometric nitrides (TiN and ZrN) [26].

Among the products of burning of aluminum hydride in air a relatively high content of aluminum nitride (~50 % wt.) was also found [27].

Condensed burning products of model rocket propellant on the basis of octagon also contain aluminum nitride [28].

The process of burning of nanopowders and small dispersive powders of aluminum, titanium and others, aluminum hydride, mixtures of aluminum nanopowder with chemical compounds: titanium and zirconium dioxides resulting in nitride formation occurs in two stages. At the first stage (at 800 – 1200 °C) burning out of the absorbed hydrogen takes place. At the second stage the burning process turns into high temperature (2000 – 2400 °C). The nitride synthesis process occurs at the second, high temperature stage. The yield of nitrides depends on the burning temperature: the higher the temperature the higher the yield of nitrides. Such regularity was obtained for aluminum nanopowder with the following additives (9 % wt.): nanopowders of iron, molybdenum, tungsten [23]. They contribute to increase of the burning temperature, increasing the yield of aluminum nitride to 14 % wt. It is important to notice that the time of the first stage changes from some seconds to several minutes, whereas during the second stage, as a rule, the burning process proceeds at high speed (about 5-20 seconds), excluding a cooling time [13]. During the second stage a burning flame of gaseous burning products above a burning powder is observed [29].

The mechanism of chemical air nitrogen binding

It is known that the molecule of nitrogen has a triple chemical bond between the atoms; the energy of its breaking is 940 kJ/mole, which is considerably higher than the energy of bond breaking in the molecule of oxygen, hydrogen and other gases [30]. At the same time the triple bond is strongly polarized and the molecule of nitrogen becomes reaction-capable even at room temperature: one of the products of oxidizing metallic lithium is nitride Li_3N [31]. According to the calculations and experimental data, the dissociation of nitrogen molecules becomes noticeable only at 4000 °C [30]. Therefore the formation of nitrides at burning occurs probably according to a different mechanism, but not through nitrogen dissociation.

The most thoroughly investigations regarding the mechanism of air nitrogen binding had been performed for the aluminum burning process. High burning speed on the second stage and the high temperature allowed supposing that during the first stage the process of oxidizing occurs according to a diffusion mechanism:

$$2Al + 3/2O_2 \rightarrow Al_2O_3,\ \Delta H^0_f = -1667 \text{ kJ/mole},$$

and then it transfers into a gaseous phase process. Thereby the destruction of protective shell of aluminum oxide at more than 800 °C occurs with the formation of gas suboxides:

$$4Al_{(liquid)} + Al_2O_{3(gas)} \leftrightarrows 3Al_2O_{(gas)}.$$

In works [8-10] it was supposed on the basis of thermodynamic calculations that aluminum nitride formation occurs by the interaction of aluminum suboxide (I) with a molecule of nitrogen:

$$2Al_2O + 2N_2 \rightarrow 4AlN + O_2.$$

At that the reaction of aluminum nitride formation even in the direct interaction of aluminum with nitrogen at 2000 – 2400 °C is endothermic, so promoting the stabilization of aluminum nitride.

The necessary condition of the formation of aluminum nitride as an independent crystal phase is that within a certain volume and within a certain time interval the aluminum nitride formation is the only reaction occurring. In turn this requires the storage of initial reagents for this reaction.

In dissertations [25, 32, 33] and monographs [16, 17] thermograms and thermal analysis data are given on which oscillatory processes under conditions of high-temperature burning are observed: increase and subsequent decrease of the temperature of reaction mixture (DTA). The explanation of these processes is given in work [25]. There is demonstrated that the formation of aluminum nitride, as an endothermic process, decreases the temperature. There may be several oscillations of such type (fig.1): the more active nanopowder is, the more oscillations there are. Thereby nanopowder of metallic aluminum may be complete oxidized.

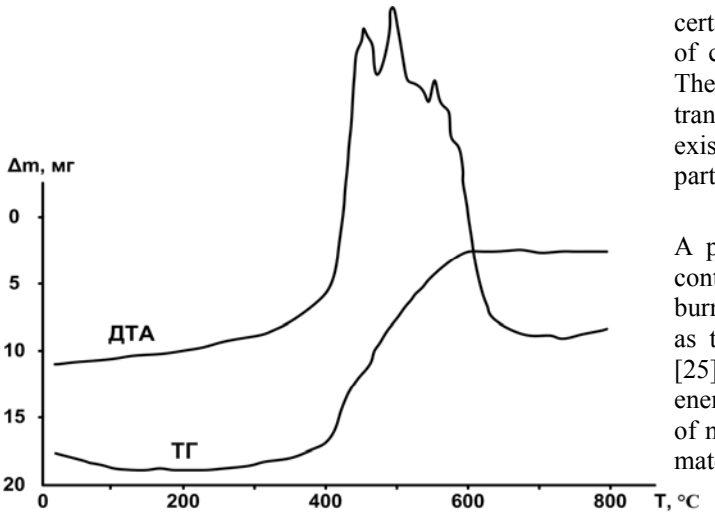

Figure 1. Thermal analysis (TG, DSC) of aluminum nanopowder: m=50mg, speed of heating – 10 K/min, atmosphere – air, crucible – platinum.

During burning of inactive nanopowders and small dispersive powders, oscillatory processes were not observed. Nevertheless, initiation of interaction between Al_2O and nitrogen remained unclear.

In earlier works oscillatory processes during burning of aluminum powders in air were also found [4, 5]. Heterogeneous burning was considered to be accompanied by thermal fluctuations which were not associated with nitride formation. A similar explanation is given for the analysis of oscillatory and pulsating processes at solid rocket propellants and pyrotechnic compositions burning. The processes during burning of other metal powders (titanium, zirconium, chromium) and nonmetals (boron and silicon) [12] also occur via the formation of suboxides.

The interdisciplinary character of the phenomenon

The phenomenon of chemical binding of air nitrogen resulting in the formation of crystalline nitride phases at burning of metals, boron and silicon powders, has not been known before our works, and is connected with the occurrence of high-temperature chemical reactions with the participation of two oxidizers – oxygen and nitrogen. It takes place during the burning processes of metal-containing and boron-containing rocket propellants and pyrotechnic compositions. Transition of burning to gaseous phase increases speed, but formation and stabilization of nitrides decrease the energetic yield of propellants [28]. Thus, it is necessary to take into consideration this influence on characteristics of compositions: during the oxidizing of 1 mole of aluminum to Al_2O_3 837 kJ/mole is emitted, while only 320 kJ/mole is emitted during oxidation of 1 mole of aluminum to AIN.

A number of problems in the geochemistry of mountain rocks can be solved if to concede that at certain stages of the earth crust development nitrides of certain metals and nonmetals were formed [12]. The point is that the chains of chemical transformations have the so called ‘white spots’, the existence of which can be explained by the participation of nitrides.

A perspective direction in the synthesis of nitride-containing ceramic materials is the synthesis by burning of metal, boron and silicon powders, as well as their mixtures with compound substances in air [25]. Thereby, complicated facility, pure nitrogen and energy costs are not required. The unique properties of nitrides can be used in ceramic and compositional materials.

Binding of air nitrogen by burning can be put in the basis of ammonia production: combustion of aluminum powder – hydrolysis of combustion products – drying up of the products of hydrolysis – electrolysis – powder production – combustion [33]. Preliminary calculations have shown that such a cycle is 3-4 times more profitable in comparison with the synthesis of ammonia according to Haber. In this case the expense component in the new scheme is the electric power.

Air nitrogen binding is possible also in conditions of technogenic and natural fires, especially during burning of petroleum, coal, shale oil, and peat. The presence of coal and hydrocarbons, as reductors during burning, contributes to the formation and stabilization of nitrides [19].

Conclusion

Thus, a cycle of researches, being conducted during 20 years, has shown that the high-temperature (>2000 °C) burning of powdered metals (aluminum, titanium, zirconium, chromium) and nonmetals (boron and silicon) in air leads to formation and stabilization of corresponding nitrides as independent crystal phases, thereby their content in final products at certain conditions exceeds 50 % wt. According to thermodynamic calculations nitrides have to be fully oxidized by air oxygen: kinetic braking of the thermodynamically permitted chemical process is observed.

The results obtained show that a before unknown phenomenon of chemical binding of air nitrogen at high-temperature burning of powders of elements of the 3-rd, 4-th and 6-th groups of the Periodic system with formation and stabilization of the corresponding nitride phases has been established.

References

[1] Chatt J. Richards L. The New in Chemical Fixation of Nitrogen. - M.: Mir. - 1983. - 304 p.

[2] Denisov N.T., Kobeleva S.I., Shestakov A.F. // Kinetika I Kataliz. - 37. – No.4. - P.528.

[3] Nikolayev G.V., Denisov N.T., Efimov O.N. and others // Kinetika I Kataliz. - 1993. - Vol.34. - No.1. - P.186.

[4] Maltsev V.M., Maltsev M.M., Kashporov L.Ya. The Fundamental Characteristics of Combustion. - M.: Chimija. - 1977. - 320 p.

[5] Pokhil P.F., Belyayev A.F., Frolov Yu.V. and others. Combustion of Powdered Metals in the Active Media. - M.: Nauka. - 1972. - 298 p.

[6] Boborykin V.M., Gremyachkin V.M., Istratov A.G. // Fizika Gorenija I Vzryva. - 1983. - No.3. - P.22.

[7] Samsonov G.V. Nitrides. - Kiev: Naukova Dumka. - 1969. - 371 p.

[8] Ilin A.P., Proskurovskaya L.T. On the Special Feature of Oxidation of Metals in Ultradispersed State. TPI. Tomsk. Dep. in ONII TEKHIM. - 1988. - No.905. - 22 p.

[9] Ilin A.P., Proskurovskaya L.T. //Fizika Gorenija I Vzryva. - 1990. - Vol.26. - No.2. - P.71.

[10] Ilin A.P., Proskurovskaya L.T. // Poroshkovaja Metallurgija. - 1990. -No.9. - P.32.

[11] Shevchenko V.G., Kononenko V.I., Bulatov M.A. and others // Fizika Gorenija I Vzryva. - 1998. - No.1. - P.45.

[12] Ilin A.P. // Geochimija. - 1993. - No.9. - P.1371.

[13] Ilin A.P., An V.V., Vereshchagin V.I., and others // Fizika Gorenija I Vzryva. - 2000. - Vol.36. - No.2. - P. 56.

[14] Ilin A.P., Karataeva E.A., Khabas T.A., Vereshchagin V.I. The Method of Graphite-Like Boron Nitride Obtaining. A. s. of the USSR No.1805627. Prior. 16.01.90.

[15] Shevchenko V.G., Kononenko V.I., Lukin I.V. and others // Fizika Gorenija I Vzryva. - 1999. - No.1. - P.85.

[16] Ilin A.P., Gromov A.A. The Oxidation of Aluminum and Boron Ultrafine Powders. - Tomsk: TPU. - 1999. - 131 p.

[17] Ilin A.P., Gromov A.A. Combustion of Aluminum and Boron in Ultrafine State. - Tomsk: Publ. Tomsk State University. - 2002. - 154 p.

[18] Ilin A.P., An V.V., Vereshchagin V.I. and others // Steklo I Keramika. - 1998. - No.3. - P.24.

[19] Ilin A.P., Yablunovskiy G.V., Gromov A.A. // Fizika Gorenija I Vzryva. - 1996. - Vol.32. - No.2. - P.108.

[20] Ilin A.P., Gromov A.A., Popenko E.M. and others // Fizika Gorenija I Vzryva. - 2001. - Vol.37. - No.6. - P.56.

[21] Ilin A.P., Popenko E.M., Gromov A.A. and others // Fizika Gorenija I Vzryva. - 2002. - Vol.38. - No.6. - P.1.

[22] Ilyin A.P., Kwon Y.S., Gromov A.A. and others // Combustion and Flame. - 2003. - Vol.133. - No.4. - P.349.

[23] Ilin A.P., Gromov A.A., Foze-Bath U., and others // Fizika Gorenija I Vzryva. - 2006. - Vol.42. - No.2. - P. 1.

[24] Ilin A. P., Tolbanova L.O. // Fizika Gorenija I Vzryva. - 2007. - Vol.43. - No.4.

[25] Tolbanova L.O. The Synthesis of Ceramic Nitride containing Materials by Combustion of Mixtures of Aluminum Nanopowder with W and Mo Nanopowders and Cr Powder in Air. Dissertation for Obtaining of Candidate of Technical Sciences Degree. - Tomsk: TPU. - 2007. - 215 p.

[26] Ilin A.P., Astankova A.P., Amelkovich Yu.A., Tolbanova L.O. The Method of Metal Nitride Obtaining. Claim for Patent of RF No. 2007112044. Prior. 02.04.2007.

[27] Ilin A.P., Bychin N.V., Gromov A.A. // Fizika Gorenija I Vzryva. - 2001. - Vol.37. - No.4. - P.139.

[28] Ilyin A.P., Kwon Y.S., Gromov A.A. and others // Combustion Science and Technology. - 2004. - Vol.176. - No.2. - P.277.

[29] Ilin A.P., Gromov A.A., Tikhonov D.V. and others // Fizika Gorenija I Vzryva. - 2002. - Vol.38. - No.1. - P.139.

[30] Gurvich L.V., Karachavtsev L.V., Kondratyev L.V. and others. Tensile Energy of Chemical Bonds. Ionization Potentials and Electron Affinity. - M.: Nauka. - 1974. - 351 p.

[31] Ripan R., Chetyanu I. Inorganic Chemistry. - Vol.1. - M.: Mir. - 1971. - 560 p.

[32] An V.V. Application of Aluminum Nanopowders for Obtaining of Nitride containing Materials. Dissertation for Obtaining of Candidate of Technical Sciences Degree. - Tomsk: TPU. - 1999. - 160 p.

[33] Gromov A.A. Nitride containing Materials Obtaining at Combustion of Ultrafine Aluminum and Boron Powders. Dissertation for Obtaining of Candidate of Technical Sciences Degree. - Tomsk: TPU. - 2000. - 197 p.

Macrokinetics of Interaction of Electroexplosive Aluminum Nanopowders with Water and Alkali Solutions

A.V. Korshunov, A.P. Ilyin
Tomsk Polytechnic University
Lenin Ave. 30, 634050 Tomsk, Russia
E-mail: androkor@mail.ru

Abstract.
Physicochemical regularities of the interaction of aluminum nanopowder, produced by the method of electric explosion of wires, with water and with sodium hydroxide solutions have been studied. Kinetic parameters of the reaction have been determined; the character of their change depending on the storage terms of the powders, solution pH and temperature has been shown. The peculiarities of the influence of the temperature mode of the reaction and pH on the degree of aluminum conversion and phase composition of the condensed reaction products have been established.

Introduction

Highly dispersed aluminum powders (submicron and nanopowders) possess a number of qualities different from those of compact metal and rough industrial powders, first of all, by high chemical reactivity which is observed in reactions with aqueous solutions, in the processes of combustion, low temperature sintering, self-propagating synthesis, etc. The increasing interest of researchers to the interaction of aluminum nanopowders with water and solutions is caused by the possibility of using this process in hydrogen power engineering, to obtain aluminum oxides-hydroxides also, which are valuable precursors of cermets, supports for catalysts, sorbents [1-3]. Regularities of the process of interaction of industrial micron powders of aluminum with water or water vapor in the mode of hydrothermal synthesis have been studied in a rather thorough way [4-7]. Thereby, the condensed products are Al_2O_3/Al composites, which chemical and phase composition, structure, mechanical properties are determined by the conditions of the synthesis. Some papers on the studying of aluminum interaction with water at before- and near critical parameters of water conditions are known. It is necessary to note that conducting the process in the notified modes is very energy costly; besides, using hydrogen in this case is connected with technological difficulties.

Using aluminum nanopowders in hydrothermal processes has obvious advantages in comparison with industrial powders: the higher degree of aluminum conversion, possibility of implementing the process at usual temperature and pressure, high reaction rate. Nevertheless, the number of papers devoted to studying the peculiarities of the interaction of aluminum nanopowders with water is not great [8-12]; the results of these researches are oftentimes contradictory and do not allow to form the complete understanding of the process regularities.

In this connection the goal of the present work has been to study physicochemical regularities of the interaction of electroexplosive aluminum nanopowders with water and aqueous solutions.

Experimental Section

In the present study there have been used passivated in the air aluminum nanopowders (ANP), produced by the method of electric explosion of wires at laboratories of High Voltage Research Institute of Tomsk Polytechnic University. In the experiment there have been used a recently obtained sample (the storage duration is less than 1 month), as well as samples being kept in a relatively hermetic package during 1-3 years. For the control experiment there have been used ASD-1 and ASD-4 industrial aluminum powders.

The characteristics of initial samples of ANP as well as of condensed products of their interaction with solutions have been determined with the help of the following methods. The values of the specific surface area have been measured with the help of BET-method according to the low temperature adsorption of argon. The phase composition was determined using X-ray diffraction (XRD) (diffractometer DRON-3M, $Cu_{K\alpha}$-radiation). Crystal phases were identified in accordance with PDF-2 data base [13, 14]. The structure parameters of Al powders and the products of its interaction with water were determined using the full-profile analysis of roentgen diffractograms [13]. The share of metallic Al in the samples was determined according to the data of differential thermal analysis (DTA) (thermoanalyzer Q600), as well as by volumetric method according to the volume of hydrogen, emitted after treating the sample by 30% alkali solution. Dispersivity and morphology of ANP have been studied by means of scanning electron microscope JSM-5500. Structure of ANP particles and the composition of their surface layer were studied with high resolution transmission electron microscope (JEOL JEM-3010 with EDS-analyzer). Particles size distribution of the samples was determined by means of

Nanosizer ZS device (Malvern Instruments) at +25°C in ethyleneglycol medium.

The values of reaction rate at different pH and temperature were determined using volumetric method on the volume of emitted hydrogen. An ANP sample (10…30 mg) was placed in a thermostated glass reactor contained 30 ml of a solution (water or diluted solutions of NaOH, and salts) and connected with a thermostated volumetric system. The stirring of the reaction mixture was performed with the help of a magnet mixer.

The heat evolution during the interaction of ANP with water and diluted NaOH solutions was measured with calorimeter controlled by computer. As a temperature detector the chromel-alumel thermocouple was used. After the completion of the reaction the solid residue was isolated, dried up at room temperature and examined with the help of the described above methods.

Results and Discussion

The ANP samples used in the study are agglomerated; agglomerate dimensions constitute up to 5…20 μm. The ANP particles are of spherical shape (Fig.1); particles distribution is monomodal in the interval 70…800 nm with the average number maximum of 120 nm; the curve of size distribution is obeyed logarithmic law. Metallic Al content in a recently obtained ANP sample according to DTA data and volumetry is about 90…94% (wt.), for the ANP samples kept within 1-3 years the share of Al decreases up to 68…75%, the rest is attributed to oxides and adsorbed substances. According to the results of roentgen-fluorescent analysis, the basic impurities in all the ANP samples are iron (up to 0.25 wt.%) and copper (up to 0.20 wt.%).

According to XRD data the basic crystal phase of the examined ANP samples is the metallic aluminum with face centered cubic lattice which parameter exceeds the standard one 0,2% in average. Metal Al crystallites size (after Scherrer) for recently obtained samples equals $L \approx 55$ nm; the L value increases in time during the storage. (Hydr)oxide phases were not indicated by XRD in the initial Al samples.

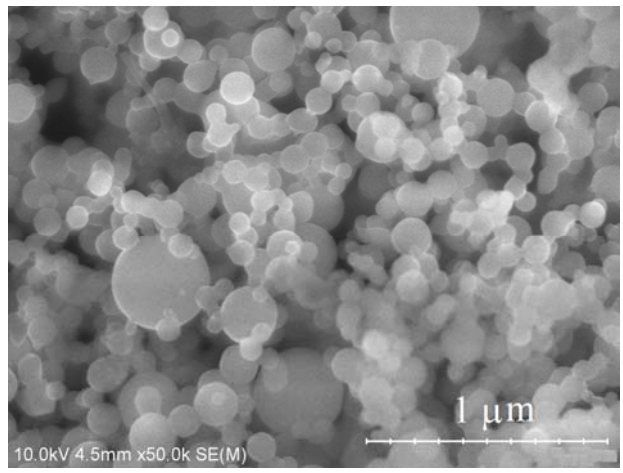

Fig. 1. SEM image of an Al nanopowder sample, produced by the electric explosion of wires.

It is known that the surface of metallic aluminum even under very low partial O_2 (~1 Pa) becomes covered with thin continuous oxide film. Because of the oxide film (10…40 nm) compact Al and industrial (micron) powders practically do not interact with water under ambient conditions and at temperatures lower than 100°C [15]. Oxideless aluminum (being treated in alkali, amalgamated, etc.) is a very active metal. Standard potentials of metal Al containing redox systems are negative at any solution pH [15]:

$Al^{3+}+3e \rightarrow Al$, $\varphi^\circ = -1.66$ V;

$AlO_2^- + 2H_2O + 3e \rightarrow Al + 4OH^-$, $\varphi^\circ = -2.33$ V.

Formation of Al hydroxocomplexes leads to a considerable shift of φ in the region of negative values, due to what metallic Al is one of the most active reductants (especially in alkali medium). In acidic and alkali solutions Al forms stable ions $[Al(H_2O)_6]^{3+}$ and $[Al(OH)_4]^-$ respectively [15]. During interaction between Al and water insoluble Al hydroxides with different degree of hydration are formed as condensed products.

In order to exclude the influence of insoluble products formation we have carried out a preliminary research of the formal kinetics of ANP interaction with diluted (0.01…0.1 M) NaOH solutions.

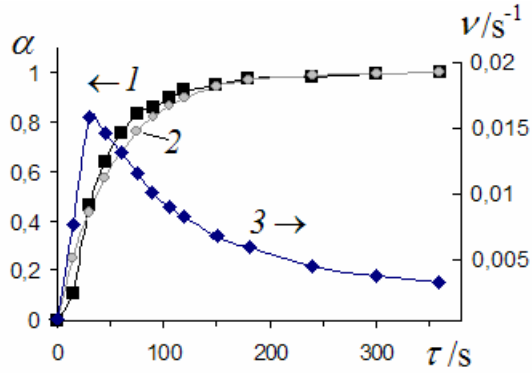

Fig.2. Dependence of ANP conversion degree α (*1* – experimental, *2* – calculated) and reaction rate v (*3*) on time τ during the interaction of Al nanopowder with 0.01 M NaOH (23°C).

According to the obtained results the reaction in alkali solutions occurs in two stages: 1) basic stage, during which the dependence of degree of Al conversion on time is close to the linear one; this stage occurs until the Al conversion degree α≈50…65%; 2) the final stage taking place at α>80%; it is obvious that at this stage there continues the interaction of the coarse particles fraction of ANP; this stage is characterized by a sharp reduction of reaction rate. Fig.2 shows the graph of $\alpha=f(\tau)$ and $d\alpha/d\tau=f(\tau)$ dependencies revealing the change of the degree of ANP conversion during the interaction with 0.1M NaOH at 23°C.

In the interval 0.01…0.1 M of NaOH concentration the process is characterized by a short (3…8 s) induction period. For all ANP samples (recently obtained, and with the term of storage 1-3 years) the maximum values of reaction rate (v_{max}) are close to each other and equal 0.024 s^{-1} on average, time τ_{max}≈30 s. Analysis of kinetic parameters of the process shows that v_{max} values do not correlate with dispersivity of initial ANP.

In alkali solutions the dependence of the degree of Al conversion on time obeys the Avrami equation [16]:

$$\alpha=1-e^{-k\tau}, \qquad (1)$$

where α –degree of conversion; τ – time, s; k –effective rate constant, s^{-1}. Kinetics of the process of hydrothermal oxidation of industrial Al powders is described similarly. In Fig.2 the calculated on eq.1 kinetic curve is shown. Linearization of the experimental data in coordinates $\ln[1/(1-\alpha)]=f(\tau)$ allows to find effective rate constant which equals 0.021±0.004 s^{-1} at 23°C. For comparison, value k for industrial powder ASD-1 under similar conditions is 25 times lower than that for ANP.

The dependence of reaction rate for ANP interaction with alkali solutions on temperature was studied in interval 25…70°C. At t>40°C reaction occurs without the induction period; the general duration of the complete conversion of Al decreases considerably.

At the increasing of temperature up to 70°C v_{max} of ANP interaction with diluted alkali solutions increases 3.5 times on average, while value of k – 2.5 times. The Arrhenius plot $\ln k$-$1/T$ is linear in the indicated temperature interval and is described by the following equation:

$$k = k_o \cdot \exp\left(-\frac{4714{,}6}{T}\right), \qquad (2)$$

where k_o=204434 s^{-1}.

The character of the dependence $k=f(T)$ indicates the invariability of mechanism of the reaction in the given temperature interval.

In Fig.3 the dependence $\alpha=f(T,\tau)$ is represented graphically as a 3D-surface (section of the surface for t>70°C is built by extrapolation). The effective activation energy E_a of the process equals 42±5 kJ/mole, on the basis of what it is possible to draw a conclusion about a mixed diffusion-kinetic control of the process.

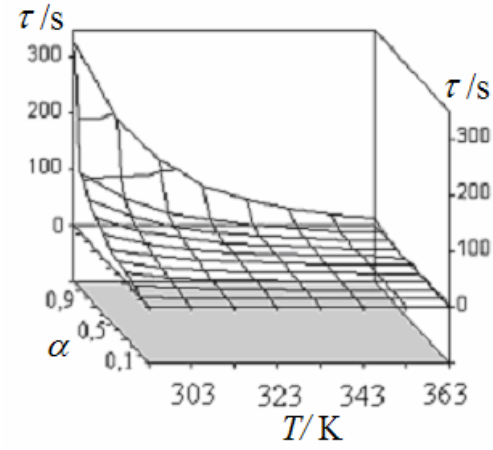

Fig.3. Graph $\alpha=f(T,\tau)$ for interaction of ANP with 0.1 M NaOH.

Calorimetric measurements of interaction of ANP and industrial powders (ASD-1, ASD-4) with diluted NaOH solutions (0.01…0.1 M) allow to find out the differences in thermokinetic regularities of the reaction with the participation of powders of different dispersivity. In Fig.4 graphs $\Delta T=f(\tau)$ are represented which reflect change in temperature during interaction of an ANP sample (50 mg) with 50 ml of 0.1 M NaOH. It is seen from the graph that the form and the position of the maximum on the curves is determined by dispersivity of powders, which in its turn determines reaction rate, and as a consequence – thermal emission rate. Because of considerable difference of ASD-1 and ANP dispersivity, temperature increase in the reaction mixture for the latter is considerably higher and the maximum is reached at

smaller τ. Calculation of ΔT value which corresponds to the mass of a given powder yields ΔT=2.33° (calorimeter constant and the heat losses caused by hydrogen removal from the system have been taken into consideration):

$$Al_{(c)}+3H_2O_{(l)}+OH^-_{(aq)}=Al(OH)_4^-{}_{(aq)}+{}^3/_2\ H_{2\,(g)},\ \Delta_r H°_{298}=-402\ kJ.$$

The calculated ΔT value corresponds well to that found experimentally for the recently obtained ANP sample (Fig.4, curve 5). For ASD-1 sample the experimental ΔT is 2 times lower (Fig.4, curve 1), which is determined by difference in the reaction rate, and as a consequence with the thermal emission rate. On the basis of these data as well as macrokinetic model of the process (eq. 2), the thermokinetic equation of the process of ANP interaction with water may be represented as follows:

$$Q_\tau - K = \Delta H \cdot n_{Al} \cdot (1 - e^{-k\tau}) = [(C_{P,sp} \cdot m)_{sol} + (C_p \cdot n)_{H_2}] \cdot \Delta T_\tau, \quad (3)$$

where Q_τ – heat evolution during time τ, J; K – calorimeter constant; ΔH – standard enthalpy of reaction, kJ/mole; n_{Al} – amount of aluminum, mole; $C_{P,\ sp}$ – specific heat capacity of solution, J/g·K; m – solution mass, g; C_P – molar heat capacity of hydrogen, J/mole·K; n_{H2} – amount of hydrogen, mole; ΔT_τ – change of temperature in calorimeter. Using eq.3 it is possible to calculate the temperature of the reaction mixture ANP+alkali solution at any time moment τ. Graph $\Delta T=f(\tau)$ built by using eq.3 practically coincides with the curve 5, Fig.4.

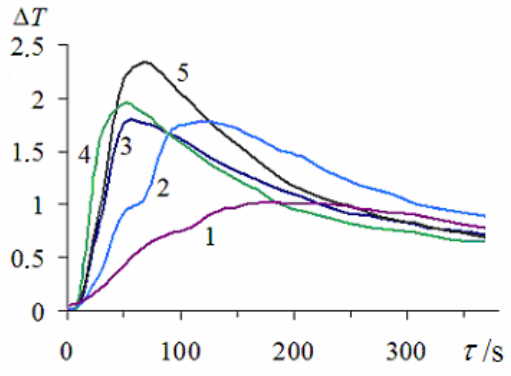

Fig.4. Curves $\Delta T=f(\tau)$ for interaction of 50 mg of a Al powder with 50 ml 0.1 M NaOH: *1*) ASD-1; *2*) ASD-4; *3,4*) ANPs with the term of 3 year storage; *5*) recently obtained ANP sample.

General regularities of ANP interaction with water somewhat differ from those of alkali solutions. In this case the process occurs in three stages: 1) induction period (initial stage), 2) basic stage and 3) final stage. The duration of the stages depends on the characteristics of initial ANP, composition of the solution, and mode of the process.

The dependence $\alpha=f(\tau)$ of the ANP interaction with water in the wide interval of temperatures is of sigmoidal shape (Fig.5). With the increase of temperature (Fig.5) the initial branch of the sigmoid is reduced (the duration of the induction period reduces sharply), thereby the shape of the kinetic curve approaches to the one for the reaction in alkali solutions (Fig.2). Reaction rate on the second stage in the interval of the conversion degree 10…55% at 55…80°C for all ANP samples practically does not depend on α. The maximum values of reaction rate are reached at $\alpha\approx35\%$; in interval 55…80°C v_{max} changes from 0.0013 up to 0.0067 s^{-1}. For comparison, v_{max} of interaction of ANP with water at 80°C exceeds the one for hydrothermal synthesis with industrial Al powders ~70 times [6]. Without taking into consideration the first stage of the process (the induction period), the chemical stage of the reaction, just as in the case regarded above concerning ANP interaction with alkali solutions, is described by equation (1). The effective rate constant of in interval 60…80°C changes from 0.0020 up to 0.0069 s^{-1}. Plot $\ln k=f(1/T)$ is linear in the given T interval, E_a equals 63±3 kJ/mole and close to that obtained in ref. [12] for mechanically activated Al in the carbon matrix. In ref. [11] there has been found value E_a=270 kJ/mole which is supposed to be scarcely possible for the process studied. According to our results, E_a values at α=12; 34 and 56% for all ANP samples in interval 55…80°C remain constant what indicates the absence of changeability of the mechanism of the process on its different stages. Taking this in account, the dependence of k on T for the reaction in water can be expressed by the following equation:

$$k = k_o \cdot \exp\left(-\frac{7240}{T}\right), \quad (4)$$

where $k_o=5.1\cdot10^7\ s^{-1}$.

Thus, from the position of formal kinetics, the ANP interaction with alkali solutions and water is described by the kinetic equation of one type; the reaction in alkali solutions occurs at mixed diffusion-kinetic control, and in water – at kinetic one. A certain resemblance of the mechanism of the processes is confirmed by the continuity of E_a values at various degrees of Al conversion in thermostatic conditions.

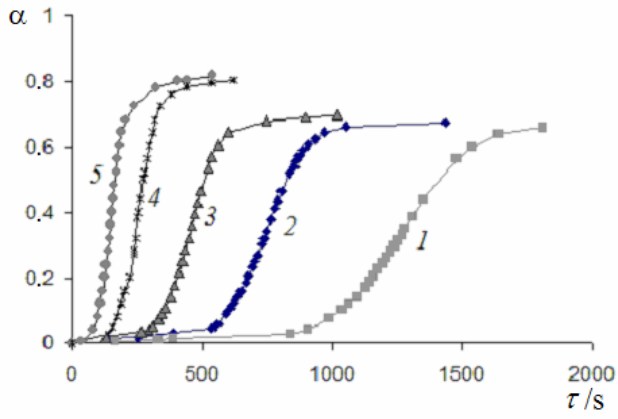

Fig.5. Dependence of degree of ANP conversion on temperature during its interaction with water at: 1) 55; 2) 60; 3) 65; 4) 75; 5) 80°C.

However, values of k in alkali solution and in water are differed to a considerable degree (eq.3, 4). For example, at 60°C k in water is 73 times lower than that in alkali solution, what is evidently determined by the different nature of particles participating in the chemical stage of the process. Moreover, the degree of Al conversion during interaction with water in the given temperature interval never reaches 100% in all cases; for example, at 80°C for freshly prepared ANP equals 93% on average, with the storage term 1 year – 82%, 3 years – 70%. The residual Al as it will be shown further by XRD is always present in solid products of the reaction.

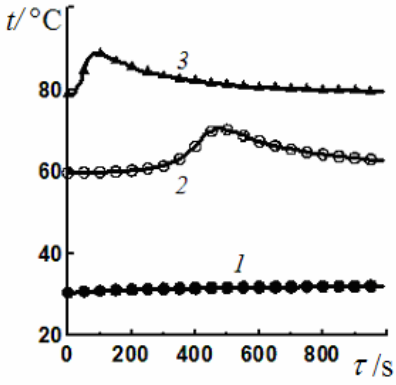

Fig.6. Plots $T=f(\tau)$ for the reaction mixture of 50 mg Al nanopowder with 50 mg of water, obtained in the calorimeter at different thermostating temperatures: *1*) 30; *2*) 60; *3*) 80°C.

Study of the thermal regime and products of ANP reaction with water in thermostatic conditions and in conditions of linear heating of the reaction mixture in the interval 30…80°C, along with kinetics experiments, allowed to make the evaluation of the temperature of the beginning of the second stage of the reaction, value of the maximum reaction rate and activation energy, as well as phase composition of condensed products of the reaction. It has been found out that the duration of induction period in thermostatic conditions practically does not depend on the mass ratio Al:H_2O. At 30°C the reaction occurs rather slowly, the induction period may reach ~1 hour for different ANP samples. The curve $T=f(\tau)$ at those conditions has a very sloping maximum (Fig. 6, curve 1). At much higher temperatures, τ_{ind} decreases (Fig. 6, curve 2, 3). Determining the heat effects by using eq.3 allows to calculate degree of Al conversion and to compare the degree with XRD data. For example, at 60°C Q=1.26 kJ, α=62%; at 80°C Q=1.89 kJ, α=70%. The obtained data correspond well to macrokinetic data, as well to the results of the analysis of the phase composition of the reaction products.

The basic phases in solid products are the residual Al, crystal α-$Al(OH)_3$ (bayerite), γ-AlOOH (boehmite), apart from that the content of the amorphous phase is considerable (17…20%), what corresponds to the data from ref. [9]. In Fig.7 a typical roentgen-diffractogram of the reaction products is given obtained during the ANP interaction with water. According to the XRD data, bayerite is well crystallized (D=150…200 nm), and boehmite is mostly in amorphous state.

Several hydroxide phases in the products are caused by their thermodynamic stability under the given conditions. In aqueous medium polymorph conversion of crystal forms of aluminum hydroxide can be presented in the following scheme [15]:

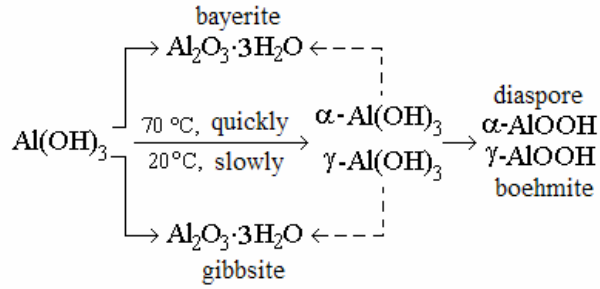

The amorphous $Al(OH)_3$ during the heating-up quickly transforms into more stable crystal orhto- (bayerite, gibbsite) and meta-forms (boehmite, diaspore). Some equations of Al reactions with water with the formation of possible stable products are given below; standard values of enthalpies (kJ per 1 mole Al) were calculated according to the data [17]:

$$Al_{(c)}+3H_2O_{(l)}=Al(OH)_{3(amorph.)}+3/2\ H_{2\,(g)}\ ,\quad \Delta_r H°_{298}=-418,$$

$$Al_{(c)}+3H_2O_{(l)}=1/2\ Al_2O_3{\cdot}3H_2O_{(bayerite)}+3/2\ H_{2\,(g)}\ ,\quad \Delta_r H°_{298}=-437,$$

$$Al_{(c)}+3H_2O_{(l)}=1/2\ Al_2O_3{\cdot}3H_2O_{(gibbsite)}+3/2\ H_{2\,(g)}\ ,\quad \Delta_r H°_{298}=-432,$$

$$Al_{(c)}+2H_2O_{(l)}=AlOOH_{(diaspore)}+3/2\ H_{2\,(g)}\ ,\quad \Delta_r H°_{298}=-428,$$

$$Al_{(c)}+2H_2O_{(l)}=AlOOH_{(boehmite)}+3/2\ H_{2\,(g)}\ .$$
$$\Delta_r H°_{298}= -416.$$

Thus, formation of various phases of hydroxides during interaction of Al with water is characterized by thermodynamic functions of one order, what explains the complexity of the phase composition of the reaction products.

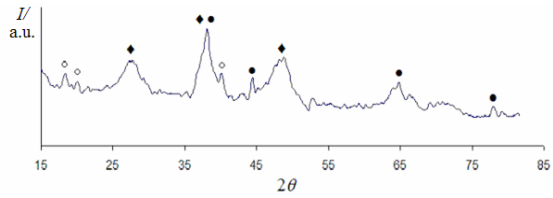

Fig.7. XRD-pattern of the solid products of ANP interaction with water at 60°C. Phase signs: ° – α-$Al(OH)_3$ (bayerite); • – Al; ♦ – γ-AlOOH (boehmite);

The XRD patterns of the solid reaction products show that the relationship of phases considerably varies depending on thermostating temperature, solution pH, and the initial reagents mass ratio. As temperature increases, the shares of bayerite and residual Al in the products are decreased, while that of boehmite is increased. The increase of the mass ratio ANP:H_2O also contributes to the increase of boehmite share. At pH>7 the degree of Al conversion is increased, boehmite share in products is decreased. The storage term of the samples also influences the products composition: for ANP samples kept >1 year, the content of the residual Al, at other conditions being equal, is three times more in comparison with recently obtained ANP samples, the content of amorphous phase is two times less, the relationship bayerite:boehmite is 1.5 times lower. It is possible to note the similarity in the porosity of the obtained at t>60°C Al (hydr)oxides; S_{sp} values measured by the BET method are about 230…250 m^2/g for all the ANP samples and they do not demonstrate any certain dependence on the mass ratio ANP:H_2O and pH.

Conclusions

1. Kinetics of interaction of electroexplosive aluminum nanopowders with diluted (0.01…0.1 M) NaOH solutions and with water follows Avrami equation. In alkali solutions the process occurs under the mixed diffusion-kinetic region, in water – under kinetic region. The values of the effective activation energy in both cases do not depend on the degree of aluminum conversion.

2. The duration of the induction period during the interaction of Al nanopowders with water is caused by the term of their storage and temperature. Kinetic parameters of the basic stage of the reaction depend mostly on temperature and change insignificantly in time during ANP storage.

3. Basic phases in the solid reaction products of the interaction of Al nanopowders with water are bayerite and boehmite, the relationship and structural characteristics of which are mainly determined by the temperature conditions of the reaction.

The research has been financially supported by the Russian Fund for Basic Research (grant № 06-08-00707).

References

[1] Yermolenko N.F., Efres M.D. Regulation of Porous Structure of Oxide Adsorbents and Catalysts. Moscow, 1991. 360 p.
[2] Godymchuk, A.Yu., An, V.V., Ilyin A.P. *Physics and chemistry of materials treatment*. **5** (2005) 69.
[3] Ilyin A.P., Korshunov A.V., Tolbanova L.O. *Proc. Tomsk Polytech. Univ*. **4** (2007) 10.
[4] Zhilinsky V.V., Lokenbakh A.K., Lepin' L.K. *Proc. Ac. Sci. Latvian SSR. Chemistry series*. **2** (1986) 151.
[5] Tikhov S.F., Romamenkov V.E., Sadykov V.N. et al. *Kinetics and Catalysis*. **5** (2005) 682.
[6] Bakumenko O.M. PhD thesis / Kharkov Univ. Kharkov, Ukraine. 2003.
[7] Rat'ko A.I., Romamenkov V.E., Bolotnikova E.V., Krupen'kina Zh.V. *Kinetics and Catalysis*. **1** (2004) 154.
[8] Proskurovskaya L.T. PhD thesis / Tomsk Polytech. Univ. Tomsk, 1988.
[9] Lyashko A.P., Medvinsky A.A., Savel'ev G.G., at al. *Kinetics and Catalysis*. **4** (1990) 967.
[10] Gadzhiev C.N., Ilyin A.P., Kertman S.V., Khasanov O.L. *In «Phisical chemistry of fine powders»*. P.1. Tomsk: High Voltage Res. Inst., TPI. 1990.
[11] Ivanov V.G., Safronov M.N., Gavrilyuk O.V. *Combustion, explosion, shock waves*. **2** (2001) 57.
[12] Streletsky A.N., Kolbanev I.V., Borunova A.B., Butyagin P.Yu. *Colloidal Journal*. **5** (2005) 694.
[13] Kovba L.M., Trunov V.K. Roentgen phase analysis. Moscow, 1976. 231 p.
[14] PDF 2 database, 1996, International Centre for Diffraction Data, Newtown Square, Pennsylvania, USA.
[15] Tikhonov V.N. Analytical chemistry of aluminum. Moscow, 1971. 266 p.
[16] Delmon B. Kinetics of heterogeneous reactions. Moscow, 1972. 556 p.
[17] Lidin R.A., Andreeva L.L., Molochko V.A. Constants of inorganic substances. Moscow, 2006. 685 p.

The nonsteady burning rate of high-energy materials

Arkhipov V.A.*, Bondarchuk S.S., Korotkikh A.G.*****

* Research Institute of Applied Mathematics and Mechanics of Tomsk State University, Tomsk, Russia

******– Institute of Chemical and Energy Technologies Problems of the SB RAS, Biysk, Russia

***– Tomsk Polytechnic University, Tomsk, Russia

Research of burning nonsteady modes of high-energy materials (HEMs), containing aluminum powder, is of interest both from the scientific point of view, and for practical applications. Studies of the ignition and slaking processes, as well as of the transient behavior of burning, the low- and high-frequency instability of burning ,as well as of the nonsteady burning rate (NBR) are necessary for the creation of change speed solid-propellant rocket engines of small traction and for engines of multiple burns for control systems of spacecraft. Experimental data under characteristics of the specified modes will allow to deepen existing representations of the nonsteady combustion theory [1] with reference to new class HEMs.

In the present work measurement results of nonsteady burning rates of HEM mixtures on the basis of ammonium perchlorate, combustible binder SKDM-80 and aluminum powder of various dispersivities are presented occurring at a sharp pressure dump in the combustion chamber. The investigations were performed on cylindrical structures with different volume-to-surface (V/S) ratios The pressure dump was realized by opening an additional nozzle during combustion of a fuel plug. The installation diagram is listed in work [2]. The burning rate determination during the transient period was performed by a method of high-speed shooting and by problem statement and solution of corresponding inverse problem internal ballistics (IPIB-method) with use of technology of direct search [3]. The analysis of experimental data on nonsteady burning rate of HEMs is given here.

Experiments were spent at a variation of initial pressure $p_0 = (1.9 \div 6.4)$ MPa, a combustion surface $S = (41 \div 79.5)$ cm^2, a volume of combustion chamber $V = (637 \div 809)$ cm^3 and a speed of pressure dump $\left|dp/dt\right|_{\max} = (30 \div 400)$ MPa/s.

Results of NBR measurements during dump of pressure by a method of high-speed filming are presented in fig. 1. Depending on value $\left|dp/dt\right|_{\max}$ two modes can be seen – quasi stationary change $u(t)$ for $\left|dp/dt\right|_{\max} \sim (30 \div 40)$ MPa/s and full slaking for higher values of pressure dump speed. For the first mode of burning (fig. 1*a*) certain fluctuations of $u(t)$ are characteristic. The amplitude of fluctuations makes up to 10 % from quasi stationary dependencies $u_{qst}(t)$ and frequency of fluctuations during dump of pressure is about (45 ÷ 70) Hz. With an increase of pressure dump speed up to $\left|dp/dt\right|_{\max} > 180$ MPa/s full slaking (fig. 1*b*, *c*, *d*) was observed. For these cases $u(t)$ shows similar characteristics. In an initial stage there is a sharp decrease of burning rate then (in the middle of transient) $u(t)$ increases by factors of $2 \div 4$, accompanied by frequency fluctuations in the range of 25 ÷ 100 Hz, and later – full slaking. Extinction time depends on parameter $B = p_0^{-1}\left|dp/dt\right|_{\max}$ (fig. 1*b*, *c*, *d*). The received results correlate with the data [4] received for HEMs on the basis of ammonium perchlorate and combustible binder HTPB, measured by the microwave frequency method.

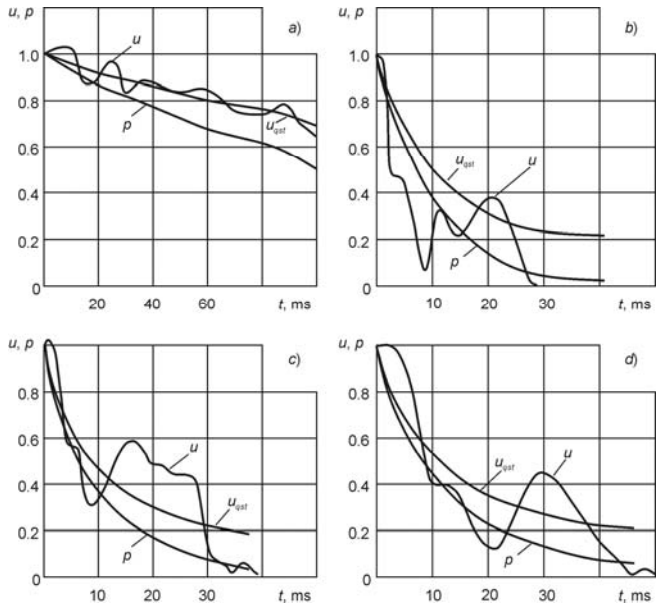

Fig. 1. Measurement results of nonsteady burning rates for cylindrical structures of HEM mixture by high speed filming:

a – $p_0 = 4.7$ MPa, $\left|dp/dt\right|_{\max} = 30$ MPa/s;

b – $p_0 = 1.9$ MPa, $\left|dp/dt\right|_{\max} = 186$ MPa/s (slaking);

c – $p_0 = 2.9$ MPa, $\left|dp/dt\right|_{\max} = 294$ MPa/s (slaking);

d – $p_0 = 5.9$ MPa, $\left|dp/dt\right|_{\max} = 400$ MPa/s (slaking)

For the investigated structures of HEM mixtures two modes of NBR are found out at pressure decay – quasi stationary change $u(t)$ at $\left|dp/dt\right|_{\max} \sim (30 \div 40)$ MPa/s and full slaking for higher values of pressure dump speed. For mixture structure «failure» on a mode of nonsteady combustion occurs at much smaller $\left|dp/dt\right|_{\max}$ than for homogeneous propellants. The basic influence on nonsteady combustion and blackout of HEM renders a mode of granular diffusion combustion of an oxidizer and combustible binder.

Use of the IPIB-method for measurement of nonsteady burning rate of HEM mixture structure has yielded results differing from the received methods of filming. In fig. 2 experimental dependencies $u(t)$ are presented received by two methods under identical conditions. The divergence of results is caused by the fact that the IPIB-method gives mean values $u(t)$ for the whole burning surface, whereas the filming method gives a local burning rate at separate points of surface. It is a principal cause of divergence, as the burning surfaces of HEM mixture structures show a much higher heterogeneity of the burning surface compared to homogeneous propellants.

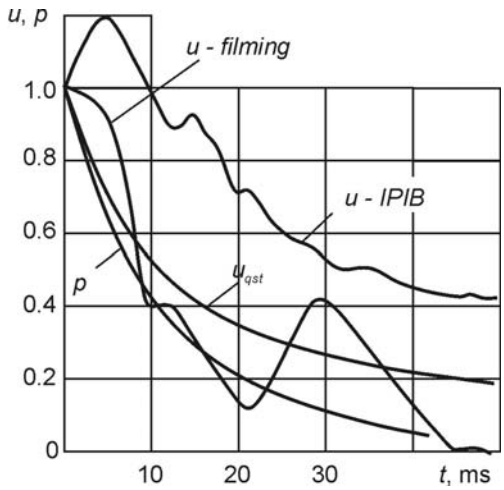

Fig. 2. Comparison of measurements results of HEM mixture structure by a method of high-speed filming and the IPIB-method for identical conditions (p_0 = 5.9 MPa, $\left|dp/dt\right|_{\max}$ = 400 MPa/s)

The analysis of the experimental results performed for HEM mixture structure has allowed to reveal some laws regarding slaking of propellants. It has been shown that slaking of HEM mixture structure occurs in a range of values $B_{cr} = (67 \div 150)$ s^{-1}. From that value on B_{cr} is essentially influenced by the geometric parameter V/S. So, at values V/S = 13 ÷ 20 cm a value of $B_{cr} = 67 \div 101$ s^{-1} has been received and at V/S = 7.7 cm, $B_{cr} \geq 140$ s^{-1}. In other words slaking occurs with increasing parameter V/S at smaller speeds of pressure dump.

REFERENCES

[1] Zeldovich Ya.B., Lejpunsky O.I., Librovich V.B. The theory of nonsteady combustion of gunpowder. Moscow: Nauka, 1973. 176 p.

[2] Arkhipov V.A., Bondarchuk S.S., Korotkikh A.G., etc. Nonsteady effects at burning high-energy nanopowder composite // Proc. of the High School. Physics. 2007, No. 9/2. P. 3–11.

[3] Arhipov V.A., Zimin D.A. The analyses of applicability conditions of inverse methods of restoration of nonsteady burning rate // Combustion, Explosion, and Shock Waves. 2000. V. 35, No. 3. P. 39–43.

[4] Strand L.D., Schultz A.L., Reedy G.K. Microwave Doppler technique for determining solid propellant transient regression rates // Journal of Spacecraft and Rockets. 1974. Vol. 11, No. 2. P. 75-83.

Nano-ingredients for rocket propulsion: performance evaluation and diagnostics

L.T. DeLuca, L. Galfetti, F. Maggi, G. Colombo, A. Bandera, S. Cerri, L. Merotto, L. Rossettini and P. Donegà
Politecnico di Milano, Dipartimento di Ingegneria Aerospaziale, SPLab
Campus Bovisa, I-20156 Milan, Italy

Abstract

A survey is offered of the results of a five years old experimentation carried out at the Space Propulsion Laboratory of Politecnico di Milano in the field of nanoingredients insertion inside rocket motors propellants (mainly solid): in the recent years, in fact, a great interest arose in replacing commercial microaluminum with nanoaluminum inside solid propellants compound, which has proved to increase the regression rate significantly. In this work a complete characterization of several nanoaluminum propellants compositions, in comparison with standard microaluminum formulations, both with AP and AN as oxidizer, will be given: both the steady and transient burning behavior will be considered. Moreover, a nanometric positive catalyst (Fe_2O_3) has been tested in comparison with standard micrometric ones in our laboratory. All the results seem to state a positive effect of nanoingredients in solid propellants performance and a different flame structure compared to standard microsized ingredients.

NOMENCLATURE

Roman symbols

Al^0	=	metallic aluminum
Al_2O_3/Al^0	=	aluminum oxidation efficiency
Al_{ox}	=	aluminum oxide
A_s	=	burning surface
D_p	=	particle diameter, μm
D_{43}	=	mass mean diameter, μm
D_{AP}	=	mean ammonium perchlorate grain size, μm
I_s	=	specific impulse, s
$I_{s,ideal}$	=	ideal equilibrium specific impulse, s
n	=	steady burning rate pressure sensitivity
nAl	=	nanometric size Aluminum
k	=	ignition delay heat flux sensitivity
p	=	pressure, bar
q	=	heat flux
r_b	=	steady burning rate, mm/s
t_{ign}	=	ignition time, ms
$(t^*)_{cc}$	=	average residence time in combustor, ms
$(V_{cc}/A_b)_{1/2}$	=	combustor free volume / burning area ratio at half burning time, m

Greek symbols

ΔI_s	=	specific impulse loss, s
η_{c^*}	=	efficiency of characteristic velocity, *%*
η_{cs}	=	efficiency of thrust coefficient, *%*
η_{Is}	=	efficiency of specific impulse, *%*
μAl	=	micrometric size Aluminum
ρ_{cc}	=	combustor gas mixture density, g cm^{-3}
ρ_p	=	propellant density, g cm^{-3}

Abbreviations

AP	=	Ammonium Perchlorate
AN	=	Ammonium Nitrate
CCPs	=	Condensed Combustion Products
EEW	=	Electric Explosion Wire
HTPB	=	Hydroxyl-Terminated Polybutadiene
MM	=	Mechanical Milling
MOPs	=	Micrometric Oxide Particles
PC	=	Plasma Condensation
SEM	=	Scanning Electron Microscopy
SOPs	=	Smoke Oxide Particles
SRB	=	Solid Rocket Booster
TMD	=	Theoretical Maximum Density
XPS	=	X-Ray Photoelectron Microscopy
XRD	=	X-Ray Diffraction

BACKGROUND

Solid propellants still play today, and will continue to play in the future, an important role in primary and sometimes auxiliary propulsion for space exploration: compared to liquid systems they can assure higher value of volumetric impulse and thrust, even if at a price of a lower specific impulse. The specific impulse is the main performance parameter for a rocket motor, being the inverse of the specific consume, and is defined as the thrust divided for the weight flow rate of propellant. The volumetric impulse is the specific impulse times the density of the propellant, and it gives the idea of the energy stored in any volume unit of the propellant: the high density of solid propellants, compared, among the others, to Hydrogen and Oxygen, makes them fully attractive for large motors (as the one needed for Earth escape). Just an example of this trend is the recent testing by NASA of the first stage of Ares I light launcher (a five-segment solid rocket derived by the Shuttle SRB), meant to carry the crew and light cargo for next ISS missions as well as support the Ares V heavy launcher in the framework of the future Constellation program. A solid rocket propellant is a mixture of oxidizer and fuel powders: AP is the most frequently used oxidizer, while microaluminum is the common fuel. The powders are entrapped in a binder (usually HTPB). AN, which is a "greener" ingredient than AP because of its reduced HCl emission, is another possible oxidizer, but its usage is strictly limited by the low burning rate deriving; the

burning rate of the propellant is the first governing parameter a motor designer has in his hands to tailor the performance as the mass flow rate (that multiplied by the exhaust velocity gives the thrust value) descends linearly from this (note that the dependency of thrust from the burning rate is not linear, as the exhaust velocity, as well, depends from the burning rate through the pressure). An impressive number of investigations, carried out all around the world during last decades, aimed at improving the currently standard AP/Al/HTPB compositions by means of new chemical ingredients (including new oxidizers, nanopowders, burning catalysts, etc.). The recent production techniques development and availability of nanoaluminum powders have made them attractive to replace standard micrometric aluminum used as fuel in many propellant compositions. This paper points out new directions using the nano-ingredients based propellants currently tested in our laboratory, in order to obtain burning rate enhancement, keeping an eye at the same time on the effect on the pressure sensitivity n: the burning rate is in fact linked to the pressure level through a power law with exponent n ($r = a*P^n$, known as Vieille law). n is an important parameter for the stability of the motor system, and its typical value for application ranges from 0.3 to 0.45. Besides the burning rate, a great interest lies in the evaluation of the specific impulse losses because of Two-Phase (2P) flow: standard AP/Al/HTPB and AN/Al/HTPB give rise, during the combustion, to large condensed phase combustion products, which provoke performance losses in the nozzle because of the thermal and velocity lag they propose compared to a purely gaseous flow. It is expected that nano-ingredients, nanoaluminum at least, should reduce the agglomeration level, thus making these losses less important and improving the specific impulse efficiency. Moreover, more recently, a new nanometric combustion catalyst (Fe_2O_3) has been tested and compared to standard micrometric one. In fact, the burning rate of AP composite propellants is increased by the addiction of small percentages (usually in the order of 1 %) of catalysts which act to increase the decomposition rate of AP particles: since catalysts are effective on the surface of AP, the total surface area of catalysts is the most important factor in achieving a good effect of catalysis, thus making clear the advantage of a small sized catalyst powders.

Metal Fuels

Metal powders, usually aluminum, are one of the common ingredients of solid rocket propellants: compared to a non-metallized composition, in fact, they enhance the motor ballistic performance in terms of density, combustion stability and specific impulse; metal addition leads to an increase of flame temperature which largely compensates the enlargement of the average molecular mass, which in the end results as an increase of the exhaust gases velocity and therefore, of the specific impulse. However, the combustion of metal powders involve a series of complex phenomena, which lead to the formation of condensed combustion products (CCPs), which damps the benefic effect of metal powders: in fact, this yields partial combustion and slag collection in the combustion chamber, throat section erosion and two-phase flow losses due to the enlarged thermal capacity and reduced inertia of the flowing mixture. All this in the end conduce to a perceivable losses of prevented specific impulse. The evolution of CCPs starts on or near the burning surface and leads to particles agglomeration, and prosecutes in the two-phase flow in the supersonic nozzle.

Aluminum Combustion and Agglomeration

The "life" of metal (i.e. Aluminum) particles on the burning surface is subjected to a variety of entraining or adhering forces, which push them to leave, move and eventually coalesce: in fact, combustion may involve both group and single metal particles, leading, through an heterogeneous and homogenous process, to the formation of small oxide particles. CCPs are usually classified in terms of particle diameters: they are labeled agglomerates if the diameter is larger than the initial metal nominal one (D_p > 15-45 μm); intermediate micrometric oxide particles, MOPs, in the range between 1-2 μm and the size of agglomerates (MOPs, 1~2 μm < D_p < agglomerates); intermediate micrometric oxide particles, and smoke oxide particles (SOPs, D_p < 1~2 μm). These three families have different origins too: agglomerates are mainly spherical burning particles made up of unburned Aluminum (Al^0) and Alumina (Al_2O_3) and have a time-variant structure and present several different variants; Micrometric oxide particles are originated from the transformation of the oxide cap, formed on each agglomerate during combustion, into a single oxide particle after full Al consumption [1]. Smoke oxide particles are generated by the homogeneous combustion of Al particles not participating in the agglomeration process and that of agglomerates in the gas phase. Their role becomes evident if one considers that about 70-80% of the original particles leave the propellant surface individually, thus giving birth to the smoke oxide particles population [2]. Moreover they can be considered the most universal population of CCPs, as they are less dependent on the propellant formulation than their larger "brothers"[3][4]. It has been previously stated that the insertion of metal powders inside a propellant matrix is benefic for instability attenuation too, because of the augmented thermal inertia and acoustic damping: in particular SOPs are effective in damping high frequency oscillations above 4000 Hz, while larger particles are effective in damping low and middle frequency oscillations (MOPs can damp instabilities around 500 Hz)[5]. The phenomena occurring in and near the burning surface and eventually leading to the agglomeration have been a major topics for years in the field of solid propellants [6][7][8]: an important factor for agglomerates to form and grow is the presence of a skeleton layer; this is a gas-permeable three-dimensional structure consisting of metal, oxides, and carbonaceous elements originated by the binder decomposition, occupying the upper part of the propellant burning surface (carbon skeleton). During the combustion, this fuel mould emerges on the burning surface in the zones among the large oxidizer grains (pockets). During binder and oxidizer decomposition process, the metal particles warm up and reach the burning surface. In this phase aluminum particles are still covered by an alumina coating. Metallic Aluminum and Aluminum Oxide have different thermal expansion coefficients and melting temperatures (T_{melt_Al2O3} = 2345 K, T_{melt_Al0} = 933 K); as a consequence, when Aluminum melts and becomes liquid it undergoes a volume augmentation because of the augmented density, which can in the end break the oxide layer and let the aluminum inside spread out. These effects lead to the formation of aggregates of irregular shape ("clusters" of elongated shape) on the burning

surface [9][10]. In a first phase only aggregates of irregular shape are observed, then through a progressive heating of the aggregates, accumulation on the burning surface and protrusion into the warmer regions of the gas-phase, inflammation and particles coalescence a single drop is formed with the characteristic round shape as it is visible in Fig. 1.

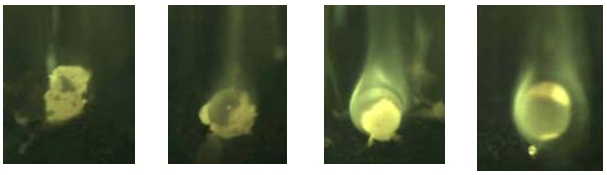

Fig. 1: Aggregates formation and evolution to agglomerates.

After formation, the particles continue to grow on the burning surface until final detachment. Typically, agglomerates are born on the surface of the skeleton layer and, after detachment, are entrained into the gas-flow where they evolve until the end. Some forces oppose to the agglomerates detachment, that is the presence of a liquid binder layer which tends to entraps the particles till it is completely gasified and the possible presence of porous carbonaceous material on the surface (this is the case when AN is used as oxidizer). From what has been briefly reported above it emerges clearly that propellant formulation plays an important role in the agglomeration process, both because of a possible different chemical composition and a grain size distribution. For micro aluminized propellants it has been widely accepted that agglomerate size depend mainly on AP coarse fraction size: however a reduction of the agglomerates size is expected when replacing microaluminum with nanoaluminum as an early detachment from the burning surface of the forming agglomerate can be forced by the faster combustion, close to the burning surface, because of the higher temperatures of that zones; the coalescence process is quite more effective because of the greater reactivity of nanopowders coming from their huge specific surface but the absence of a liquid binder reduces the residence time. This great reactivity makes possible that a larger part of metallic Aluminum burns very close to the burning surface, provoking a local increase of temperature, which in the end results in the prevented burning rate increase.

Iron Oxide Catalysis

It has been already stated that the burning rate of AP composite propellants is greatly amplified by the addition of catalysts which increase the rate of AP decomposition and that the total surface of catalytic element is the subsequent crucial factor. As catalysts both fine iron oxides (Fe_2O_3 and Fe_3O_4) and organic iron compounds can be used. In general the degree of the burning rate increase is proportional to the amounts of catalysts when the total amount of catalysts is less than about 3%, and is saturated at about 5% [11]. Other possible catalysts could be copper oxides, but the thermal stability of the propellants is largely lowered and spontaneous ignition could occur, making them not suitable for applications. Organic iron compounds are quite more effective than iron oxides, but the latter are the most commonly used in applications because of their easiness of handling and relatively low cost. The new frontier of nanosized iron oxides promises to bridge the gap in terms of performance with organic iron compounds, and this work will try to supply the first data on this subject.

Plan of Presentation

This work will report the results of the substitution of microaluminum with nanoaluminum inside a standard AP/Al/HTPB propellant: a lot of aspects will be investigated, concerning both the static and dynamic behavior of propellant; great emphasis will be initially given to the burning rate characterization and ballistic properties of identical recipes propellants but with different size of aluminum powders, and also to an estimate of the diameter of agglomerates, carried out through the optical analysys of high-resolution visualizations recordings. Detailed information about the agglomerate mean diameter and agglomerate histograms at different pressures is obtained. Properly combining a variety of diagnostic techniques revealed surprising differences in the flame structure of apparently similar formulations. Later the transients of ignition and extinguishment will be presented, concerning ignition delay, pressure deflagration limit (PDL) and fast depressurization, always tracing a comparison with a commercial aluminum based propellant. In the second part of the paper some short results concerning the effect on the ballistic properties of nanoaluminum on AN and AP-AN mixtures based propellants will be given. The last part of the paper will deal with nanometric and micrometric iron oxide comparison, as catalysts for solid propellants. Conclusions and clues on current developments close the paper.

AP-nAl BASED FORMULATIONS

Burning Rate

Several Aluminum powders of various sizes, both micrometric and nanometric, have been used as fuel in propellants with analogous composition (AP/Al/HTPB, 68/15/17 in mass percentage), produced directly in our laboratory. The AP distribution was monomodal in the range 80-140 μm. The characteristics of the Aluminum powders used are summed up in Table 1.

Table 1: Tested Aluminum Powders

Powders Label	Size (μm)	Bet (m^2/g)	Coating	Technique of production
Al-02a	0.127	17.50	-	EEW
Al-01c	0.135	16.40	-	EEW
Al-04a	0.363	6.10	Hydrocarbon	PC
Al-05	22.15	0.10	-	MM

The aluminum labeled Al_05 is a standard commercial micrometric one, already used in boosters of real motors. To perform the burning rates tests the propellants were cut in parallelepiped shape (5x5x30 mm), and were coated with Paraloid to inhibit lateral combustion and then dried for more than 24 hours at ambient temperature; the combustion takes place in a closed vessel where an inert atmosphere of Nitrogen is created. During the combustion

the pressure is kept strictly constant by a system composed of a piezoresistive pressure transducer, a software as pressure controller and electro valves as actuators. The ignition of the strand is demanded to the usual hot wire technique, while the combustion videos are recorded by an high-speed camera, which permit a proprietary software (elaborated in our group by Dr. Filippo Maggi) to calculate the burning rate by means of a brightness gradient analysis. The whole experimental set-up is shown in Fig. 2.

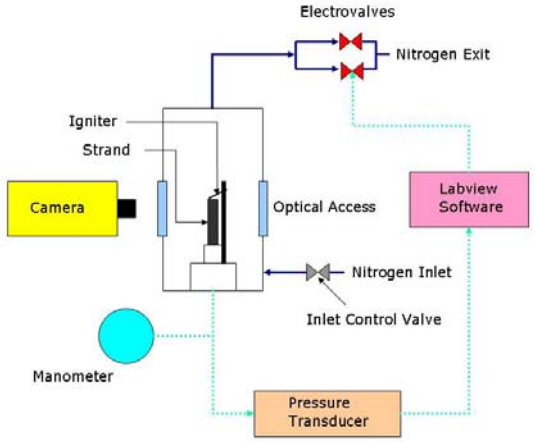

Fig. 2: Burning rate experimental set-up

The results obtained are depicted in the following Fig. 3 where the Vieille laws for all the propellants analyzed are shown.

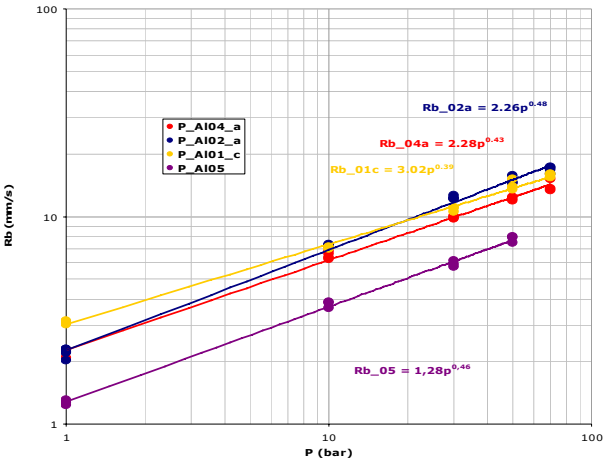

Fig. 3: Burning rate results (Conti, SPLab)

It is evident that the propellants with nano-aluminum are much faster than the standard aluminum based one (3 times higher at every pressure level). However, in spite of the relatively large range of investigated specific surfaces, from 0.1 to 17.5 m^2/g, no obvious effect on the pressure sensitivity power *n* could be detected over the explored range of parameters, as confirmed by [5]. In the absence of ballistic anomalies and in the range of pressure 1-70 bar, possible fluctuations of *n* are likely due to (uncontrolled) changes of other properties and possible propellant manufacture imperfections. The results illustrated in Fig. 4, reporting the burning rate as a function of BET for different pressure levels for the powders investigated and two more micrometric powders, indicate a regular increase of burning rate with increasing specific surface under all tested pressures, thus confirming the faster burning rate of nAl. A direct analysis of Fig. 2 and Fig. 3 permits to define the following scenario: solid propellants formulations containing nAl particles exhibit higher burning rates as the size of the particles falls down, that is to say for high particles specific surface. Size, however, is not the only governing parameter: the importance of the relative amount of metallic Aluminum (Al^0) and Aluminum Oxide is to be taken into consideration.

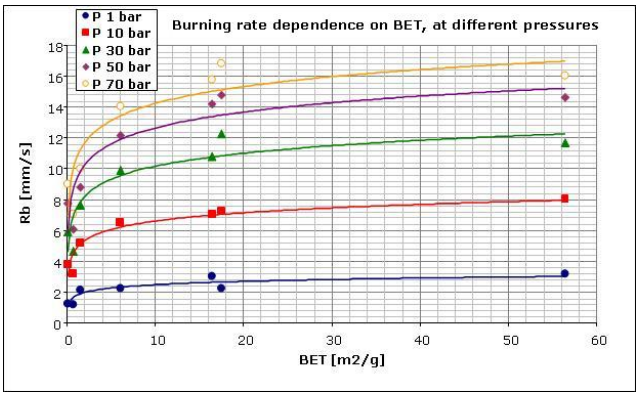

Fig. 4: Burning rate as a function of BET (Conti, SPLab)

Table 2: Metallic Aluminum Atomic Concentration

Powders Label	Al^0 (%)	Al_2O_3 (%)	Oxigen (%)	Corresponding Propellant Pressure Sensitivity
Al-02a	32	30	35	0.48
Al-01c	47	25	27	0.38
Al-04a	63	13	19	0.43
Al-05	72	15	12	0.46

Table 2 displays the atomic concentration of metallic Aluminum, Aluminum Oxide and Oxygen for the powders under investigation, as obtained from XPS after 12 minutes of sputtering: metallic aluminum content increases with the particle size, as the oxide layer is always realtively thin but never becomes slimmer than tenths of nanometers, and its volume fraction on the particle becomes significant for small particles. Al-01c has a much larger metallic Aluminum percentage than Al-02a, in spite of their being very similar in size, and this is probably the origin of the behavior of the propellants at low pressure: Al-01c based is nearby two times faster than Al-02a at 1 bar; the larger amount of Aluminum can probably crack faster the oxide layer, thus making ignition easier. This effect is reduced at high pressure where the burning process is so fast that the difference in concentration becomes trivial and the specific surface returns to be the governing parameter. The high burning rate at low pressure for Al-01c is consequently responsible of the low pressure sensitivity of the corresponding propellant. Al-02a has an oxide layer thickness very similar to that of Al-04a. That's probably the reason for their low pressure behavior being so similar, while, once again, at high pressure the particles size is restored in its leading role. Moreover, Al-04a is the only coated powder, which prevents "cold agglomeration" of particles.

The effect of particles size on the pressure dependency becomes more evident in the sub atmospheric pressure range. At this purpose two different propellants were investigated, with the same (AP/Al/HTPB, 68/18/14) nominal composition, but different Aluminum size, one being a micrometric powder and the other nanomteric (AP was monomodal smaller than 71µm). The features of these powders are reported in Table 3.

Table. 3: Tested Aluminum Powders

Powders Label	Size (µm)	Shape	Coating	Technique of production
Al-01a	0.15	Spherical	-	EEW
Al-06	50	Irregular	-	MM

Al-06 is a micrometric Aluminum powders, currently not used in applications because of its bad shape regularity. The results obtained are shown in Fig. 5. The confirm of the accelerating effect on nAl is evident, even for low pressure levels, but a new element is the strong reduction on pressure sensitivity (-33%).

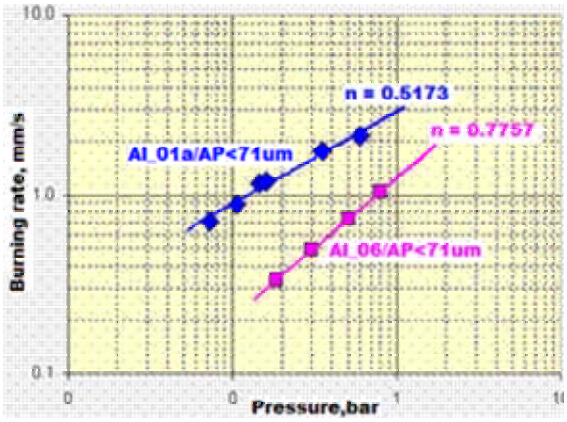

Fig. 5: Sub atmospheric burning rate results (Colombo, SPLab)

It should, however, be remarked that testing was purposely carried out in the subatmospheric pressure range, where typically µAl propellant burning shifts from a diffusion to kinetics controlled combustion, thus increasing its pressure sensitivity to higher values. In addition, if pressure keeps on decreasing approaching the propellant PDL value, the steady time-invariant deflagration wave is replaced by a steady self-sustained oscillatory deflagration wave. Under these circumstances, the Vieille fitting laws actually refers to the average burning rate vs. pressure. In other words the effect of nAl on the pressure sensitivity, even in sub atmospheric range, is still under debate.

Visualization of Aggregation/Agglomeration and Diameter Evaluation

The purpose was to investigate in detail the growth mechanism of the condensed combustion products due to the aggregation / agglomeration process taking place on / near the combustion surface. Combustion tests in the range 1 to 30 bar were performed in a horizontal combustion chamber with optical accesses. Ignition was performed by an hot wire. Combustion was in a nitrogen atmosphere with the pressure regulated by an automatic control system. Recording of tests was performed with a high-speed and high-resolution video system with a long-range microscope; the light was given by a cold-light source. Video camera was focused at about 5 mm from the beginning of the sample in order to exclude the burning transient. Size calibration was repeated several times for each test session. Qualitative and quantitative information were obtained comparing the agglomeration processes featured by different propellants. A measurement of the agglomerates size, detaching from the surface, can be performed directly from the observation of the video, after proper calibration (see Fig. 6)[12][13]. This easy technique, when performed manually by a single operator, permits only to gain qualitative information, in terms of comparison between different formulations, because of the limited number of measurement that is reasonable to do for each video (at this purpose an automatic software is under development today in SPLab).

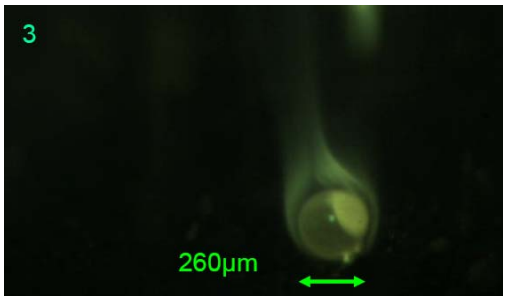

Fig. 6: Agglomerate size Evaluation Example (SPLab, Maggi)

For each video a number of tests equal to 100 is usually performed and histograms of (average) agglomerate sizes were obtained, under each testing condition. The experimental set-up used is shown in the following Fig. 7.

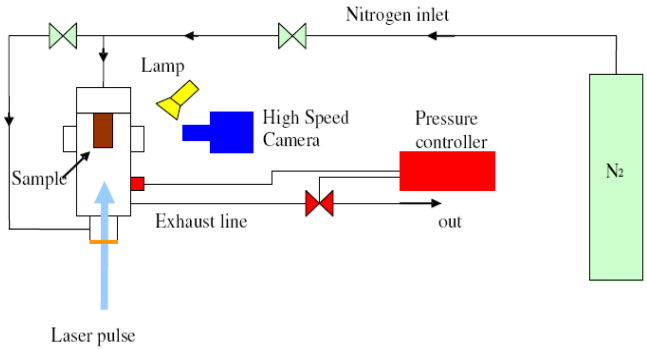

Fig. 7: Visualizations Experimental Set-Up

This technique is a well-established technique in SPLab, and has been made possible by the last generation high-speed camera used, which was forced to work at 3000-4000 Hz and 1/20000 s exposition time, in order to obtain the requested time resolution. An example of the typical output of this procedure is reported in Fig. 8, for a µAl based propellant: together with a the histograms, the granulometric curve (representing the percentage of probability to find a particle larger than a fixed diameter) is proposed.

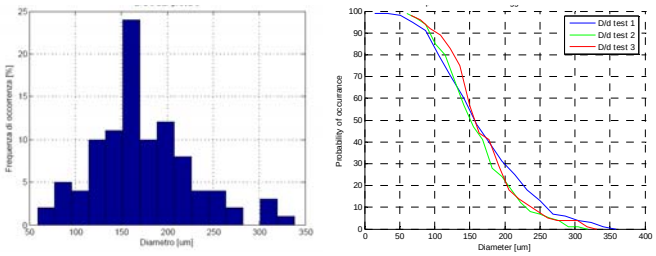

Fig. 8: Typical Agglomerates Size Evaluation Technique Output (SPLab, Maggi)

When this approach was applied to the nAl based propellants making use of the powders Al-01c and Al-04-a no presence of agglomerates was found; moreover the shape of the aggregates, the pre-agglomeration stage is quite peculiar in the case of nAl as it is shown in Fig. 9. These aggregates emanate from the propellant, grow on the burning surface, accumulate, and protrude into the adjacent gas-phase until detachment. With respect to nAl, the aggregate structure for µAl propellants looks different, implying some transition time or thickness before triggering agglomeration. This is not the case for nAl based propellants: the aggregates have a coral-like structure and never, or almost never, evolve into the spherical agglomerates typical of µAl [14], leaving the surface in the form of flakes whose size is in the order of 50 µm. An evidence of agglomeration was recognized in a propellant with the same nominal recipe but including Al-03b, which is a five time larger Aluminum powder, thus suggesting the existence of a boundary level of size under which no complete agglomeration can take place, at least near the burning surface where the high-speed camera can fix its glance.

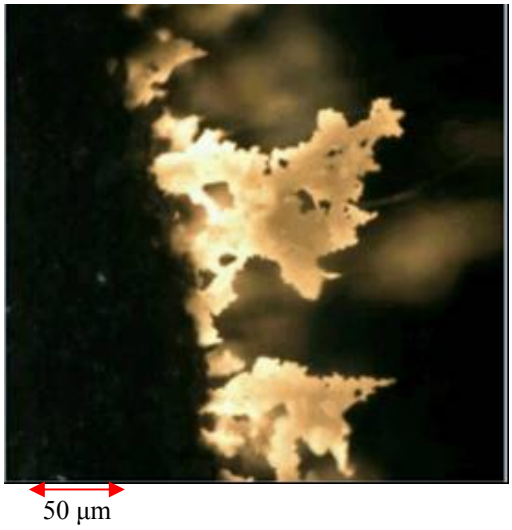

Fig. 9: nAl based propellant aggregate (SPLab, Maggi)

The histograms representing the results for this propellant are reported in Fig. 10, for the pressure levels investigated of 1, 5 and 10 bar. The most populated family of agglomerates in for all cases is the 80 µm. Just to fix the ideas, an industrial µAl based propellant has typically agglomerates in the size of 150 µm or larger in the same pressure range investigated. The knowledge of how large the agglomerates are is of basic importance if one considers that all the methods for performance losses ($\Delta I_s = Is_{,ideal} - I_s$) prediction in real motors are based at least in part on this information; two are the main causes of losses, that is the losses for two-phase flow in the nozzle and the ones due to incomplete combustion of the metal; both of them are usually predicted by means of correlation between the motor and the agglomerates sizes (and are enhanced with increasing agglomerates size), the operating conditions and some experimental correlation constants (note that for the performance losses in the nozzle the exhaust diameter is the main parameter)[15col]. The main size of agglomerates, before the new generation high-speed camera permitted to correctly monitor their evolution, was estimated in their turn through operative conditions and motors sizes or burning rate and oxidizer percentage weight correlations [16][17]. During this phase the residence time inside the combustion chamber (t^*_{cc}) must be estimated as well: it can be simply evaluated as the ratio between the total mass of volume occupied by the hot gases and the mass flow rate produced by the combustion, which leads to the simple expression: $t^*_{cc} = V * \rho_{cc} / (\rho_p r A_s)$. In any case, however, nanoaluminum should reduce specific impulse losses because of the reduced, if any, size of the agglomerates it produces. It could be noted that the theoretical estimate of residence time is in agreement with what experimentally found: the higher burning rate leads to reduced residence time and consequently low agglomerates size could be expected; and small agglomerates, or more often, no complete agglomerates at all, is what has been experimentally found in our research. The tendency of nAl based propellant not to generate agglomerates has been confirmed in our group by a series of visualizations tests in sub atmospheric pressure ranges.

Ignition Delay

In this section the different behavior during ignition of nAl compared to µAl based propellants will be analyzed: the reduced dimension of nanoaluminum with respect to micrometric fuel promotes a more intense heat release close the burning surface, and a consequently reduced time to obtain ignition of the corresponding propellant is expected. The capability of nano-powders to be ignited more easily at relatively low temperature was confirmed by a preliminary series of experimental tests, where the powders where heated by a laser beam till the ignition was detected and the corresponging temperature was reocrded (the pressure was always 1 bar in air), whose results are reported below:

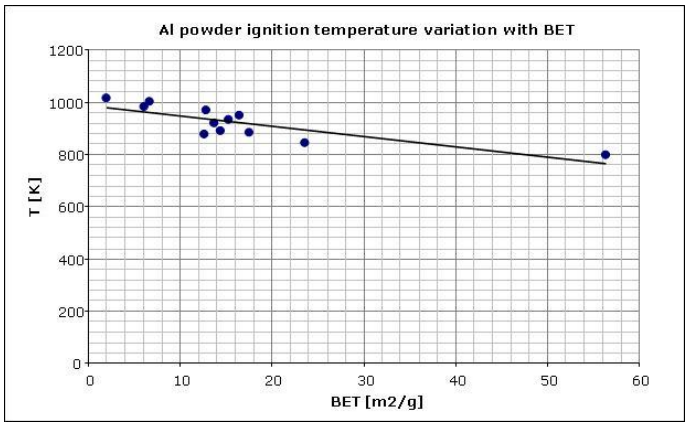

Fig. 10: Aluminum powders ignition temperature as a function of BET (SPLab, Merotto)

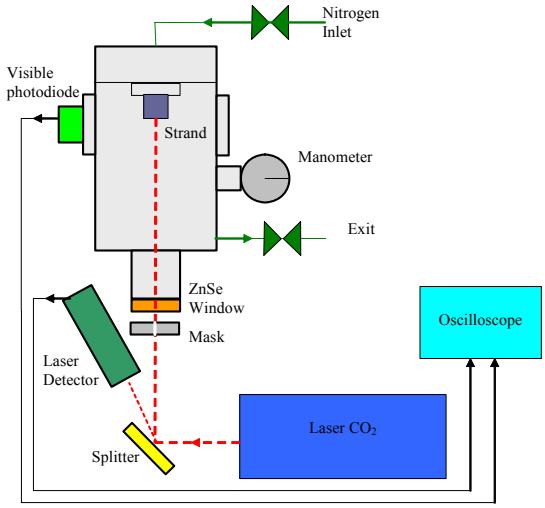

Fig. 11: Ignition Delay Experimental Set-up

It is clearly visible the decreasing of the ignition temperature moving from the micrometric powders to the nanometric ones, with the ignition occurring even 200 K before for the tiniest. The ignition delay is the time needed by a propellant to obtain self-sustained ignition under an external heat source, which usually is a laser beam. According to the classic theory the ignition time under constant impinging flux can be expressed as $t_{ign} = a\, q_r^{-k}$, where a is an experimental constant and k is predicted to be equal to 2 by solving the problem of heating an inert body to a critical temperature[18][19][20][21][22]. It has been widely experimentally shown that in reality k is never equal to 2, because of possible in-depth chemical reaction and absorption of light. The ignition behavior of AP-based solid rocket composite propellants, with or without micro-Al powders, was reviewed by Lengellé et al. [23]: available data were re-elaborated on a standard bi-logarithmic plot suggesting a value of k higher for nAl than for µAl, thus suggesting a greater dependency on the heat flux, which in turn confirms the larger reactivity of nAl powders. In our experimentation, which takes place in the experimental set-up depicted in Fig. 11, the combustion chamber has an internal volume of 2 litres, and the CO_2 laser used to ignite the propellants (cut in parallelepiped shape of 5x5x2 mm) enters the chamber through a ZnSe window, which is transparent to the 10.6 µm radiation. The chamber is, as usual, fed with a nitrogen atmosphere (10 bar). The signal from a laser detector is acquired by a digital oscilloscope, which, moreover, receives the signal coming from a photo-diode, operating in the visible range of radiation, facing the window of the combustion chamber. The time between the laser firing, supplied by the laser detector, and the start of combustion, readable from the photo-diode signal, is referred to as the ignition delay.

The propellants investigated were the usual (AP/Al/HTPB, 68/15/17 in mass percentage, with Aluminum powders labeled Al-01c, Al-02a, Al-04a and Al-05, see Burning Rate section for details). The results obtained in terms ok the coefficient k, in the heat fluxes range investigated which span from 100 to 250 W/cm^2 are reported in Table 4 and in Fig.

Table 4: Tested Aluminum powders and results

Powders Label	Size (µm)	Bet (m^2/g)	Corresponding Propellant Heat Flux Sensitivity
Al-02a	0.127	17.50	1.09
Al-01c	0.135	16.40	0.84
Al-04a	0.363	6.10	1.31
Al-05	22.15	0.10	0.55

The results show ignition delays for nAl based propellants almost always lower than µAl based, with a tendency at dilating this gap toward high impinging fluxes, because of the confirmed tendency of nAl to supply higher dependency on the heat flux, which makes their lines more vertical. A somewhat countertendency effect is established by the ignition delay of Al-04a propellant for low laser flux: its ignition delay seems to be much higher than Al-05 one (which is micrometric) and is also responsible for its huge value of k, which breaks the tendency to k reduction as particle size increase. Disregarding this data its value for k would be equal to 1, in much closer agreement with the expected trend.

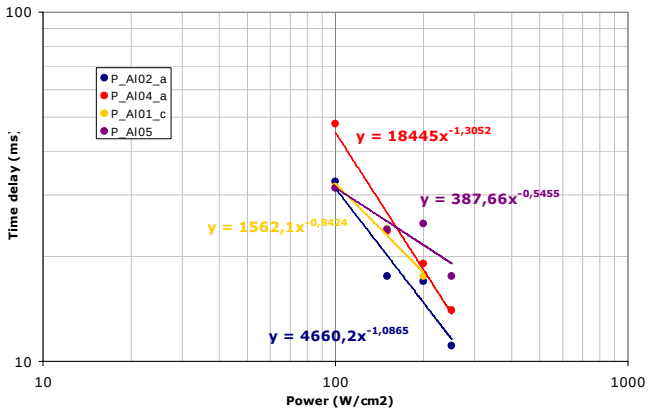

Fig. 12: Ignition Delay Results (SPLab, Conti)

Summing up, nAl based propellants exhibit lower ignition delay compared to the analogues micrometric Aluminum fueled ones, and a more evident dependency on the heat flux. Both these results are in good agreement with what was expected considering the intrinsically more energetic behavior of these powders.

Pressure Deflagration Limit (PDL) and Fast Depressurization

Besides ignition, the flame extinguishment as well is supposed to magnify the differences between microsized and nanosized Aluminum, when used as fuel in solid propellants. The PDL is the pressure level where the combustion becomes no more self sustained: when the pressure is smoothly reduced the combustion, at a certain pressure level, becomes more and more unstable (with partial extinguishment and abrupt re-firing) and oscillatory (as witnessed, for example, by photodiodes) till the final value (PDL) is reached where we have complete extinguishment. PDL is an interesting topic for basic research but it is no use as a possible strategy for real motors shut down: for this purpose, it is more suitable the dynamic effect of a high negative pressure gradient (it is a technique used in real applications). Merkle et al. [24] are among the few who systematically tested the effects of aluminum addition to a variety of ammonium perchlorate (AP) - based solid rocket propellants, but limited to micro-Al studyng the fast depressurization effect on the propellant combustion stability. No sensible difference was found by testing different micro-Al contents up to 15% and different micro-Al types (16 and 120 μm sizes). Nanoaluminum is supposed to have a strong effect both on PDL and on fast depressurization continuous burning-extinction boundary, because of its more energetic combustion which should help the propellant combustion to resist to "extinguishment forces". In our group both PDL and fast depressurization effects were tested, while comparing μAl and nAl as fuel for solid propellants. The PDL experimental set-up is composed of a large volume bomb (40 litres), capable to damp the pressure oscillations typical of near PDL burning, photodiodes, a pressure transducer and a void pump. After ignition of the strands, long enough to permit the application of tiny pressure gradient (1 mbar/s), the pressure inside the chamber is slowly reduced by means of the void pump. The following mechanism can be recognized observing the signals of the photodiode and the pressure transducer: the central part of the combustion is characterized by decreasing pressure, while the photodiodes show a reduction of frequency of the oscillating combustion and an increase in amplitude; when the flame extinction is reached, the signal from the photodiode falls to zero, while, at the same time, the pressure curve changes its inclination because there is no gas production. The pressure of the slope modification is the investigated PDL value (Fig. 13). For a given formulation the intrinsic but only ideal value of PDL actually corresponds to a sample of infinite geometry. The importance of the border effects can be assessed by the shape factor, defined as the ratio between the specimen cross section area and the cross section perimeter: as the shape factor increases (that is as the specimen becomes larger in section) the PDL tends to decrease. Our experimentation has correctly reproduced this trend (Fig. 14); moreover, nAl has strengthened the combustion making it resist to much lower pressure levels (2-3 times lower). The propellants investigated were AP/Al/HTPB, 68/18/14, (AP monomodal lower than 71 μm) using as fuel the nanometric Al-01a (0.15 μm) and the micrometric Al-06 (50 μm), whose characteristics are summed up in Table 3.

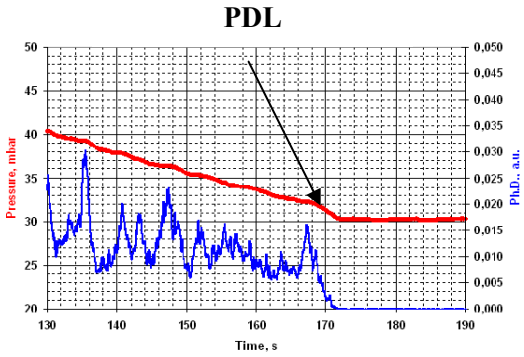

Fig. 13: Photodiode and Pressure Transducer Typical Curve

Note that the gap between nAl and μAl based is decreasing as the shape factor is increasing, that is moving toward the ideal conditions of infinite sample. The observed stronger resistance to extinction, for propellants using nAl instead of μAl, can be checked also under transient operating conditions. Three different propellants were tested: two making use of the same Al-01a and Al-06 aluminum powders of PDL experimentation, but in the percentages AP/Al/HTPB 68/15/17, and a non-metallized AP/HTPB propellant in the percentage 80/20. The depressurization tests were performed in an experimental rig realized at CNR-IENI Laboratory. A detailed description of this set-up can be found in Dondè et al. [25].

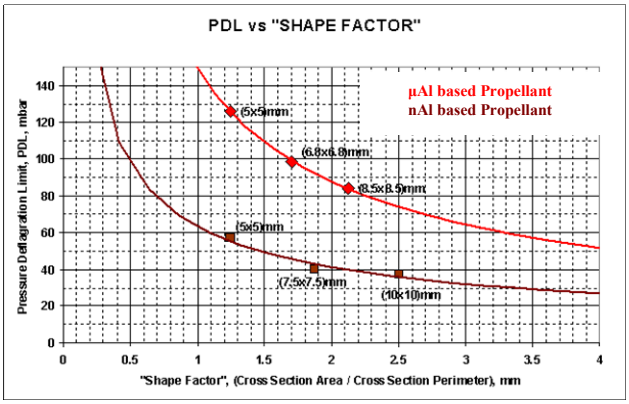

Fig. 14: PDL results

Three main parts compose the rig: a windowed combustion bomb (1050 cm^3), a double burst disk depressurization apparatus and a discharge tank. Pressure transducer permit to monitor the pressure fall, whose gradient can be modified by different exhaust orifices. After a fixed time from the ignition of the strand, during which the static burning rate is measured with the usual optical technique, the pressure gradient is imposed by means of a diaphragms rupture. The initial depressurization rate was taken as indicative of the disturbance strength. Either extinction (labelled "no go" test) or continuous burning (labelled "go") of the propellant sample gives the overall result of the pressure transient. The go/no-go data are plotted in terms of initial depressurization rate vs. initial pressure. A straight line was found to separate extinction from burning region in this plot, as correctly reported by Ciepluch and DeLuca [26][27][28] .

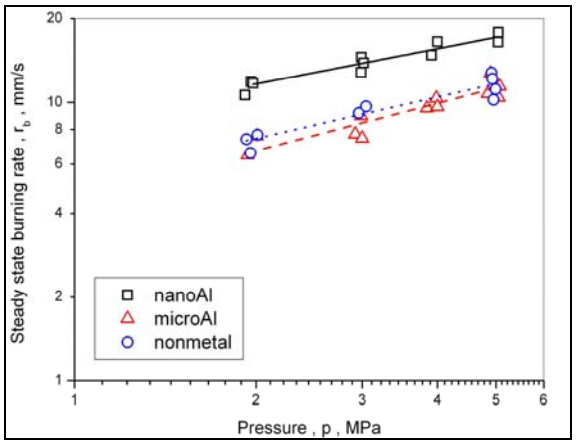

Fig. 15: Static Burning rate results

From the analysis of the Fig. 15 and Fig. 16 the following results can be extrapolated: first of all, we found a confirmation of what our experimentation on static burning rate had already pointed out, that is the benefic effect that nAl has on the burning rate. Where an increase between 50 and 100 % was discovered for all the pressures; moreover, the burning rate increase leads, considering constant thermal diffusivity of the condensed-phase, to the decrease of the propellant thermal wave characteristic time (≈ 75 % lower), thus suggesting a prompter reaction of the propellant to any kind of disturbance.

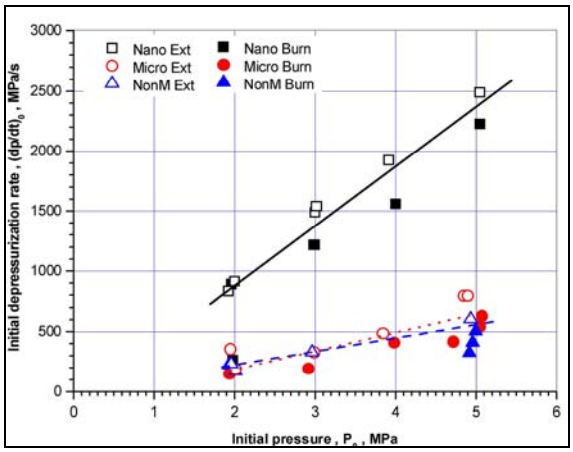

Fig. 16: Fast Depressurization Results

According to this, the significant effect of aluminum nanoparticles is not limited to steady state burning rates, but should be reflected also by the resistance to extinction of the propellant. In fact, the present experimental tests revealed a great increase of the depressurization rate needed to extinguish the propellant: in general a 4/5 times higher depressurization rate is necessary, moving from the same initial pressure level, to obtain extinguishment when nAl replaces μAl inside the propellant recipe, thus confirming the more energetic and stabilizing effect of nanoAluminum, already sufggested by PDL and ignition delay results. The result by Merkle et al è[24], suggesting a no evident different behavior when μAl is used compared to a non-metallized has been confirmed by our experimentation.

Surface Morphology of Aluminized Formulations

The unburned and quenched surface of both nAl and μAl based propellants were observed by means of SEM and EDX techniques: SEM technique permit to gain information about propellant morphology , while EDX supplies also qualitative information about Aluminum and Chlorine distribution. The following Fig. 17 and 18 are graphical elaboration of the images which permit to evidence in green the Chlorine and in red the Aluminum distribution, overlapped to a surface morphological map.

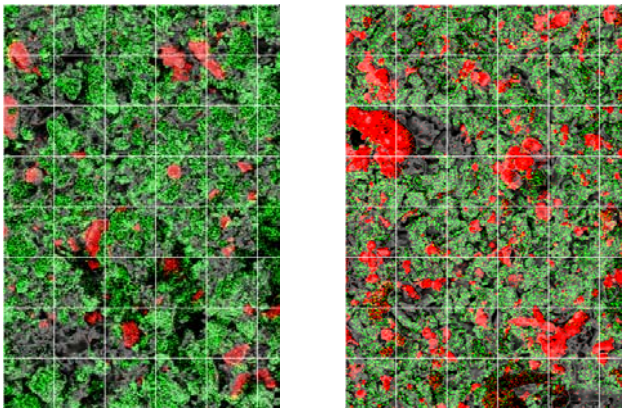

Fig. 17: SEM and EDX visualizations of Unburned (on the left) and Extinguished (on the right) surface of μAl based propellant (SPLab, Cerri-Rossettini)

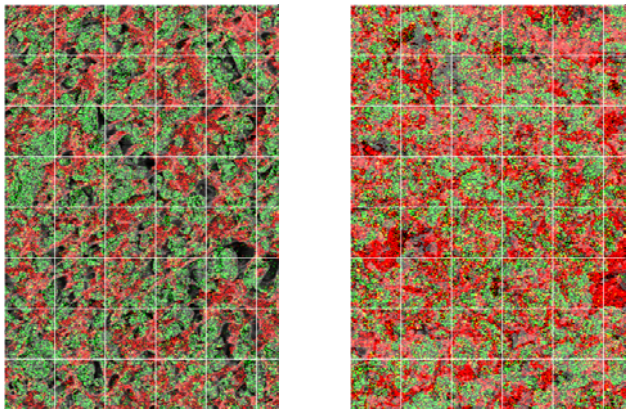

Fig. 18: SEM and EDX visualizations of Unburned (on the left) and Extinguished (on the right) surface of nAl based propellant (SPLab, Cerri-Rossettini)

As far as the μAl based propellant is considered it is evident the presence on the burned surface of grey zone with lack of Chlorine and Aluminum, parts that are probably occupied entirely by the binder; moreover, it is evident that while Chlorine is distributed uniformly on the burning surface, Aluminum is confined in large clusters in the form of flakes; the original unburned surface has a quite similar appearance. In the case of nAl based propellant, one can immediately note that in both unburned and extinguished surfaces Aluminum is more uniformly dispersed on the surface, with a lower tendency to accumulate in pockets. A regularizing effect of combustion is, in any case, evident making the Aluminum distribution even more uniform and less oxidizer surrounding, as it is on the unburned surface. Moreover, after combustion the zones purely occupied by the binder are much less evident. The following conclusions can be inferred: the combustion tends to make surfaces appearance (and therefore chemical species distributions) much more uniform, but even the unburned surface has a level of uniformity much higher than a μAl based has.

nAl Vs. μAl: a final review

Our direct comparison of equally aluminized formulation has shown a general trend for faster burning rates, quicker ignition and reduced agglomeration when nAl is used instead of μAl as fuel in solid propellants. This is in great agreement with what is known in literature. All this effect descend from the more intense heat release near the burning surface, which in turns, favors high burning rate and reduced agglomerates size: in fact, also aggregation and subsequent agglomeration phenomena are different, leading to the peculiar form of coral-like flakes for agglomerates of nAl based propellants, in contrst with spherical agglomerates typical of μAl based. Moreover, the size for μAl based propellants agglomerates is higher than for nAl, thus provoking possible specific impulse losses. In fact, aluminum occupies the regions (pockets) surrounded by the coarser AP. Within these three-dimensional regions, aluminum agglomerates to liquid burning spheres of varying size. Typically, the initial size is around 150 μm for μAl based (decreasing while flowing through the nozzle) and 80 μm or lower for the flakes of nAl based propellants. The more effective energy release of nAl is confirmed by its transient burning behavior, which leads to reduced ignition delay and a stronger resistance to extinguishment "attempts" (PDL and fast depressurization effects).

AN and AP/AN nAl BASED FORMULATIONS

Ammonium Nitrate (AN) is an inorganic oxidizer already used in rocket propulsion, and it is still nowadays a candidate oxidizer as it yields, with standard fuel and binder, environmentally safe combustion products [29]; Solid propellants used in the heavy space launchers, in fact, release after combustion a large amount of substances toxic and polluting. In particular compositions based on AP release ½ mole of chlorine for every mole of AP decomposed; subsequently chlorine reacts with other elements released during the combustion and generate several dangerous substances. moreover, AN, because of its large diffusion as fertilizer, is relatively low cost, at least compared to AP. Therefore, in the frame of the recent research for reduced cost space launchers, the ballistic properties of AN based propellant have been widely investigated. However, with respect to AP, AN present a series of contraindications which have limited strongly its application in space propulsion. Among these, its high hygroscopicity (AN crystals easily absorb water, thus suffering a decrease of density and mechanical properties), low density and limited oxidation capacity (its decomposition monopropellant flame has a lower temperature than AP) must be cited. But even more important are the polymorphic phase transitions and subsequent volumetric changes which create elevate mechanical strains on the propellant. Particularly important is the transition which take place at 305.4 K, very close to the ambient temperature. The combustion surface appearance is different too: a liquid melting layer accompanies AN combustion, making retention forces on the forming aggregates/agglomerates quite more effective, which in the end lead to the generally noted larger size of AN agglomerates (Fig. 19). All these lead to generally lower ballistic performance, in particular, AN based propellants are affected by low burning rate, not efficiently tailored with particle size, high pressure sensitivity (a too high value of n can make the motor dangerous), high PDL and low reactivity at low pressure and a general bad quality of combustion. In the end AN based motors supply lower real specific impulse levels compared to analogous AP based motor. Before becoming attractive for applications the overall level of AN based propellant must be raised to AP based levels. One possibility could be using mixtures of the oxidizers (AN/AP mixtures) and simultaneous replacement of μAl with nAl. If one considers the high cost of nAl the benefit of reduced cost of AN might be lost. For this purpose Aluminum mixtures, partly micrometric and partly nanometric in different percentages, have been considered too. Moreover, to solve the problem of phase transitions, Phase Stabilized Ammonium Nitrate (PSAN, in which the use of additives to modify the crystalline lattice prevent the phase transitions) has been proposed in literature [29][30]. In this paper the results obtained by SPLab group on both AP/AN and AP/PSAN mixtures, making use of nAl or nAl/μAl mixtures, will be reviewed in terms of burning rate.

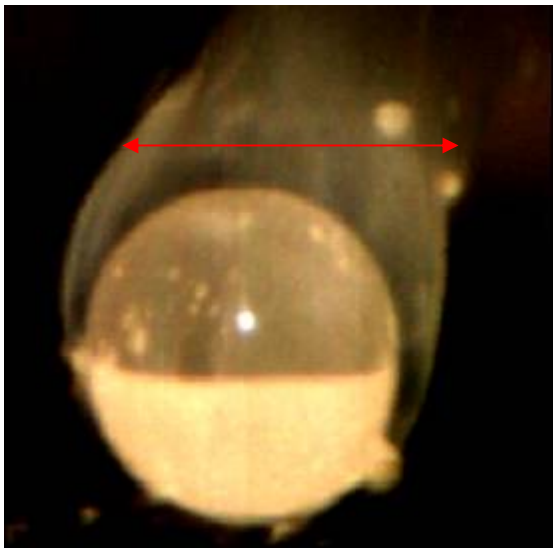

Fig. 19: AN typical agglomerate (SPLab, Maggi)

AN/AP mixtures results

In this section the results obtained on a series of propellants with the same nominal composition, but different Aluminum size, are reported: the oxidizer total amount is always 68 % in mass of the propellant, with 40 % being AN smaller than 200 µm and 28 % being AP in the size range between 80 and 140 µm. The metallic fuel is the 18 % in mass for all the propellants, but the powders size was varied according to the following procedure: the first propellant has pure Al-05b Aluminum (micrometric, see Table 1); in the others, steps of 10 % (up to 40 %) of micrometric Aluminum were replaced by nanometric Aluminum Al-01a (see Table 3). The combustion took place in the experimental set-up depicted in Fig. 2, and covered the range of pressure between 20 and 50 bar. The beneficial effect that the partial substitution of µAl with nAl has on the burning rate are evident on Fig. 20, with augmentation up to 150 %, moving from the pure µAl to the 40 % nAl composition. Roughly speaking, at high pressure (50 bar), the 40 % nAl propellant is only 10 % slower than a commercial AP/µAl propellant. Much contrasted, once again, is the effect of nAl on the pressure sensitivity, which does not define a fixed trend with the increase of the nAl percentage; note, in any case, that when dealing with mixtures of AN/AP the pressure sensitivity is the 50 % higher than for pure AP propellants.

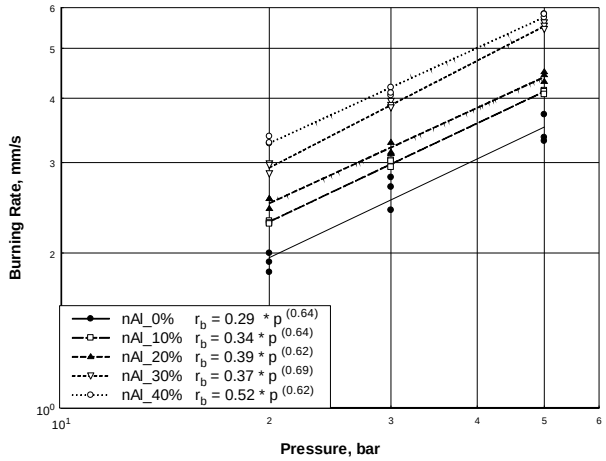

Fig. 20: AN/AP-µAl/nAl mixtures burning rate results (SPLab, Levi)

The positive effect on burning rate of nAl was, for AP/AN mixtures too, accompanied by a massive reduction of the agglomerates size as witnessed by Fig. 21, all coming from combustion at 5 bar: the presence of the oxide cap is very clear, together with the reduction of size while increasing the nAl contribution. The determination of the agglomerates population has been carried out with the usual optical technique, even tough on a reduced number of samples, and has once more confirmed the role of nAl as condensed phase particles size reductor (Fig. 22). A clear reduction of the particle size is achieved even when a low fraction of nAl is used (10 %), in particular for low pressure. The decreasing size of agglomerates with the pressure has been correctly reproduced in all cases, even if the nAl heavy filled propellant seems to be pressure insensitive, in terms of agglomerates size.

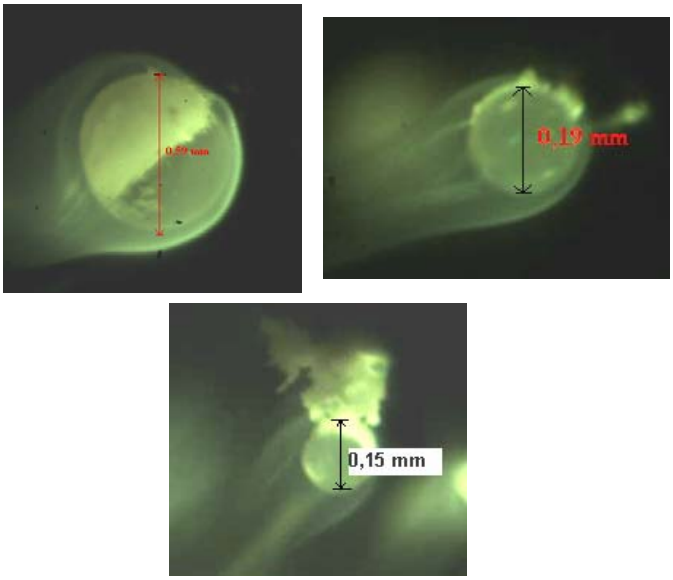

Fig. 21: AN/AP-µAl/nAl mixtures agglomerates: 0 % nAl on the top left; 10 % nAl on the top right; 30 % nAl on the bottom (SPLab, Levi)

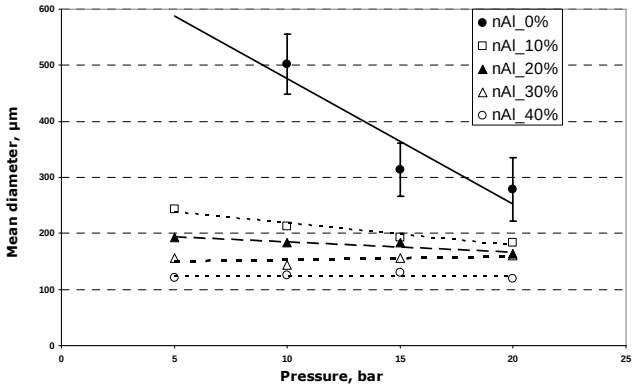

Fig. 22: Agglomerates size as a function of pressure

PSAN/AP mixtures results

In this section the SPLab results on the effect of nAl on the burning rate on AP/PSAN mixtures are presented. In particular the effect of a partial substitution (20 %) of µAl (Al-06, see Table 3) with nAl (of the usual Al-01a type, see Table 3) on a AP/PSAN/Al/HTPB 28/40/18/14. The stabilized Ammonium Nitrate used was labeled PSAN5, and it was obtained by means of 3 % $K_2Cr_2O_7$, 1 % $Mg(NO_3)_2$ and 1 % KCl to a 95 % AN. For more details

about PSAN5 and a general survey of all the stabilized Ammonium Nitrates used in SPLab see [29][31][32]. The effect of nAl introduction is less evident than in other cases, with an increase of the burning rate never higher than 10 %; A direct comparison with the 20 % nAl rich formulations based on standard Ammonium Nitrate (Fig. 20) show a consistently lower burning rate augmentation when PSAN is used. A slight increase of the ballistic coefficient was detected when inserting nAl, in a general frames of values of n lower than those of AN/AP mixtures.

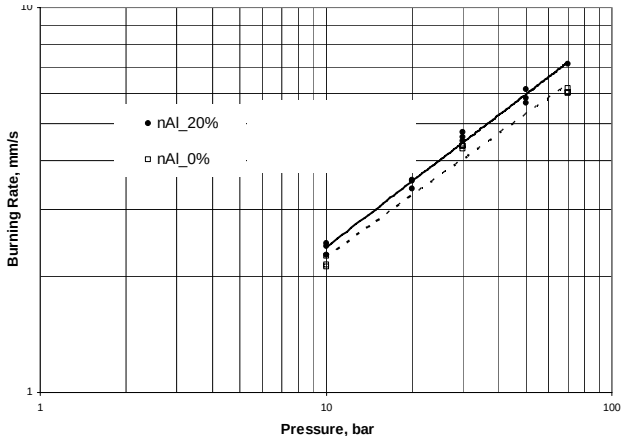

Fig. 23: PSAN/AP burning rate results (SPLab, Signoriello)

Pure AN SPLab experimentation

In an early stage of its experimentation, pure AN oxidizer were tested (without any AP inclusion): analogous propellants were tested, where the only difference was the Aluminum size (Al-05 and Al-01a, Table 1 and 3). These propellnts were in the composition AN/Al/HTPB - 68/15/17; both these propellants exhibited peculiar burning behavior: the µAl based propellant burns leaving, under a certain pressure level (usually in the order of 50 bar), a carbonaceous skeleton of the same size of the original strand, in which all the metal and the binder are substantially unreacted: the decomposition of AN is not energetic enough to promote pyrolysis of the binder and metal oxidation. When nAl replaces µAl something different happens: in all the pressure range investigated (varying from 1 to 70 bar), after the combustion a skeleton remains, but its composition is quite different from the previous case: it is made mainly of Aluminum Oxide (witnessed by the bright white color), and no trace of metallic fuel can be seen (Fig. 24). Obviously it is a nonsense to define a burning rate for this propellant. These results have forced SPLab to move towards AN/AP mixtures and disregard pure AN based propellants.

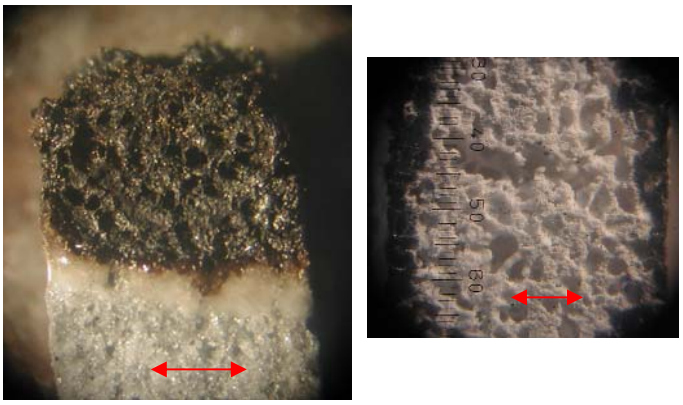

Fig. 24: Combustion skeleton for µAl (on the left) and nAl (on the right) (SPLab, Galeotta-Taiariol)

NANOMETRIC IRON OXIDE SPLab EXPERIMENTATION

In SPLab several kinds of Iron Oxides have been recently tested as ballistic modifiers inside propellants recipes. Iron oxide is, in fact, a catalyst of thermal decomposition of Ammonium Perchlorate at high temperature. Ammonium Perchlorate decomposition is, in general, extremely sensitive to the action of catalysts. Theses additives can accelerate the low temperature decomposition of the salt and consequently reduce the deflagration delay time. This high decomposition rate eventually leads to high regression rate of the compositions of propellants including AP: this stimulated a lot of studies on the solid propellants ballistic modifiers, among which, industrially, Iron Oxide is the most frequently used (both U.S. and European heavy launchers make use of Fe_2O_3 in their solid rocket boosters). It is reported in literature that the efficiency of the catalysis is increased by a massive reduction of oxide particles moving from micrometric to nanometric size (Ref. 138 art. Nuovo). These authors also put in relationship the specific surface of the catalyst with and its capability to promote Ammonium Perchlorate decomposition. In this frame propellants with the same nominal composition (AP/ Al/HTPB 69/19/12) with a 0.2 % of iron replacing AP were tested in SPlab. The Aluminum was the usual Al-05 (see Table 2) and the AP was bimodal with 54,8 % 200 µm sized and 14 % in a size lower than 10 µm. Four different Iron oxides were tested, differing for size, shape and chemical composition, whose main characteristics are reported in Table 5. Note that the Iron Oxide labeled Nanocat® is the only purely nanometric one.

Table 5: Tested Iron Oxide powders

Powders Label	Size	Shape
Red 1	Slightly Submicrometric	Irregular
Red 2	Micrometric	Irregular
Monohydrate	Micrometric	Needle
Nanocat®	Nanometric	Round

The Monohydrate is yellow colored, because of the water molecule bonded, which has made the mixing of the propellants easier and more effective. The burning rate for

the Iron Oxides enriched propellants has been investigated in the set-up described in Fig. 2, and the results are reported in Fig. 25: one can immediately note that the reduced size of Iron Oxide labeled "Red 1" compared to "Red 2" provokes a thin increase in burning rate (close to 10 % at 50 bar). When the Monohydrate Iron oxide was used, no sensible difference was found on the ballistic behavior of the propellants: both the burning rate and the pressure dependency remain largely unmodified. A major burning rate increase can only be gained using the nanometric Nanocat®: at the pressure level of 50 bar, the burning rate of the propellant based on "Red 1", is enhanced by a factor close to 1.3. The pressure exponent is lowered strongly (≈ - 15 %). These characteristics were expected considering the low size of Nanocat® powders, which, in good analogy with nAl, makes it more energetic and easily reactive than standard, commercial, micrometric Iron Oxide. What is important to point out, anyway, is the similar behavior of all the micrometric (and slightly micrometric) Iron Oxides:

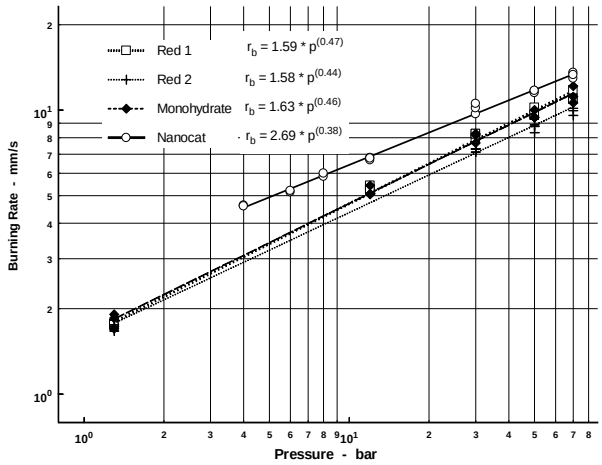

Fig. 25: Iron Oxides effects on propellants burning rate (SPLab, Donegà)

From Fig. 25 one can immediately note that the reduced size of Iron Oxide labeled "Red 1" compared to "Red 2" provokes a thin increase in burning rate (close to 10 % at 50 bar). When the Monohydrate Iron oxide was used, no sensible difference was found on the ballistic behavior of the propellants: both the burning rate and the pressure dependency remain largely unmodified. A major burning rate increase can only be gained using the nanometric Nanocat®: at the pressure level of 50 bar, the burning rate of the propellant based on "Red 1", is enhanced by a factor close to 1.3. The pressure exponent is lowered strongly (≈ - 15 %). These characteristics were expected considering the low size of Nanocat® powders, which, in good analogy with nAl, makes it more energetic and easily reactive than standard, commercial, micrometric Iron Oxide. What is important to point out, anyway, is the similar behavior of all the micrometric (and slightly micrometric) Iron Oxides: the burning rate and the pressure dependency are very close, and the slight differences encountered derive probably from different degree of purity, shape and chemical modification of the molecules. Size becomes important only when nanometric size is reached, thus reproducing, someway, what had been already asserted for nAl based propellants (see Fig. 14 and 15). Another effect of nanometric Iron Oxide was discovered when the high speed cinematography techniques previously described (see Fig. 7) were performed: the large population of spherical agglomerates visible on the burning surface when micrometric Iron Oxide was used (Fig. 26) was replaced by different shaped particles (usually in the form of irregular leaflets) which were to become spherical only at a certain distance from the burning surface (Fig. 27).

Fig. 26: Micrometric Iron Oxide based propellants spherical agglomerates at 1 bar (SPLab, Donegà)

Fig. 27: Nanometric Iron Oxide based propellants spherical agglomerates at 1 bar (SPLab, Donegà)

The corresponding grain size curve has shown the size being quite different too (Fig. 28): for all the pressure range investigated Nanocat® based propellant has produced lower agglomerates size compared to micrometric Iron Oxide one.

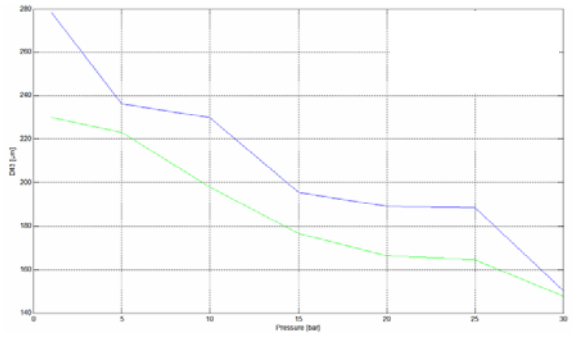

Fig. 28: Granulometric Curve Vs. Pressure for Red 1 and Nanocat® based propellants (SPLab, Donegà)

Once again the capability of nanosized ingredients to reduce agglomeration process and consequent specific impulse losses is evident. At the present stage of experimentation different recipes of propellants are being tested in SPLab making use of Nanocat® in higher percentage (up to 1 %, together with a 1 % of Monohydrate), all confirming the great advance in burning rate that is possible to obtain (+ ~ 30 %, with respect to a pure 2 % Monohydrate based), coupled with a massive pressure sensitivity reduction (- ~ 40 %). As a summary, at

the present stage of our experimentation, nanometric Iron Oxide seems to be a very promising agent acting vigorously as ballistic modifier.

CONCLUSIONS AND FUTURE WORK

Several nAl based propellants were compared to corresponding μAl based , both in terms of static and dynamic burning: all our tests have shown nanoaluminum to be very effective in burning rate enhancement and agglomerates size reduction. Moreover the nAl based propellants have shown a stronger resistance to forced extinguishment and quicker ignition, thus confirming the more energetic behavior, derived from the reduced flame-surface distance, of nAl combustion. Some remaining drawbacks (mainly concerning the lifetime and mixability) should not refrain potential users from exploiting the superior quality of nAl flames in rocket propulsion: the larger availability of these powders is making their price lower and lower, and at least a mixture of nAl with μAl could be used in applications. Of course, whatever result is eventually obtained, it should be validated by first small-scale and then full-scale motor fire tests. Besides nanoaluminum, nanometric Iron Oxide has been tested: the results has shown a performance enhancement in terms of burning rate, pressure sensitivity and agglomerates formation and size reduction. A dynamic behavior characterization of this Iron Oxide is planned for the near future in SPLab. Another plan of SPlab consists in testing new generation, generally coated, of nAl powders, coupled with small size oxidizers in order to reach the maximum burning rate. The high-speed recording techniques currently used in SPLab will be developed and automated.

ACKNOWLEDGMENTS

All ballistic analyses were carried out at SPLab of Politecnico di Milano, Milan, Italy. SEM, EDX, XPS, and XRD analyses were carried out at Istituto Guido Donegani (ENI Research Center), Novara, Italy.

The authors gratefully acknowledge the important support of the many SPLab students (Annalisa Conti, Saul Levi, Daniele Signoriello, Paolo Taiariol and Marco Galeotta) whose dedication and effort made this work possible.

REFERENCES

[1] Glotov, O.G., and Zarko, V.E.: "Condensed combustion products of aluminized propellants", Aeronautical and Astronautical Society of China, Vol. 34, No. 3, pp. 247-256, 2002.

[2] Lengellé, G., Duterque, J., and Trubert, J.F.: "Combustion of Solid Propellants", from Internal Aerodynamics of Solid Rocket Motor, Special Course at the Von Karman Institute for Fluid Dynamics, 27-31 May 02.

[3] Price, E.W., and Sigman, R.K.: "Combustion of aluminized solid propellants", *Solid Propellant Chemistry, Combustion and Motor Interior Ballistics*, AIAA PAAS, Vol. 185, edited by Yang, V., Brill, T.B., and Ren, W.Z., 2000, pp. 663-687.

[4] Glotov, O.G., Zarko, V.E., Karasev, V.V., and Beckstead, M.W.: "Effect of binder on the formation and evolution of condensed combustion product of metallized solid propellants", *28th International Conference of ICT*, Germany, Jun 97.

[5] Dokhan, A., Price, E.W., Sigman, R.K., and Seitzman, R.K.: "Combustion mechanism of bimodal and ultra-fine aluminum in AP solid propellant", AIAA Paper 2002-4173, 2002.

[6] Babuk, V.A., Vasilyev, V.A., and Malakhov, M.S.: "Condensed combustion products at the burning surface of aluminized solid propellant", *Journal of Propulsion and Power*, Vol. 15, No. 6, 1999, pp. 783-793.

[7] Babuk, V.A., Vassiliev, V.A., and Sviridov, V.V.: "Formation of condensed combustion products at the burning surface of solid rocket propellant", *Solid Propellant Chemistry, Combustion and Motor Interior Ballistic*s, AIAA PAAS, Vol. 185, edited by Yang, V., Brill, T.B., and Ren, W.Z., AIAA, 2000, pp. 749-776.

[8] Babuk, V.A., Vassiliev, V.A., and Sviridov, V.V.: "Propellant formulation factors and metal agglomeration in combustion of aluminized solid rocket propellants", *Combustion Science and Technology*, 2001, pp. 261-289.

[9] Duterque, J.: "Experimental studies of Al agglomeration in solid rocket motors", 4th International Symposium on Special Topics in Chemical Propulsion, Stockholm, Sweden, 27-31 May 96, pp. 693-705.

[10] Grigor'ev, V.G., Zarko, V.E., and Kutsenogii, K.P.: "Experimental investigation of the agglomeration of aluminum particles in burning condensed systems", *Combustion, Explosion and Shock Waves*, Vol. 17, No. 3, 1981, pp. 245-250.

[11] Kubota, N., "Propellants end Explosives, Thermochemical Aspects of Combustion" Wiley-Vch, Weinheim, Germany, 2002, pp. 164-165.

[12] DeLuca, L.T., *"*Burning of Aluminized Solid Rocket Propellants: from Micrometric to Nanometric Fuel Size*",* Invited Paper in Proceedings of the 2007 International Autumn Seminar on Propellants, Explosives and Pyrotechnics, Vol. VII, Edited by HUANG Ping, WANG Yajun, LI Shengcai, China Science Press, ISBN 978-7-03-020254-3, pp. 277-289.

[13] DeLuca, L.T., and Galfetti, L., Burning of Metallized Composite Solid Rocket Propellants: from Micrometric to Nanometric Aluminum Size*",* Invited Paper in Proceedings of 3rd Asian Joint Conference on Propulsion and Power (AJCPP), Gyeongju, Korea, 6-8 Mar 08.

[14] DeLuca, L.T., Galfetti, L., Severini, F., Meda, L., Marra, G., Vorozhstov, A.B., Sedoi, V.B., and Babuk, V.A.: "Burning of nAl Composite Rocket Propellants", *Combustion, Explosion and Shock Waves*, Vol. 41, No. 6, pp. 80-94.

[15] Colacarro, C.: "Caratterizzazione chimico-fisica e morfologica dei prodotti condensati di combustione di propellenti solidi per propulsione spaziale", MSc. Aerospace Engineering, Politecnico di Milano, SPLab, Milan, Italy, Jul 2006. (in Italian).

[16] Hermsen, R.W.: "Aluminum combustion efficiency in solid rocket motors". AIAA Paper 81-0038, 1978.

[17] Fedeli, C., and Giassi, D.: “Previsione del diametro d_{43} di agglomerati in combustione di propellenti compositi alluminizzati”, Advanced Space Propulsion, Spring Semester 2007.

[18] Baer, A.D., et Ryan, N.W., “Ignition of Composite Propellants by Low Radiant Fluxes”. AIAA Journal, Vol. 3, No. 5, p. 884, 1965.

[19] Inami, S.H., McCulley, L., and Wise, H., “Ignition Response of Solid Propellants to Radiation and Conduction”, Combustion and Flame, Vol. 13, Oct 1969.

[20] DeLuca L.T., Caveny, L.H., Ohlemiller T.J., and Summerfield, M., “Radiative Ignition of Double-Base Propellants: I. Some Formulation Effects”, AIAA Journal, 1976, Vol. 14, No. 8, pp. 940-946.

[21] DeLuca, L.T., Ohlemiller, T.J., Caveny, L.H., and Summerfield, M., “Radiative Ignition of Double-Base Propellants: II. Pre-Ignition Events and Source Effects”, AIAA Journal, 1976, Vol. 14, No. 8, pp. 1111-1117.

[22] Hermance, C.E., “Solid-Propellant Ignition Theories and Experiments”. In K.K. Kuo and M. Summerfield (Editors), Fundamentals of Solid-Propellant Combustion, AIAA, New York, Vol. 90, pp. 247-250, 1984.

[23] Lengellé, G., Bizot, A., Duterque, J., and Amiot, J.-C. “Ignition of Solid Propellants”, La Recherche Aérospatiale, No. 2, pp. 1-20, 1991.

[24] Merkle, C. L., Turk S.L. and Summerfield, M.: “Extinguishment of Solid Propellant by Fast Depressurization”, AIAA Paper 69-176, Jan 69.

[25] Dondé, R., Riva, G., and DeLuca, L.T.: "Experimental and Theoretical Extinction of Solid Rocket Propellants by Fast Depressurization", Acta Astronautica, Vol. 11, No. 9, 1984, pp. 569-576.

[26] Ciepluch, C.C., “Effects of Rapid Pressure Decay on Solid Propellant Combustion”, ARS J., Vol. 31, Nov 1961, pp. 1584-1586.

[27] Ciepluch, C.C., “Spontaneous Reignition of Previously Extinguished Solid Propellants”, NASA TN D-2167, 1964.

[28] Ciepluch, C.C., “Effect of Composition on Combustion of Solid Propellants During a Rapid Pressure Decrease”, NASA TN D-1559, 1962.

[29] Levi, S., Signoriello, D., Gabardi, A., Molinari, M., Galfetti, L., DeLuca, L.T., Cianfanelli, S., and Klyakin, G.F.: “Metallized Solid Rocket Propellants based on AN/AP and PSAN/AP for access to space”, Proceedings 2nd EUCASS, Brussels, Belgium, 01-06 Jul 07.

[30] DeLuca, L.T., Galfetti, L., Severini, F., Taiariol, P., Babuk, V.A., Kondrikov, B.N., Vorozhtsov, A.B. and Klyakin, G., “Ballistic Properties of Solid Rocket Propellants Based on Dual-Oxidizer (AP+AN) Mixtures”, Zeldovich Memorial II, 30 Aug – 03 Sep 04, Moscow, Russia.

[31] Vorozhtsov, A.B, Arkhipov, V, Bondarchuk, S, , N., Klyakin, G., Babuk, V., Kuznetsov, V., Sinogina, E., DeLuca, L.T. and Galfetti, L.: “Characteristics of Solid Propellants Containing Dual Oxidizer”, European Conference for Aerospace Sciences (Eucass), Moscow 2005.

[32] Babuk, V.A., Glebov, A. , Arkhipov, V.A., Vorozhtsov, A.B., Klyakin, G.F, Severini, F., Galfetti, L. and DeLuca, L.T.: “Dual Oxidizer solid rocket propellant for low-cost access to space”, 10th IWCP, Grafiche GSS, Bergamo, Italy, Nov 2005, paper 15.

Refractory ceramics for aluminum electrolyzers based on clay raw material

T. V. Vakalova, A. A. Reshetova, I. B. Revva, E. Yu. Egorova
Tomsk Polytechnic University, Tomsk, Russia

Abstract

The results of integrated studies of clay raw material of the Siberian Region are considered and recommendations are issued for evaluation of the quality of materials, which make it possible to identify the means of control of the main technological properties of clay rocks with the aim of bringing then to the required level. The results of developing compositions and technologies for barrier materials based on the products of concentration of refractory clay for cathode lining in aluminum electrolyzes are described. High-density dry barrier mixtures with different Al_2O_3–SiO_2 ratios (from 0.42 to 0.76) have been obtained, which can be used in two-layer linings for aluminum electrolyzers (in the high-alumina and silica layers).

KEYWORDS: clay rocks**,** clay mineral: kaolinite, montmorillonite, hydromica**,** chemical and mineralogical compositions**,** disordering of structure, aluminum electrolyzes, barrier materials alumina-silica refractory.

INTRODUCTION

Despite the increasing share of engineering ceramics based on synthesized materials in the total ceramic production, clay raw materials as yet are the most important for traditional materials, such as porcelain (household and electroengineering), all types of faience, sanitaryware, aluminosilicate engineering ceramics and refractories, etc.

Among clay minerals, the most common are kaolinite (and its analogs) and minerals of the montmorillonite and hydromica groups. Kaolinite minerals make up finely disperse components of the best-quality and the rarest clay rocks, i.e., white-burning (sometimes named "porcelain") refractory clays. Hydromica is the main clayforming mineral used for ceramic sanitaryware and is sometimes found in refractory clay as the second argillaceous mineral. The montmorillonite group minerals are at the basis of low-melting clay and loams that are used, as a rule, for ceramics with tinted crock, including construction ceramics.

The clay raw materials of Siberia are represented by all varieties of argillaceous rocks: kaolins, plastic and kaolinic refractory clays, high-melting clays, low-melting clays, and loams.

The depletion of domestic reserves of high-quality clays and kaolins forces the use of low-grade local clay rocks in the ceramic industry. The available resources of such low-melting argillaceous materials, including those in Siberia, make them important for production of tinted-crock ceramics.

EXPERIMENTAL RESULTS AND DISCUSSION

The diversity of argillaceous rocks and their different behavior in the technological process makes it necessary to predict and control their main technological properties, which is impossible without the detailed study of such rocks. The integrated evaluation of the clay materials implies the determination of some parameters such as chemical, granulometric, material compositions, structural specifics of the clay components, and physicochemical and technological properties. The material compositions of the argillaceous materials found in Siberia are indicated in Table 1.

Table 1 - The material compositions of the clay materials

Clay	Argillaceous and finely dispersed component (below 5 μm)		Non-argillaceous component (above 5 μm)	
	mineral	weight content, %	mineral	weight content, %
Refractory clays				
Troshkovskoe	Kaolinite and Halloysite Hydromica Free quartz Colloids	55,5 4,7 8,0 12,3	Quartz Feldspar Ferrous minerals Calcite and magnesite	10,0 6,0 0,9 2,5
High-melting clays				
Kailinskoe	Kaolinite Hydromica Free quartz	37,8 14,4 37,1	Feldspar Calcite Ferrous minerals	4,4 2,6 3,7
Low-melting clays				
Slyudyanskoe	Kaolinite, montmorillonite, Hydromica Free quartz	28,7 29,9	Feldspar Gypsum Magnesite Limonite	26,0 2,3 3,6 8,5

Clays are most frequently polymineral rocks and, accordingly, the chemical composition of clay (the gross chemical composition), although reflecting the specifics of the composition of all mineral components (argillaceous and non-argillaceous), does not always directly identify the types of minerals and their quantitative content. However, some components in the chemical composition make it possible to predict the specifics of the mineralogical composition and properties of the particular rock. For instance, when the content of Al_2O_3 is above 30%, it points to a prevailingly kaolinite composition of argillaceous rock; from 20 – 30%, to hydromica (if the clay is monomineral) or to a mixture of hydromica and kaolinite (when the argillaceous component is polymineral); and less than 20%, to montmorrilonite. The presence of Fe_2O_3 in quantities below 1% determines the white color of clay after firing, a quantity from 1 to 2% will impart yellowish tints to ceramics, and with the Fe_2O_3 content above 2% the color varies from yellow (3 – 4%) to red (above 4 %). The presence in the gross chemical composition of alkali metal oxides ($Na_2O + K_2O$) up to 1% with a prevailing kaolinite composition of finely disperse component will impede the process of clay sintering; when that content is over 1%, good sinterability is ensured while preserving high refractoriness.

The data on the granulometric composition of argillaceous rocks make it possible to identify the variety of argillaceous material (clay, loam, or loess) based on the ratio of sand, dust-like, and argillaceous articles and to predict its behavior in production. In particular, crack resistance and drying sensitivity of clays depend not only on their qualitative and quantitative mineralogical composition and the total content of natural grog (sand) particles, but also on the granulometry of these particles, since finely dispersed sand below 0,25 mm) stops fulfilling the grog function typical for silica rocks, compacts the plastic clay mixture, and complicates the process of moisture transfer in drying. Furthermore, the content of clay particles (smaller than 5 μm) can be used to predict the suitability of clays for producing ceramics by casting of aqueous suspensions into porous molds. The practice established that argillaceous rocks with not more than 40% content of clay particles sized below 0.005 mm are not suitable for slip casting without a special plastifying additive, which is represented by another more disperse and plastic clay. This is especially significant in developing mixtures for red-burning majolica based on local low-melting clay and loam.

Since nearly all argillaceous rocks have a complex (polymineral) composition of the fine (argillaceous) fraction, identification of the mineral type of argillaceous material is rather complicated, labor-consuming, and possible only using up-to-date physicochemical analysis methods that enable one with sufficient accuracy to identify individual argillaceous minerals belonging to different types, and even discrete particles or interlayer accretions in mixtures. However, when these argillaceous minerals belong to the same group, their identification becomes rather problematic. This is mainly true of such common refractory clay minerals as kaolinite and halloysite, especially if the latter is represented by varieties with different degrees of hydration.

The fullest review of the method of diagnostics for halloysite is given by Sand and Ormsby [1], who concluded that the x-ray phase method is unsuitable for analysis of kaolinite-halloysite mineral mixtures. Brindly et al. [2] established that even 30% kaolinite in the mixture totally masks the presence of halloysite on the diffraction pattern. Preliminary physicochemical treatment of clays by organic liquids (for instance,

impregnation with ethylene glycol or glycerin) expands the identification possibilities of thermal analysis, since they have been observed to form complexes with hydrohalloysite. This fact became the basis for qualitative determination of the presence of hydrohalloysite in mixtures with halloysite and kaolinite [3]. The invariability of the thermal effect position at 500 – 600°C during thermal analysis indicates that the sample is halloysite or kaolinite. This effect is splitted in two points to a mixture of hydrohalloysite with halloysite, or with kaolinite, or with both.

It has been reliability proved that the properties of clays are determined not only by their mineralogical compositions but also by the degree of crystallinity of clay-forming minerals.

A certain degree of disruption in crystallinity is typical of all argillaceous minerals. This is more typical of montmorillonite and to a lesser degree of the kaolinite group of minerals. Opinion exists that structural disordering of argillaceous minerals is mainly due to isomorphic replacement in the octahedral (in the case of kaolinite [4]) or tetrahedral or in both types of layers simultaneously (which is most typical of montmorillonite [5]) by oppositely charged ions, which weakens the hydrogen bonds between the gibbsite and silica layers.

It is found that disordering of the main clay-forming mineral to a large extent affects some physicochemical properties of clays (Table 2).

Table 2- Some physicochemical properties of clays

Parameter	Clay variety			
	Glukhovetskoe kaolin	Troshkovskoe clay	Zhuravlinyi Log kaolin	Kailinskoe clay
Clay-forming mineral	Kaolinite	Kaolinite and halloysite	Kaolinite and halloysite	Kaolinite and hydromica
Ordering index	0.90	0.38	0.86	0.30
Particle size, μm	1.00 – 1.50	0.10 – 0.75	1.00 – 1.50	0.10 – 0.50
Wetting heat, J/g: in natural state after disaggregation of particles	 5.45 5.45	 5.72 17.14	 5.30 5.30	 Not determ The same
Specific surface area, m^2/g	18	70	Not determ.	73
Total cation exchange capacity, mg -·equ. per 100 g Including: Ca^{2+} Mg^{2+} Na+	3.80 Not determ. The same -	19.52 14.39 4.80 0.30	6.51 3.60 2.72 0.14	16.70 12.50 3.60 0.60

In particular, the disordering of the kaolinite structure in Troshkovskoe kaolinic clays leads to disturbance of bonds around the aluminosilicon units, which together with isomorphic substitution inside the structure causes a shortage of positive charges, which is compensated by exchange cations Na^+, Mg^{2+}, and Ca^{2+} making up the exchange complex. However, the relatively low exchange capacity of minerals in the kaolinite group is accounted by disrupted bonds in the vertical planes parallel to the axis *c*; moreover, the more disordered the structure and the smaller the particle size, i.e., the lower the degree of crystallization of kaolinite, the higher is its exchange capacity, whereas in the case of montmorillonite minerals, the predominant reason for their increased cation exchange capacity is isomorphism in tetrahedral and especially in octahedral layers, which constitutes around 80% of the total exchange capacity [5]. Knowledge of the type of ionic exchange is especially important for controlling the plastic properties of clays and flow properties of clay suspensions, for instance, in thinning ceramic slip.

The disordering of the structure is also reflected in the behavior of argillaceous minerals in heating. It is noted in [10] that the DTA curves of kaolinite with a disordered structure typically have an exothermic effect within a temperature range of 50 – 200°C which is probably due to the extended surface of disordered kaolinite (up to 50 – 70 m^2/g), since it is known that the amount of adsorbed water for finely dispersed samples will be much higher and its role will be more significant. Furthermore, it is demonstrated in [6] that the more destroyed the particles are, the higher the peak of the low-temperature water removal. Moreover, the cation exchange capacity of disordered kaolinite increases with increasing specific surface area and the amount of molecular water bound by the exchange cations grows as well [7]. As for montmorillonite, the endothermic reactions on the DTA curves determined by dehydration by montmorillonite vary in intensity and process temperature depending on

the type of the substitution cation and the structural unit in which these changes are observed (the tetrahedral or octahedral positions). For instance, the more ferrous varieties (in which aluminum is replaced by iron in the octahedral layer) have a maximum below 600°C. Hectorite, which is rich in magnesium, stops releasing water at a higher temperature (around 800°C) than high-alumina montmorillonite.

The degree of ordering of the initial mineral structure influences the formation of mullite as well, i.e., the more ordered the structure, the easier is mullite formation, whereas the more defects emerge in the crystalline structure, the more the mullite-formation process is delayed.

The domestic and foreign practical experience indicates that the most important physicochemical and technological properties of argillaceous rocks depend not only on the qualitative and quantitative composition of their finely divided component, but on the composition of the non-argillaceous component as well.

Researcher É. A. Guber developed an original scheme for identifying material compositions of argillaceous rocks using a rational chemical analysis, which consists of the standard gross chemical analysis and additional chemical analysis of different extracts (aqueous, hydrochloric acid, soda, etc.) for the purpose of extracting total individual minerals or their characteristic part from clay.

According to this method, which has been widely tested in numerous studies, a direct analysis determines the chemical composition of the fine fractions, the quantity and composition of exchange cations, water-soluble salts, carbonates, the amorphous component (colloid minerals), and the amount of amorphous silica and free quartz. Using the results of direct measurements, the amount of hydromica is calculated based on the content of non-exchange potassium oxide, and the composition of the main argillaceous mineral is estimated. By subtracting all components obtained by direct measurements and calculations from the chemical composition of the fine fractions of clays, we obtain the quantity and chemical composition of the main argillaceous mineral in the fine fractions. This residue is converted to 100% and the molar ratio of Al_2O_3 : SiO_2 is determined. If this ratio is equal to 1 : 2, the mineral belongs to the kaolinite group; if the ratio is 1 : 4, the mineral belongs to the montmorillonite group. It is possible that this residue in a clay with prevalence of montmorillonite may have a ratio of Al_2O_3 : SiO_2 less than 4, which may happen when montmorillonite and kaolinite are present simultaneously or in the presence of such minerals of the montmorillonite group as beidellite, which contains less silica than other components of this group.

The type and structure of argillaceous materials are not the only factors that affect the properties of argillaceous rocks; according to contemporary concepts of the structure of argillaceous minerals and the material composition of argillaceous rocks, virtually all clays, besides the crystalline component, contain some x-ray-amorphous material.

There are data [8] on the formation of colloid shells around argillaceous particles, which can happen either due to the formation of gel-like products of decomposition of parental rocks in the course of clay formation, or as a consequence of disassociation and dissolution of the surface layer of the argillaceous particles in water, or water peptization of hydrophylic clay material.

Both silicic acid sol that is occasionally formed in weathering of feldspar and the surface sol emerging in peptization, whose chemical composition is close to that of argillaceous mineral, are capable of jelly- and gel-formation even with a relatively high water content, as a consequence of skeleton formation by adhesion of the less hydrophilic ends of the argillaceous particles or by adsorption of colloid particles on the surface of the crystallized argillaceous minerals. There was concluded /9/ that colloids are separated from the crystalline nucleus in heating the fine fraction of clay by a buffer mixture that consists of mixed aqueous solutions of oxalic acid and ammonium oxalate (the Tamm reactant).

These recommendations were used in clarifying the reasons for the kaolinity of some varieties of refractory kaolinite clays (in particular, nonplastic Troshkovskoe and Katomskoe clays). It was established that the lack of plasticity of theseclays in their natural state is due to the aggregating effect of the amorphous material which cements the clay particles intowater-strong aggregates, whose existence is corroborated byelectron microscopy. Analysis of the materials compositionof the colloids indicated that they contain 70 – 80% colloid aluminum hydroxide $Al(OH)_3$ and gel SiO_2, which in natural conditions exist in the form of aluminosilica gel due to coagulation of oppositely charged particles. Therefore, the properties of such coagulation gel and the strength of its bond to the crystalline nucleus will have a predominant effect on the properties of the argillaceous particle aggregates and finally determine the physicochemical and technological properties of clays.

In the case of the Troshkovskoe kaolinic clays, it is established that their argillaceous particle constitutes a complex aggregate consisting of a crystalline nucleus (kaolinite or halloysite particles with different degrees of hydration) surrounded by a colloid shell. The disordered structure of the argillaceous minerals determine the increased activity of the crystalline nucleus, which, according to the proposed model, takes the form of adsorption of the positively charged aluminosilica gel, which forms the finest shells around the crystalline nuclei (argillaceous particles) and which is firmly fixed due to electrostatic mutual attraction forces. This is presumably the reason for the fact that colloids cannot be isolated from kaolinic clays by simple elutriation.

Along with white-burning refractory and high-melting clays intended for porcelain and faience, low-melting clay and loam with tinted crock after firing are important for ceramics used in construction.

Extensive experimental material accumulated in studying loam materials in Siberia shows that nearly all these

rocks are surface loams with a diverse material composition. The mineralogical composition of the fraction over 1 mm has no significant qualitative distinctions; the prevailing minerals are nonplastic ones, such as feldspar (up to 70%), quartz (up to 20%), and others (up to 10%). The finely disperse fraction (below 1 mm) is mostly made up of argillaceous components: a mixture of montmorillonite group minerals in the form of beidellite (60 – 70%) and hydromica of the type of illite (2 – 13%), as well as colloids (14 – 28%), fine-disperse quartz (1 – 7%), and insignificant impurities of other minerals (mainly carbonates). As for surface loams it is established that despite their territorial remoteness, they have qualitatively the same material compositions. Furthermore, their main argillaceous mineral is a mineral of the montmorillonite group with the structural formula $\{3H_2O[(Na, Mg)_{0.02-0.14}Ca_{0.11-0.30}]_{0.15-0.39}\}(Al_{1.49-1.71}Fe_{0.18-0.44}Mg_{0.04-0.27})_2(Si_{4.0-3.51}Al_{0.49-0.0})_4(O_{10.45-9.13}OH_{2.37-1.51})_{12}$ and the lattice parameters a = 0.517 nm, b = 0.896 nm, and c = 1.50 nm. Isomorphic substitutions are registered in this mineral in both tetrahedral and octahedral layers; furthermore, the aluminum substitution for silicon in the tetrahedral layer in the amount of 3.51 for silicon and 0.49 for aluminum corroborates the opinion of R. Grim [9] who assumed the existence of a natural mineral with a significantly greater substitution than 3.80 and 0.20, respectively, which has been named beidellite. This mineral in Siberia loam represents a ferrous variety of the montmorillonite group mineral, which is in the phase of transformation from illite to montmorillonite.

In the general case, identification of the structural formula of the main argillaceous mineral makes it possible to predict the behavior of the analyzed rock in technological processing. For instance, the prevalence of Ca^{2+} cation among the exchange cations makes the montmorillonite rock virtually unswellable; in the case of a substantial replacement of the silicon cation Si^{4+} by Al^{3+} in firing one can expect the formation of spinel as one of the high-temperature phase instead of modifications of quartz; isomorphic replacement of Al^{3+} in the octahedral layer by Fe^{2+} and Mg^{2+}, the presence of four-coordination Al^{3+}, as well a substantial replacement of oxygen by the hydroxyl group increase the activity of clay in sintering.

Thus, in selecting argillaceous materials for particular technologies of ceramic production, one should be guided by the integrated evaluation of the properties of the argillaceous rock, such as microaggregation and granulometric and material composition, including the chemical and mineralogical compositions of the argillaceous and impurity components, the presence of amorphous material, and the state of ordering

of the clay-forming mineral structure. Knowledge of these properties will make it possible to identify ways of controlling the main technological properties of argillaceous rocks in order to bring them to the required level.

At present the fireclay were widely applied in producing both fine ceramics, particularly porcelain and faience, and in technologies of silica-alumina refractory for the black and colored metallurgy.

For example the service life and technical-economical parameters of electrolyzers producing primary aluminum to a large extent depend on the properties of refractoris used in cathode units, including barrier materials that serve as a barrier between the aluminum melt and the heat-insulating part of the electrolyzer base. Their main function is to lower the risk of emergency breakthrough of molten metal and electrolyte. Such barrier materials in contemporary electrolyzers are either molded as bricks and plates, or non-molded in the form of dry barrier mixtures and concretes of different chemicomineralogical compositions, mainly aluminosilicates.

It is assumed that when the electrolyte components penetrate into the barrier material, they react with aluminum oxides and form chemical compounds of the type of nepheline and albite, which creates an additional obstacle to further diffusion of chemically aggressive components into the electrolyzer base.

In addition to this main function, i.e., after impregnation with electrolyte to form high-melting compounds whose melting point is higher than that of the infiltrating electrolyte (1100°C in the case of albite and 1200°C in the case of nepheline), the mixture of aluminosilicate powders redistributes the cross-section profile of the charge by decreasing it near the peripheral joints and making it higher in the central part of the cathode unit.

Hence, it is evident that the main source of raw materials for barrier materials, regardless of their production method (molded or non-molded), are natural aluminosilicate rocks, i.e., refractory clays and kaolins.

Despite the growing demand for special refractories to be used in electrolyzers, the Russian industry has not yet implemented the production of dry barrier mixtures (DBM); therefore, producers mainly use foreign refractory mixtures, most frequently from China.

The present study evaluates the possibility of using kaolin to produce dry barrier mixtures similar in their composition and properties to imported DBM.

According to standard requirements, all barrier materials based on their chemical composition are divided into two classes: high-silica (albite-forming), including grades MTDPR-2 and DBM, and high-alumina (nephelineforming), including grades E-50, E-53, E-55, and MTDPR-1 (Table 3). However, regardless of the DBM type, the Al_2O_3:SiO_2 ratio in its chemical composition should be not more than 0.85 in order to provide high resistance to fluorides and aluminum melts.

Table 3 - Characteristics of Dry Barrier Mixtures

Parameters	DBM from Mayerton (China)				Grade "DBM" from Clayburn (Canada)
	E - 50	E - 55	MTDPR-1	MTDPR-2	
Weight content, %:					
Al_2O_3	40 – 45	30 – 35	35 – 42	23 – 28	26 – 32
SiO_2	50 – 55	55 – 60	55 – 60	57 – 64	60 – 65
Fe_2O_3	1 – 3	2 – 3	1 – 2	1 – 2	5 – 7
CaO+MgO	0.8	1 – 2	1.0	1 – 2	1 – 2
Al_2O_3/SiO_2	0.73–0.82	0.50 – 0.64	0.58 – 0.75	0.36 – 0.49	0.40 – 0.53
Density of deposited layer, g/cm^3	1.92	1.95	1.75	1.85	1.88
Thermal conductivity, (W/m·K)	0.59 (650°C)	0.35 (300°C)	0.50 (350°C)	0.50 (650°C)	0.59 (650°C)

The need to develop DBMs of both types is known from the practice of operating electrolyzers using nonmolded barrier refractories, which shows that the most preferable electrolyzer lining is a two-layer lining in which the first layer is a material with a high SiO_2 content and low infiltration and heat losses and the second layer is a high-alumina material with high resistance to the gaseous reaction products. The thickness of the DBM layer in this case is usually 30 – 210 mm.

The granulometric and chemical composition of raw kaolin indicates that the content of the clay fraction, i.e., kaolinite proper, is not more than 40%, and the remainder non-clay impurities. Another peculiarity of this kaolin is its increased content of pigment oxides (ferrous oxides and titanium dioxide up to 2.5%), thus requiring concentration, which at the same time stabilizes the chemical and mineralogical composition of the concentration products.

Industrial concentration of this kaolin is now implemented using the dry method. The kaolin concentration scheme combines drying, milling, and screening by fractions and yields four products of concentration produced by separation in three consecutively arranged cyclones and a bag filter, which differ in their granulometric and chemicomineral compositions and technological properties.

The increased content of SiO_2 and the relatively low content of Al_2O_3 in the chemical composition of cyclone concentration products are due to the presence of the finely milled quartz component from the stony inclusions (up to 25 – 30%), which raises the temperature of complete sintering of plastically molded products (> 1400°C).

In developing alumina-bearing DBM of types E-50, E-53, E-5, and MTDPR-1 it was necessary to add technical alumina to the concentrated kaolin in order to bring the total Al_2O_3 content to 35 – 45%; in developing silica-bearing compositions of types MTDPR-2 and DBM we added quartz sand milled to complete passing through a No. 0063 sieve.

Since the concentration products themselves sinter poorly and the technical alumina additive requires an even higher firing temperature, the goal of optimizing practical DBM compositions was to lower the firing temperatures of mixtures while ensuring the maximum possible density of fired material, since the rate of physicochemical processes between the lining and the melt in an aluminum electrolyzer depends not only on the chemical composition of the refractory, but to a great extent on its structure, in particular, on the permeable porosity, the specific surface area, and the prevalent pore size.

It is known that introducing an additive of easily sinterable plastic refractory clay to kaolin not only provides the required cohesion and moldability of ceramic mixtures, but also lowers the sintering temperature by about 100°C. In this context, the sintering component tested in out study was high-melting clay with the complete sintering temperature equal to 1250°C in quantities providing a required content of the critical oxides SiO_2 and Al_2O_3 in mixtures with kaolin. Furthermore, to activate liquid-phase sintering in high-alumina mixtures, we used such effective flux as nepheline sienite in quantities that do not significantly impair the refractoriness of the composite. Since one of the reason for choosing high-alumina barrier materials for aluminum electrolyzers is the formation of nepheline in the contact layer in the course of reactions with the products of electrolysis, it is assumed that the deliberately introduced additive of nepheline sienite will be an addition to the total nepheline content formed in service and thus will have a favorable effect on cryolite resistance of the barrier material.

The composition of ceramic mixtures was selected based on the principle of ensuring a preset chemical composition (Al_2O_3 : SiO_2). The sinterability of experimental compositions was estimated by consecutive firing of plastically molded samples within an interval of 1300 – 1450°C. The optimal compositions analogous to imported mixtures were selected from the data array (Table 4). The experiments made it possible to recommend a combined additive that has both sintering and mineralizing effect, contributes to lowering the firing temperature of aluminosilicate composite by 50 – 100°C, and yields a refractory ceramic material with water

absorption less than 5% at the firing temperature of 1300 – 1450°C (depending on the type of the DBM).

The phase composition of the developed materials was identified by x-ray diffraction analysis. The degree of synthesis of mullite and the transformation of the alumina and silica components were estimated based on varying intensities of the characteristic x-ray reflections of mullite with interplanar distance of 0.54 nm, cristobalite (0.404 nm) and residual quartz (0.334 nm) and corundum (0.384 nm). The reference standards for these minerals included mullite (the mullite standard), white electrocorundum (the corundum standard), raw vein quartz (the quartz standard) and quartz calcined at 1600°C (the cristobalite standard). The obtained data are given in Table 5.

Table 4- Component Compositions and Main Service Parameters of Optimal Barrier

Analog	Composition code*	Content of oxide, wt. %		Firing temperature, °C	Water absorption, %	Open porosity, %	Apparent density, g/cm^3	Refractoriness, °C
		Al_2O_3	SiO_2					
E-50	1^1	42.28	53.26	1450	6.2	13.5	2.17	> 1650
	1^1-s	42.84	54.80	1450	1.9	4.3	2.24	1550
E-53	11^1	38.7	55.4	1450	5.6	11.3	2.17	> 1650
E-55	3^1	32.8	57.7	1400	3.6	7.8	2.19	1600–1625
MTDPR-1	5^1	39.8	54.7	1400	6.6	14.2	2.15	> 1650
	5^1-s	37.2	53.8	1350	2.9	6.4	2.20	1500
MTDPR-2	9	28.9	64.5	1350	6.2	12.9	2.10	> 1600
DBM	10	29.2	64.2	1350	3.1	6.7	2.16	1600

Table 5 – Phase Composition of Developed Barrier Aluminosilicate Refractories (X-Ray Phase Analysis Data)

Analog	Composition code	Firing temperature, °C	Phase composition, %				
			Mullite	Quartz	Cristobalite	Corundum	Vitreous phase
E-50	1^1	1450	68.1	3.0	3.8	10.1	15.0
	1^1-s	1450	63.7	2.5	4.0	12.1	17.7
E-53	11^1	1450	59.3	2.9	4.1	8.5	25.2
E-55	3^1	1400	48.4	5.9	3.1	9.1	33.5
MTDPR-1	5^1	1400	66.0	2.9	2.7	10.6	17.8
MTDPR-2	9	1350	49.5	5.7	2.7	2.0	40.1
DBM	10	1350	40.7	6.4	3.8	-	49.1

It has been established that the total content of mullite in alumina (35 – 45% Al2O3) mixtures (E-50, E-53, E-55, MTDPR-1) in the amount ranging from 48% (E-55) to 68% (E-50) is ensured by the synthesis of primary mullite as a consequence of the reaction between Al_2O_3 introduced with the technical alumina additive and SiO_2 introduced via kaolin in the form of impurity quartz and formed as cristobalite in the destruction of kaolinite. In this case not more than 50 – 60% of initial Al_2O_3 participated in the reaction of mullite formation at 1400 – 1450°C, whereas the rest is transformed into corundum.

To estimate the porous structure of barrier materials, in particular, the distribution of pores and their sizes, two samples corresponding to the alumina DBM—mixture 1^1 (analog of E-50) and the silica type—mixture 10 (analog of DBM, Canada) was selected.

It is established that the unimodal curve of the pore size distribution in sample 1^1 points to the homogeneous porous structure of the sample, in which pores of size 1.6 μm prevail. As for the pore size distribution in the silica sample (mixture 10), the bimodal curve with two maxima for pore sizes 1.8 and 2.9 μm indicates the dimensional heterogeneity of its porous structure. However, in both cases the mean pore size meets the requirements imposed on barrier materials (not more than 10 μm).

The cryolite resistance and gas impermeability of DBMs serving in aluminum electrolyzers at the site of their

contact with melts and gaseous electrolyte components to a large extent depends on an appropriately chosen granular composition ensuring the densest possible packing of the chamotte particles. Taking into account theoretical data and requirements imposed on the fraction (5 – 3) mm — 25, (3 – 05) mm — 30, (0.5 – 0.1) mm — 25, below 01 mm — 20.

Fractionated material was prepared by milling sintered chamotte in a jaw crusher and in a ball mill.

In addition to the chemicomineralogical composition, degree of sintering, and refractoriness, a DBM has to be characterized from the aspect of its thermophysical properties, in particular, thermal conductivity. It is found that the thermal conductivity of mixture 1[1] at 200 and 600°C is equal to 0.45 and 0.59 W/(m K), and that of mixture 10 is equal to 0.41 and 0.63 W/(m K), respectively.granulometric composition of DBMs, the following composition for chamotte powder (wt. %) were selected:

CONCLUSION

Thus, the concentration products of kaolin based on their chemicomineralogical composition and properties meet the requirements imposed on barrier refractories. High-density DBMs with different Al_2O_3 : SiO_2 ratios (from 0.42 to 0.76) have been obtained, which can be used in two-layer lining of aluminum electrolyzers (the alumina and silicate layers). The compositions and properties of these DBMs correspond to those of known foreign analogs.

REFERENCES

[1] L. B. Sand andW. C. Ormsby, “Evalution of methods for quantitative analysis of halloysite – kaolinite clays,” in: *Clays and Clay Minerals. Pros. II, Nat. Conf. Publ.*, Washington, 1954.

[2] I. W. Brindly, P. Santos, and H. Santos, “Mineralogical studies of kaolinite – halloysite. Part I, Identification problems,” *Am. Miner.*, 48 (7 – 8) (1963).

[3] L. B. Sand and T. F. Bates, “Quantitative analysis of endellite, halloysite and kaolinite by DTA,” *Am. Miner.*, 38 (3 – 4) (1953).

[4] W. Worrall, *Clays and Ceramic Raw Materials*, Applied Science Publishers (1975).

[5] R. Grim, *Applied Clay Mineralogy*, New York (1962).

[6] M. F. Vikulova, *A Manual for Petrographic-Mineralogical Studies of Clays* [in Russian], Gosgeoltekhizdat, Moscow (1957).

[7] A. J. Keenan, R.W. Mooney, and L. A.Wood, “The relation between exchangeable ions and water adsorption on kaolinite,” *J. Phys. Chem.*, 55 (9) (1951).

[8] F. V. Chukhrov, *Colloids in the Earth’s Crust* [in Russian], Izd. Akad. Nauk SSSR, Moscow (1955).

[9] T.V. Vakalova, The nature “Cake” and plasticity of refractory clay from Troshkovskoe deposit. // Glass and ceramic s. - 1997. - № 11. - P. 23 - 26.

Production of ceramic pigments with anorthite structures using nepheline sludge

M. B. Sedelnikova and V. M. Pogrebenkov

Abstract

For the most part, industrial ceramic pigments are synthesized from reagent-grade salts or oxides [1]. The use of nontraditional material in the composition of pigments would make it possible to substantially reduce their production cost. We made ceramic pigments with anorthite structures using nepheline sludge. In the reaction to obtain pigments with anorthite structure, the chromophores were added to a mixture of nepheline sludge, natural mineral kaolinite, aluminum oxide and silicon oxide, ensuring the stoichiometric composition of anorthite. The pigments were fired at temperatures of 1000 –1200°C. They can be recommended to supplement pigments of spectral colours and of bulk coloring of ceramic pastes and glazes.

INTRODUCTION

The pigments are resistant to high temperatures and the effect of fluxes and glazes. For the most part, industrial ceramic pigments are synthesized from reagent-grade salts or oxides [1]. In addition to lowering the price of the pigments, problems of using nature raw-materials [2, 3] and no utilizable production wastes are solved and the raw-material base for synthesis of ceramic pigments is expanded.

Materials in a wide color range are now required in modern construction. However, stable color can only be obtained as a result of addition of relatively expensive ceramic pigments. Synthesis of stable pigments using inexpensive raw material, industrial wastes, for example, whose utilization is an important problem, could be a solution to this problem. It is likewise important to extend the palette of existing pigments.

It was reported in the literature [4] that ceramic pigments with the diopside $CaMgSi_2O_6$ and wollastonite $CaSiO_3$ structure were obtained from the waste from alumina production — nepheline sludge.

EXPERIMENTAL PROCEDURE

We made ceramic pigments with anorthite structures using nepheline sludge.

Nepheline sludge is the product of a complex, well regulated manufacturing process of processing natural nepheline-apatite ores and production of alumina, and the sludge is stable with respect to all properties [5]. Used nepheline sludge is now kept in dumps in large amounts, so that its subsequent processing is becoming a pressing problem. CaO and SiO2, corresponding to a molar ratio of CaO : SiO2 = 2 : 1 and constituting a total of 85 – 88%, are the basic chemical components of nepheline sludge.2 The other oxides (Al_2O_3, MgO, Na_2O, K_2O) can be considered as minor components which have little effect on the structure and properties of the pigments obtained. The chemical composition of nepheline sludge from the Achinsk Alumina Combine is as follows (%): 29.12 SiO_2, 3.67 Al_2O_3, 4.55 Fe_2O_3, 53.20 CaO, 1.45 MgO, 2.16 Na_2O, 0.90 K_2O, 4.96 calcination loss. The mineral composition of nepheline sludge is basically represented by dicalcium silicate, and calcium hydrosilicates, hydroferrites, etc., are present as minor phases. The presence of calcium and silicon oxides in nepheline sludge makes it possible to obtain ceramic pigments with anorthite structures in charge adjustment with the corresponding reaction:

$$2CaO\cdot SiO_2 + Al_2O_3\cdot 2SiO_2\cdot 2H_2O + SiO_2 + Al_2O_3 \rightarrow 2(CaO\cdot Al_2O_3\cdot 2SiO_2) \quad /1/$$

For synthesizing ceramic pigments, nepheline sludge was finely ground to a maximum residue of 2% on a No. 0063 sieve. Compounds of 3*d* elements: iron, chromium, nickel, and cobalt, added in the form of salts in the amount of 3.86 – 23.68% in oxide, were used as chromophores.

In the reaction to obtain pigments with anorthite structure, the chromophores were added to a mixture of nepheline sludge, natural mineral kaolinite, aluminum oxide and silicon oxide, ensuring the stoichiometric composition of anorthite.

The compositions of some pigments are reported in Table 1.

Table 1: The compositions of some pigments

Pigment	Mass content, %						
	nepheline sludge	kaolinite	SiO_2	Al_2O_3	NiO	CoO	Fe_2O_3
A1	29.46	44.18	13.46	11.26	3.86	-	-
A2	29.74	44.60	9.70	11.36	6.48	-	-
A3	30.45	45.66	0	11.64	13.27	-	-
A4	29.46	44.18	13.46	11.26	-	3.85	-
A5	29.74	44.60	9.70	11.36	-	6.48	-
A6	30.01	45.02	5.88	11.47	-	9.16	-
A7	28.21	42.32	12.89	10.78	-	-	7.88
A8	27.70	41.55	9.04	10.58	-	-	12.88
A9	27.19	40.79	5.83	10.39	-	-	17.17

The pigments were fired at temperatures of 1000 –1200°C.

RESULTS AND DISCUSSION

Since nepheline sludge already contains a small amount (4.55%) of iron oxide, the final colour of each pigment is due to the combinations of iron oxide and other oxides- chromophores.

For the synthesizing pigments, the optimum colour appeared at a firing temperature of 1100°C, and the pigments melted at higher temperatures. But for cobalt- and nickel-containing pigments, a temperature of 1200°C, at which the brightest colour formed, was optimum.

The pigments were applied on the ceramic articles as overglaze paints. The colour of the pigments and paints is given in Table 2. The pigments were stable in overglaze painting and almost did not change colour.

Table 2: Colour of pigments and overglaze paints

Pigment (Ion Chromophore)	Colour of pigment at firing temperature of 1100°C	Overglaze paints at firing temperature of 850°C
A1 (Ni^{2+})	Grayish-green	Mustard-yellow
A3 (Ni^{2+})	Olive-green	Brown
A5 (Co^{2+})	Light-blue	Blue - green
A6 (Co^{2+})	Dark-Blue	Blue
A7 (Fe^{3+})	Apricot	Red-brown
A9 (Fe^{3+})	Red-brown	Red-brown

The x-ray phase analysis showed (see Fig. 1) that the pigments had a complex composition: anorthite (d = 0.408, 0.320, 0.213 nm), mullite (d = 0.342, 0.221, 0.169 nm) were identified in them. The anorthite was the dominate phase (Fig. 1). Fig.2 indicated that the height of anorthite characteristic peaks (d=0.32 нм) increased when the temperature grew from 1100°C to 1200°C .

The colour index coordinates were made on an SF-18 spectrophotometer. The dominant wavelength and purity of the pigment tone were determined (Table 3).

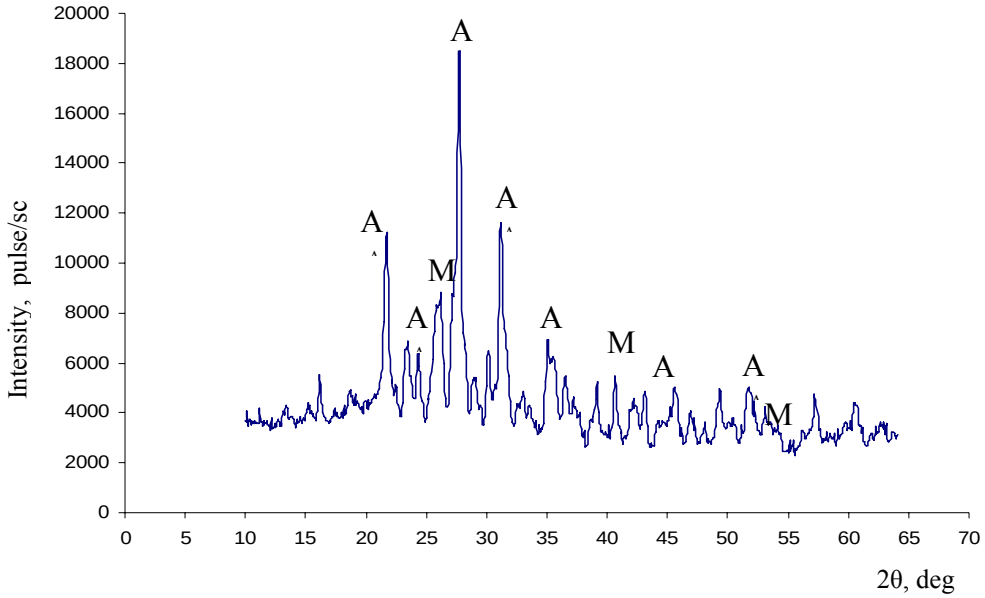

Fig.1 X-ray patterns of sample according to reaction /1/ at firing temperature of 1200°C, A – anorthite, M – mullite

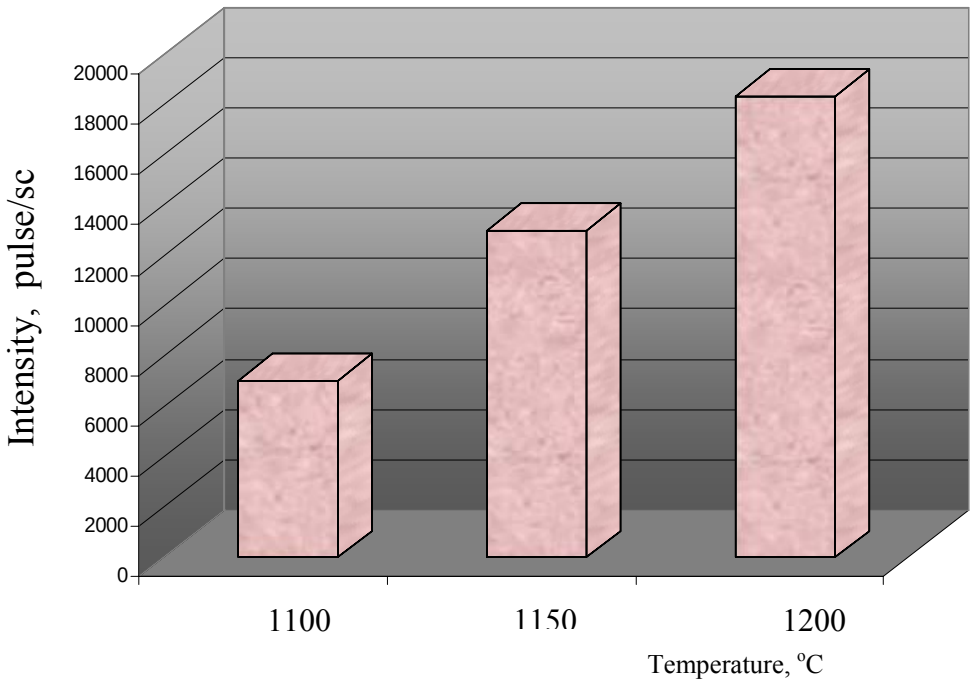

Fig.2 The changes of anorthite characteristic peak (d=0.32μm) depending on temperature

Table 3 Dominant wavelenths and purity of tone

Pigment	Chromaticity coordinates			Wavelength, nm	Purity of tone, %
	x	y	z		
firing temperature of 1100°C					
A3	0,37	0,38	0,25	575	31
A5	0,24	0,25	0,51	479	20
A9	0,48	0,34	0,18	608	47

CONCLUSION

Use of nepheline sludge for obtaining ceramic pigments with different crystal structures is thus economically expedient. The synthesized pigments are resistant to high temperatures and flux and glaze melts.

They can be recommended to supplement pigments of spectral colours and of bulk colouring of ceramic pastes and glazes.

The pigment compositions developed can be widely used for manufacturing coloured construction materials. In addition to reducing the cost of the pigments, problems of utilizing no utilizable production wastes can be solved and the raw-material base for synthesis of ceramic pigments can be expanded.

REFERENCES

[1] V. Pishch and G. N. Maslennikova, *Ceramic Pigments* [in Russian],Vysshaya Shkola, Minsk (1987).

[2] M. B. Sedel'nikova, and V. M. Pogrebenkov, "Production of ceramic pigments with diopside and anorthite structure using the gel method" *Steklo Keram.*, No. 8, 26 – 27 (2006).

[3] M. B. Sedel'nikova, and V. M. Pogrebenkov, "The effect of mineralizing additives on synthesis of ceramic pigments based on natural wollastonite" *Steklo Keram.*, No.1, 21-24 (2006).

[4] M. B. Sedel'nikova, and V. M. Pogrebenkov, "Production of ceramic pigments with wollastonite and diopside structures using nepheline sludge" *Steklo Keram.*, №10, 28-30 (2007).

[5] N. S. Shmorgunenko and V. I. Kornev, *Comprehensive Processing and Use of No utilizable Alumina Production Sludges* [in Russian], Metallurgiya, Moscow (1982).

Influence of mechanical activation on glass formation

O.V. Kazmina, V.I. Vereschagin, A.N. Abijaka

Tomsk Polytechnic University, Tomsk, Russia

Glass mixtures are a polydisperse composition of materials of various origins, the most refractory component of which is a siliceous one. In obtaining glass, a limiting stage of the entire glass manufacturing process is dissolution in the residual silica bath. Therefore, additional activation methods for the given kind of materials are still remained relevant problems.

As is known, amorphous variety of reagents interact significantly quicker than the crystal ones due to the excess of the internal energy. Therefore, the paper investigates the influence of mechanical activation of crystal siliceous materials on a degree of its possible amorphization and, consequently, on glass manufacturing processes.

The aim of the study was to determine the influence of mechanical activation of the glass mixture builder on glass manufacturing processes at temperatures up to 850^{o}C.

Natural fine silica flour was taken as a subject of research which does not need special crushing. Silica flour is a loose monogene crystal rock of sedimentary origin which corresponds to a weathering product e.g. of quartzite or silicified limestone. At that, the original dispersion of the rock allows to more accurately determine the influence of mechanical activation without a powerful effect superposition connected with the fine grinding of material.

Out of the known techniques of mechanical activation tested were variants of preliminary activation of original silica flour and co-activation of silica flour and soda mix. Mechanical activation of the investigated samples was provided by the vibrating mill 2014/B with vibrating crushing duration of 5 hours.

Structural processes caused by mechanical activation of silica flour were investigated by roentgen phase and IR-spectral analyses. The results of IR spectra (IR-Fourier Nicolet 5700) obtained in the infrared spectrum of 4000-400 cm^{-1} for the samples of original and vibratory crushed silica flour are given in Fig. 1, where spectra of anhydrous silicic acid (amorphous silica) are also shown.

As the chemical analysis of composited sample showed, silica flour consists of 95.7% of silica, up to 2% of Al_2O_3, and low quantity of such impurities as CaO, MgO, Fe_2O_3 with 1.0; 0.4; 0.27 mass%, respectively. As the roentgen phase analysis showed, the mineralogical makeup of silica flour is presented mainly by β-quartz and low kaolin. Granulometric structure of silica flour is characterized by high dispersion (Table 1).

Table 1. Granulometric structure of silica flour

Fraction size, μm	1 – 3	4 – 8	8 – 16	16 – 48	over 48
Quantity, %	22.5	31.3	35.2	9.7	1.3

Infrared spectroscopy procedure is one of in situ and exact methods of investigating matter structure which is very sensitive to different factors (sample preparation, survey conditions). Thus, the detection of separability in spectral bands which coincide or are situated rather closely is the important moment during the spectrum analysis. To detect separability an absolute degree of difference was analyzed with respect to wave number parameters. Spectral bands are considered to be indistinguishable

upon their simultaneous occurrence in materials in case the absolute degree of difference is less than 10 for both parameters. IR spectra of the samples under study (Fig. 1) demonstrate four conventional regions with the most significant absorption bands of 4000 – 3400; 3400 – 2000; 2000 – 1250; 1250 – 500 cm^{-1} which just underwent the comparative spectral analysis.

It has been detected that the outline of long-wave absorption bands (4000 – 3400 cm^{-1}) was substantially retained; absolute degree of difference did not exceed 10. In the given region a new absorption band occurs for vibratory crushed silica flour which is 3879.4 cm^{-1} and observed also on curves of amorphous SiO_2 that means occurrence of bonds characteristic for amorphous silica in vibratory crushed silica flour.

The main difference is observed in region of 3400 – 2000 cm^{-1}: all the five bands presented by the spectrogram of the original silica flour are absent that is probably connected with its surface amorphization. Occurred 3407.5 cm^{-1} band is similar to the absorption band of amorphous SiO_2 that speaks about their coincidence. Within the spectrum region 2000 – 1250 cm^{-1} all absorption bands along vibratory crushed silica flour samples are identical; absolute degree of difference is less than 10.

Special attention should be paid to region 1250 – 800 cm^{-1}, which is peculiar to group SiO^{4-}, therewith the given range of wave numbers is included in the region which is rather an individual spectrum of the given material. The main difference in this region is connected with another two absorption bands occurred in silica flour samples whose intensity is rather high: 1114.4 and 781.7 cm^{-1}; their absolute degree of difference does not exceed 10 for amorphous silica with absorption bands of 1105.3 and 800.6 cm^{-1}, respectively. This fact points to bonds peculiar to amorphous SiO_2 presented in vibratory crushed silica flour.

From the viewpoint of using short-living active states to increase mixture reactivity, the intergrinding of its components has definite advantages. This type of mechanical activation allows achieving both uniform distribution of the mixture components throughout the volume and mechanical intrusion of one matter into near-surface layers of the other. The effect of intrusion of fusible soda into the near-surface layer of silica flour can be regarded as a process of increasing reactivity of the refractory siliceous component.

Mechanical treatment of material is accompanied by the occurrence of point defects and accumulation of electrically charged centres when one can expect that formation of unlike charges on the surface of the mixture components will intensify this process. It was previously stated that the mixture components have unlike charges. This statement affirms the experiment carried out in connection with the mixture placement into the stationary electric field of 40kV. Upon this, fine particles of soda and dolomite accumulate on cathode while particles of sand on anode. After stirring in a mixer without wetting the mixture corresponds to weakly bound sintered sand particles on whose surfaces particles of fine dolomite and soda ash are retained by electrostatic forces. Obviously, silica flour and soda particles will be attracted during the process of grinding owing to non compensated unlike charges occurred on their surfaces.

IR spectra of vibratory crushed silica flour and soda mix and pure soda subjected to vibrating crushing are shown in Fig. 2. All materials were preliminary dried at temperature 115^{o}C until constant mass. The findings obtained allowed to detect that there were practically the same absorption bands on intergrinded samples of silica flour and soda as on IR spectra of separate silica flour and soda, excluding absorption bands of maxima at 3407.5; 2116.2; 1273.8 cm^{-1}, which are not present in the mix spectrum. Curves *a* and *b* are practically identical, as shown in Fig. 2, however, absorption bands characteristic for $(CO_3)^{2-}$ ion carbonate become wider and more fuzzy unlike narrow and intensive bands corresponding to the pure soda sample. Obviously, the difference between the given spectra is connected with the intrusion of soda into the surface layer of silica flour.

Results of roentgen phase analysis have showed that there is almost no any difference between silica flour activated separately from and in combination with soda. There is no amorphous halo

on radiograph of grinded materials. However, it is worth noting that relation of absolute intensity of maximum reflection corresponding to silica (d = 3.35 nm) to the background level intensity from the basic line in the area of small-angle scattering is approximately half as compared to non grinded silica flour that indirectly indicates amorphous phase occurrence.

To assess reactivity of mixtures activated by a vibrating mill at the similar time aging and different variants a comparative quality analysis has been carried out for the glass-ceramic material. The results of detecting the crystal phase amount (Table 2) showed that the mixture based on intergrinded silica flour and soda has the lowest crystal phase content while the mixture with non activated materials has the highest one. With the increase of temperature of the mixture treatment, the quality of crystal phase decreases, but the process of glass formation is more intensive in the mixture based on intergrinded materials, for all that.

Research findings assert the growth of chemical activity of mixtures based on intergrinded silica flour and soda that is depended on the area extension and the contact number between them. A comparison of IR spectra and diffraction patterns of the vibratory crushed original silica flour as well as that one of the amorphous silica data allow speaking about the presence of mechanical activation of crystal silica flour connected with its partial surface amorphization.

Table 2. Glass-ceramic product response

Mixture	Amount of crystal phase in material obtained at temperatures, %		
	750 °C	800 °C	850 °C
No mechanical activation	32	31	30
Mechanical activation of separate components	30	29	26
Mechanical co-activation of components	23	19	14

Thus, a preliminary mechanical coactivation of silica flour and soda allows obtaining an intermediate product with a glassy phase of no more than 85% at temperatures that does not exceed 850°C.

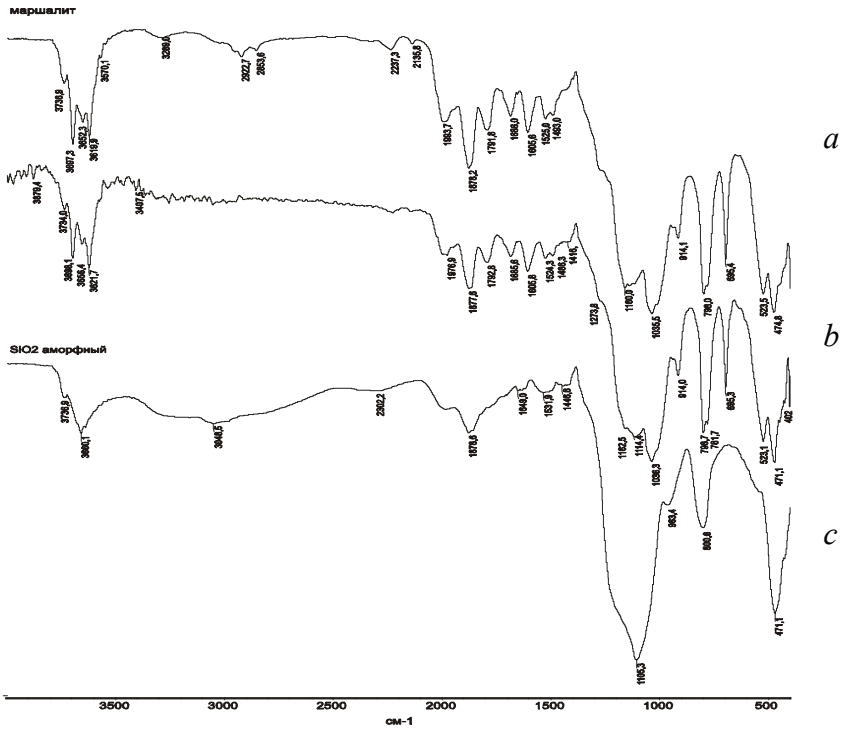

Fig. 1. Absorption IR spectra of: a - original silica flour; b - vibratory crushed silica flour; c - amorphous silica

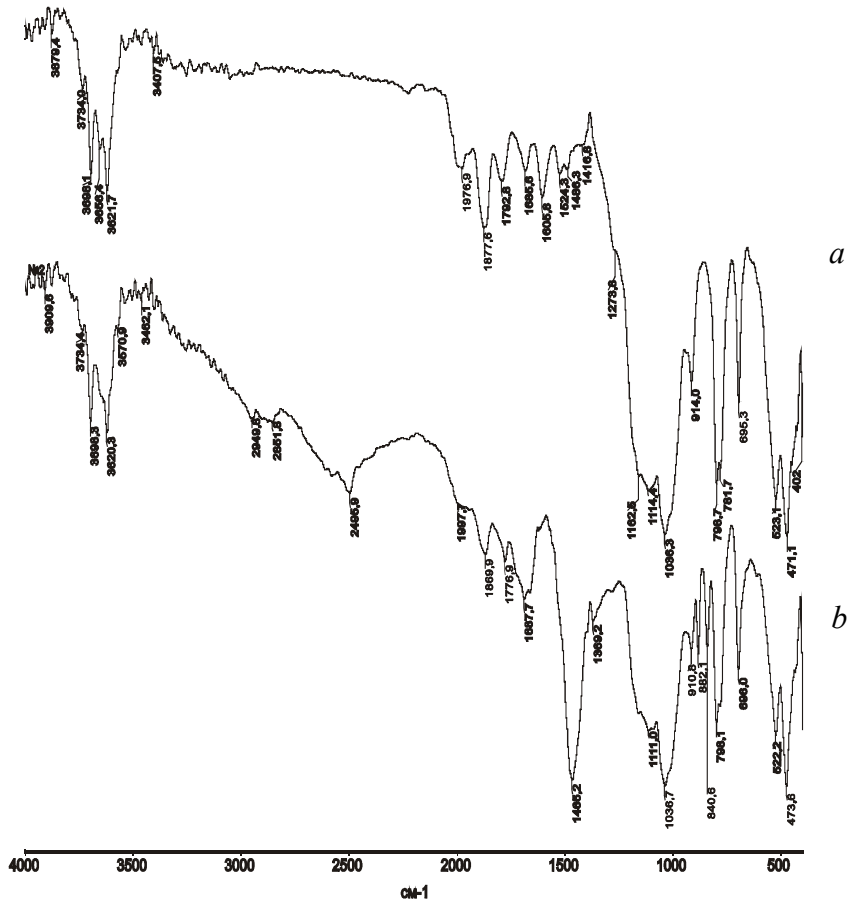

Fig. 2. Absorption IR spectra of: a - vibratory crushed silica flour and soda; b - vibratory crushed soda.

Characterization of Test Dust

Ulrich Teipel[1], Herbert Winter1, Alexander Ditts[2], Joachim Cäsar[3]

[1] Georg-Simon-Ohm Hochschule Nürnberg, Mechanische Verfahrenstechnik/ Partikeltechnologie, Wassertorstr. 10, 90489 Nürnberg, Germany
ulrich.teipel@ohm-hochschule.de

[2] Tomsk Polytechnic University, Department of Chemical Technology, 30 Lenin Str., 634050 Tomsk, Russland

[3] Fraunhofer Institut für Chemische Technologie (ICT), Joseph-von-Fraunhoferstrasse 7, 76327 Pfinztal, Germany

1 Introduction

For product qualification and quality assurance utilities, devices, frames or other assemblies have to undergo a protection class test. During this IP protection class test the test item that consists of mechanically moveable or electronic components has to be evaluated for its ingress protection against water or dust particles. Within the protection class IP 5X dusts may enter the equipment but mustn't interfere with the product function. However in the protection class IP 6X it has to be dust proof. Especially with regard to the durability the feeding properties and effects of the particles to the interior of the utility have to be examined more closely [1 -4]. Within this paper some of the dusts that are currently used for testing were examined regarding their particle size distribution, average particle size, particle density, bulk and tap density, specific surface area and morphology.

2 Materials

The above mentioned attributes of the following particle collectives respectively test dust were determined:

- Portland cement and fly ash (50 wt.%/50 wt.%) in accordance with DIN 40 050 – 9 [1]
- Portland cement
- Arizona dust "fine" in accordance with SAE J 726 [2] und ISO 12 103-1 [3]
- Arizona dust "coarse" in accordance with SAE J 726 [2]
- Test dust in accordance with JIS Z 8901 Class 8

3 Product properties and measuring methods

3.1 Particle density

Solid density and particle density respectively is a very important product properties that describes the mass per volume ratio. The solid density can be determined with a pycnometer [5]. For that the volume of the individually sample with known mass is metered with pressure measurement within a calibrated measurement chamber (Fig. 1).

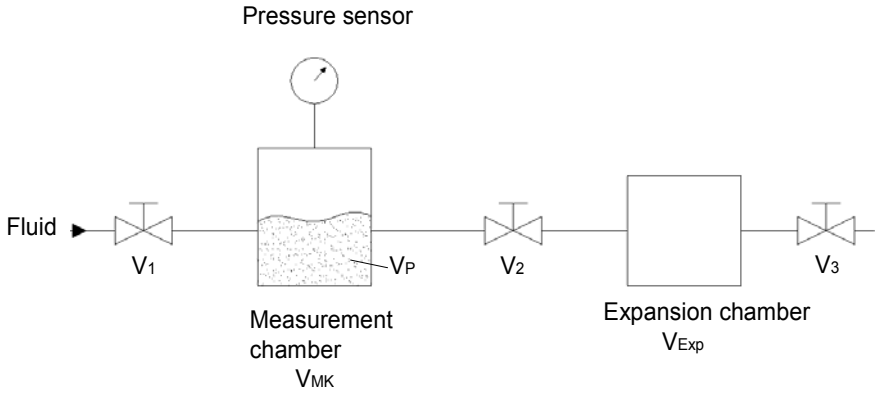

Figure 1: Schematic view of a pycnometer

With known sample mass the according volume is equal (1) and the density ρ_P can be determined.

$$V_P = V_{MK} - \frac{V_{Exp}}{\frac{\Delta p_1}{\Delta p_2} - 1} \qquad (1)$$

3.2 Bulk and tap density

Besides solid density the bulk and tap densities are other very important product properties In contrast to particle density the bulk and tap density contains information about the particle collective and the behaviour of the powders.

It applies for example that spherical particles due to their higher movability and lower affinity for arching take a higher place in the order of the system and have therefore a larger bulk density than irregular shaped particles. Therefore the bulk density is primarily depending on size, orientation of particles within the bulk, surface roughness, particle shape and the width of particle size distribution of the particle collective and contains further product properties of the testing material implicitly.

The bulk density is additively composed from particle density ρ_P and density of cavity filling fluid ρ_F according to volume share. The tap density is being determined by exposing the particle system to vibration for a given time slice [6, 7].

3.3 Specific surface area

The specific surface area of a discrete-disperse system can be calculated from measured particle size distribution or measured directly by photometric, sorption or permeation methods. With this measurement techniques different specific particle size distributions are being determined. While permeation methods are used to measure the outer surface area of a powder which corresponds approximately to the geometric surface (calculated from particle size distribution), the sorption methods are used to determine the inner surface area of a collective as well which is particularly eminent for porous particles. During flow through a fluid passes through the bulk particle and exposes it thereby to a certain resistance. This flow resistance is the higher the finer the powder is, i.e. the higher it's specific surface is the higher is it's flow resistance.
The specific surface can be determined with Eq. (2) which is based on the *Carman-Kozeny* equation:

$$S_V^2 = \frac{\Delta p \cdot \varepsilon^3}{L \cdot k_1 \cdot \eta_F \cdot u \cdot (1-\varepsilon)^2} \qquad (2)$$

where k_1 is the *Carman-Kozeny* constant, η_F is the dynamic viscosity of the fluid, Δp the pressure difference over the length of the packing L, ε the porosity and u is the fluid thoughput velocity.
The gas adsorption technique to determine the specific surface area is based on the adsorption of molecules from the adjacent gas or liquid phase onto the solid surface. The quantity of molecules adsorbed to the lower layer is only depending on the geometric shape of the surface. If the necessary amount of gas n_M to cover the monolayer and the required space A_0 of a molecule is known the mass specific surface area S_m can be determined with this Eq. (3):

$$S_m = \frac{n_M}{m} \cdot N_A \cdot A_0 \qquad (3)$$

Where N_A is the Avogadro number: $N_A = 6{,}023 \cdot 10^{23} \frac{molecules}{mole}$

For the calculation of the specific surface area it is necessary to qualify the adsorption process with the corresponding isotherm. A important model to describe the process is the multi layer adsorption model (BET - Isotherm) developed by Brunauer, Emmett and Teller (1938). See also [8-12].

The volume related specific surface area S_V can be calculated with the acquired mass related specific surface area S_m as follows (4):

$$S_V = \rho_P \cdot S_m \tag{4}$$

3.4 Particle size and particle size distribution

To measure the particle size and particle size distribution within this work the laser diffraction process was used. Laser light diffraction spectrometry is a method that determines particle size distribution based on the scattered light distribution, which originates from particle-light interactions, i.e., from the scattering that occurs as light waves expands through a particulate medium [13, 14]. Figure 2 schematically shows the laser diffraction process.

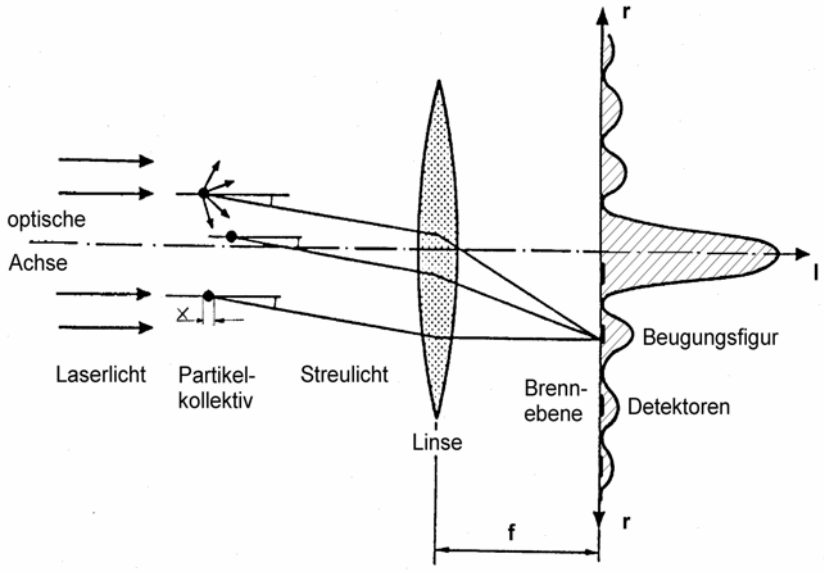

Figure 2: Basic design of the laser light diffraction spectrometer

The volume sum function $Q_3(x)$ and volume density distribution $q_3(x)$ were the result of the particle size analysis. The cumulative distribution $Q_3(x_i)$ represents the concentration of particles equal to or smaller than a given particle size x_i.

$$Q_r(x_i) = \frac{\text{Amount of particles } x \leq x_i}{\text{Total amount of particles}} \tag{5}$$

The density distribution $q_r(x_i)$ represents the amount of particles of a given particle size x_i, relative to the entire particle size distribution. Amounts that fall within a given particle size interval are referenced to the interval size:

$$q_r(\overline{x}_i) = \frac{\text{Amount between } x_i \text{ and } x_{i+1}}{\text{Interval size } x_{i+1} - x_i} \tag{6}$$

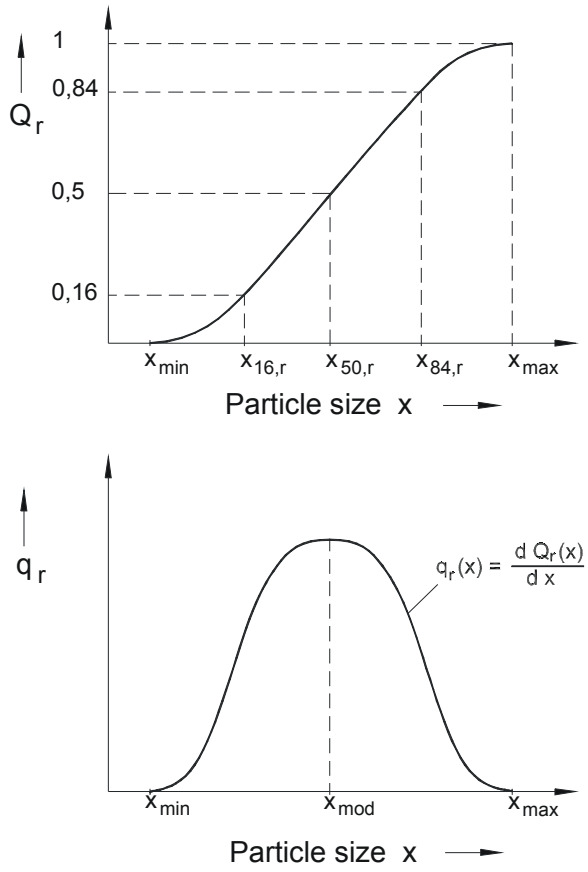

Figure 3: Cumulative distribution Q_r (x) ; density distribution q_r (x)

For characterisation of the particle collectives several parameters can be ascertained from the measured particle size distribution. The median $x_{50,r}$ represents the particle size valid for Q_r ($x_{50,r}$) = 0,5. This means that 50% of the total quantity of the collective are bellow this measure. The mode of the distribution is the particle size at which the density distribution $q_r(x)$ has a maximum. For spherical particles the volume based specific surface is:

$$S_V = \frac{6}{x} \qquad (7)$$

4 Results and diskussion

4.1 Portland cement und fly ash

DIN 40 050 part 9 clause 7.3.1 (IP protection class test for road vehicles) requires the test dust compound to consist of 50 wt. % unburnt Portland cement and 50 wt.% fly ash. In addition this norm demands the test dust to consist of 33 weight proportions $x \leq 32$ µm and 67 weight proportions $32\ \mu m < x \leq 250\ \mu m$.

Portland cement consists of approx. 58% to 66% calcium oxide, 18% to 26% of silicon dioxide (SiO_2), 4% to 10% Aluminium oxide (Al_2O_3) and 2% to 5% Iron(III) oxide (Fe_2O_3). Fly ash consists predominantly of Silicon-, Aluminium and Iron oxide. Details on product attributes of test dusts are not made within that norm.

The product properties of three charges (P1 to P3) of the test dust according to DIN 40 050 part 9 were determined the results are showed in the following Figures.

Sample	solid density	Bulk density	Tap density	$x_{10,3}$	$x_{5\ 0,3}$	$x_{90,3}$
	g/cm³	g/cm³	g/cm³	µm	µm	µm
P1	2,53	-	-	4,3	61,69	167,6
P2	2,54	1,33	1,74	4,3	55,63	167,4
P3	2,47	1,27	1,64	6,1	70,87	180,7

Sample	S_m *calculated*	*S_m Blaine*
	cm²/g	*cm²/g*
P1	1828	2838
P2	1852	2844
P3	1471	2740

Figure 4: Portland cement and fly ash

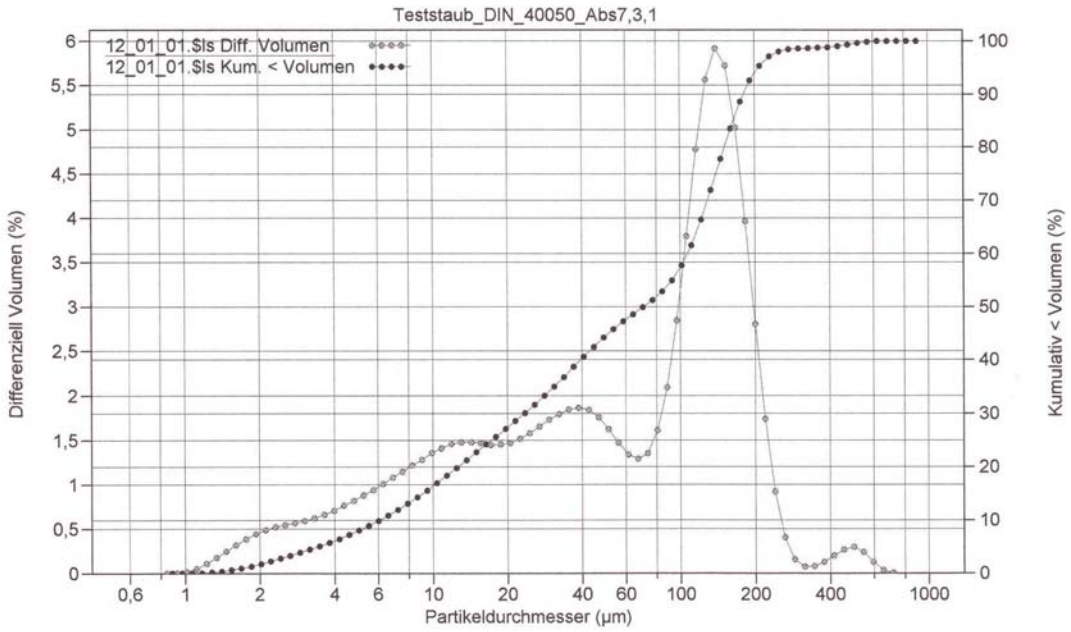

Figure 5: Particle size distribution (volume) Portland cement and fly ash (P3)

Figure 5 exemplary shows the volume sum - and volume density distributions of sample P3. At x ≈ 150 µm the distribution has a modal value. Furthermore it is apparent that it is a tri-modal distribution with the second modal value at x ≈ 40 µm and the third at x ≈ 14 µm. This characteristic is shown by all examined test dust samples according to DIN 40 050 part 9. The multi-modal characteristic of this sample can also be identified on the images taken by the scanning electron microscope (Figure 6).

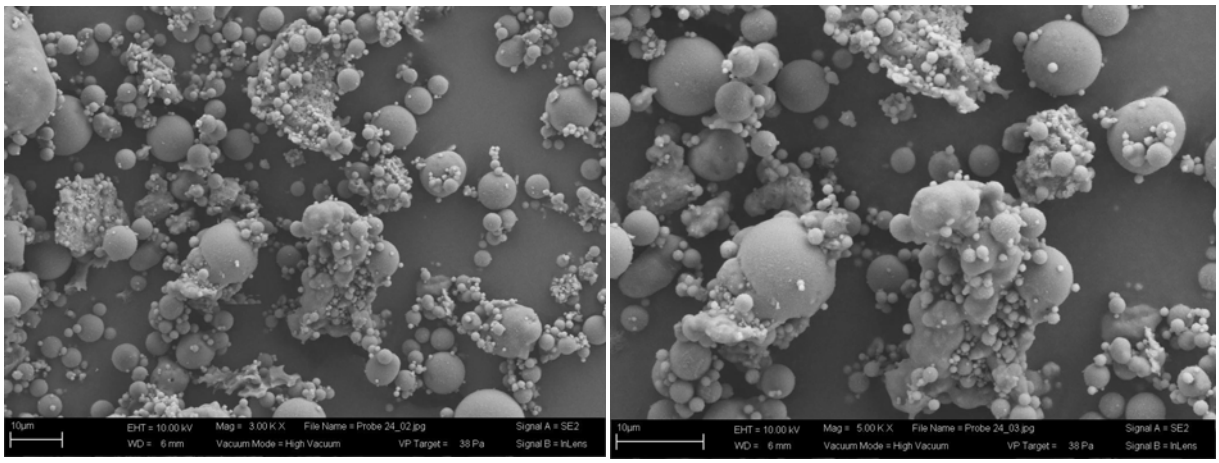

Figure 6: Portland cement and fly ash

The images show that the particle collective has an almost spherical shaped component and that a significant quantity of fine particles exists.

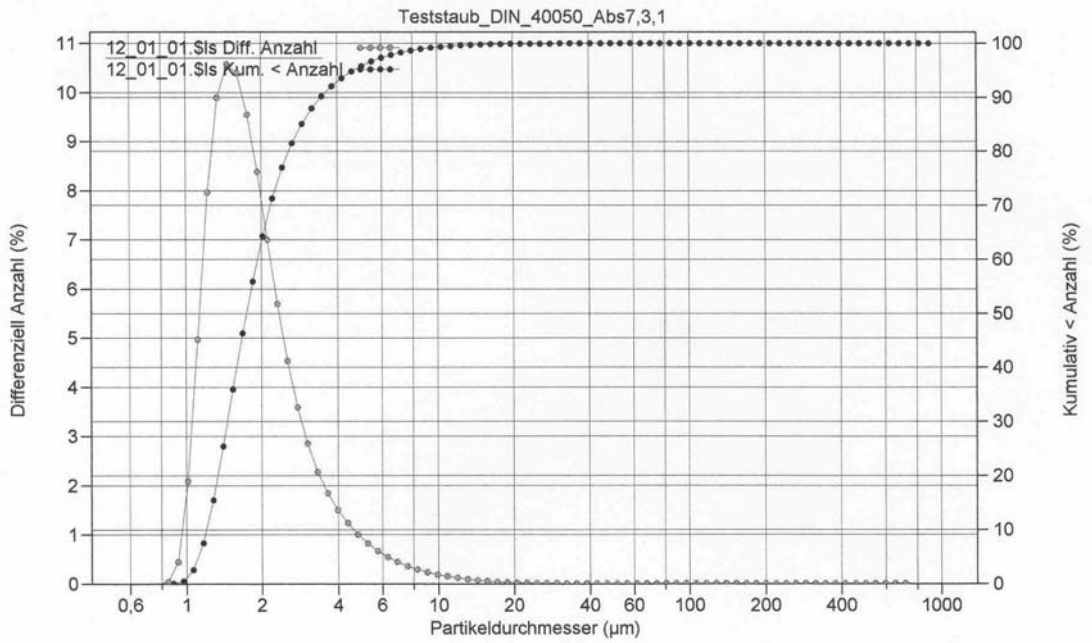

Figure 7: Particle size distribution (number) Portland cement and fly ash (P3)

4.2 Arizona dust

SAE J 726 Rev. June 93 demands synthetic manufactured dust for testing purposes with the following chemical composition:

Chemical composition	Percentage of weight
SiO_2	67 - 69
Fe_2O_3	3 - 5
Al_2O_3	15 - 17
CaO	2 - 4
MgO	0,5 - 1,5
Total Alkalis	3 - 5
Ignition Loss	2 - 3

Figure 8 Composition of Arizona dust

Furthermore SAE J 726 specifies a volume based particle size distribution within the size between 5,5 µm ≤ x ≤ 125 µm.

4.2.1 Arizona dust “coarse”

For the particle collectives P4 and P5 the following product properties were determined within the scope of this work.

Sample	solid density	Bulk density	Tap density	$x_{10,3}$	$x_{5\ 0,3}$	$x_{90,3}$
	g/cm³	g/cm³	g/cm³	µm	µm	µm
P4	2,86	-	1,64	3,33	40,22	129,65
P5	2,88	1.02	1,73	3,33	40,22	129,75

Sample	S_m *gerechnet*	*S_m Blaine*
	cm²/g	*cm²/g*
P4	1994	3087
P5	2001	3369

Figure 9 Arizona dust „coarse“

Figure 10 shows the volume sum – and volume density distribution of sample P4. It is also apparent that it is a bi-modal distributed product with a median particle size $x_{50,3}$ = 40,2 µm and a large fraction of coarse particles within the area of 90 µm as well as a large fraction of fine particles within the size of 2 µm ≤ x ≤ 15 µm.

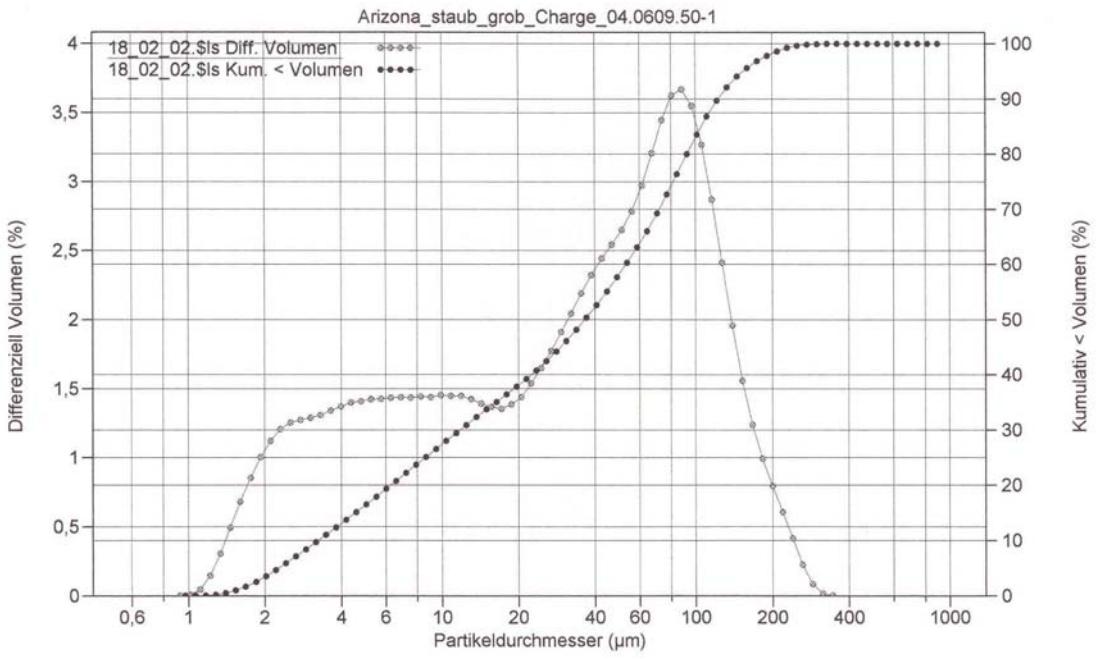

Figure 10: Particle size distribution (volume) Arizona dust “course”

At this point we’d like to point out that the coarse and fine particles included in the product have different impacts on the equipment under test if applied for dust test in the

environmental simulation. The maximum particle size of Arizona dust “coarse” is at $x_{max} \approx 280$ µm and thereby clearly above the demanded particle size of x = 125 µm.

4.2.2 Arizona dust „fine“

Another particulate product is intended within SAE J 726 Rev. Juni 93 Arizona dust “fine”. For the charges P6 to P10 the product properties were determined. These are displayed in figure 11. It gets especially apparent that the product properties of all the examined samples which were all taken from different containers do not show significant discrepancies.

Arizona dust “fine” shows a relatively wide distribution of size but does not posses a distinct multi modal system. The particles are within the size of 1,5 µm $\leq$ x $\leq$ 100 µm. The median size for sample P9 is $x_{50,3}$ = 10,8 µm. Figure 12 shows example images taken by an scanning electron microscope of samples P9 and P10. These images point out the width of distribution. It is apparent that a large percentage of particles with x = 20 µm is existent within the product which gets confirmed by figure 13.

Sample	solid density	Bulk density	Tap density	$x_{10,3}$	$x_{5\ 0,3}$	$x_{90,3}$
	g/cm³	g/cm³	g/cm³	µm	µm	µm
P6	2,95	-	-	2,44	10,8	39,12
P7	2,95	0,74	1,31	2,64	11,08	39,36
P8	2,95	0,73	1,30	2,36	9,51	38,83
P9	2,86	0,77	1,33	2,44	10,80	39,12
P10	2,97	0,74	1,34	2,40	10,83	39,44

Sample	S_m *calculated*	S_m *Blaine*	*S_m* Gasad.
	cm²/g	cm²/g	*cm²/g*
P6	3226	6262	6268
P7	3077	6227	-
P8	3523	6779	6835
P9	3366	6161	-
P10	3292	6498	6753

Figure 11: Arizona dust „fine“

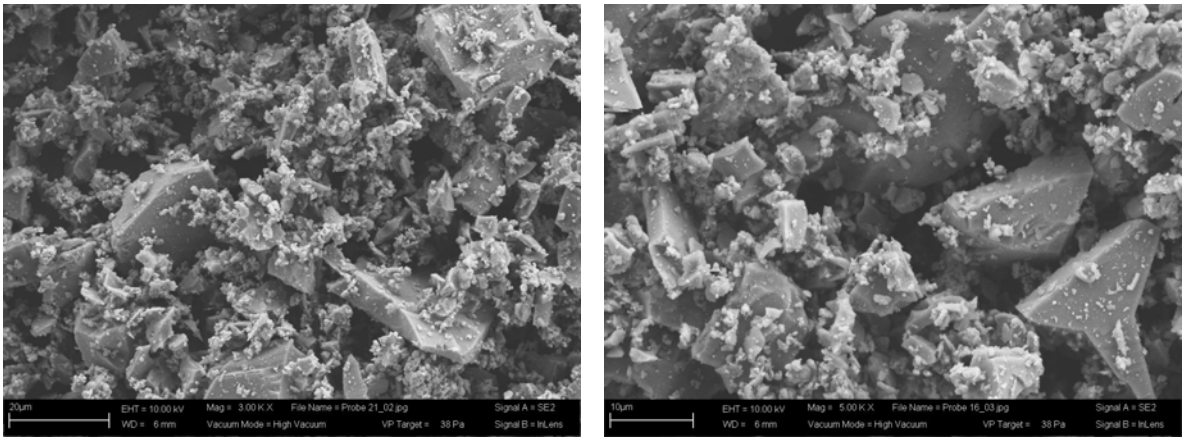

Figure 12: Arizona dust „fine“ (P9 and P10)

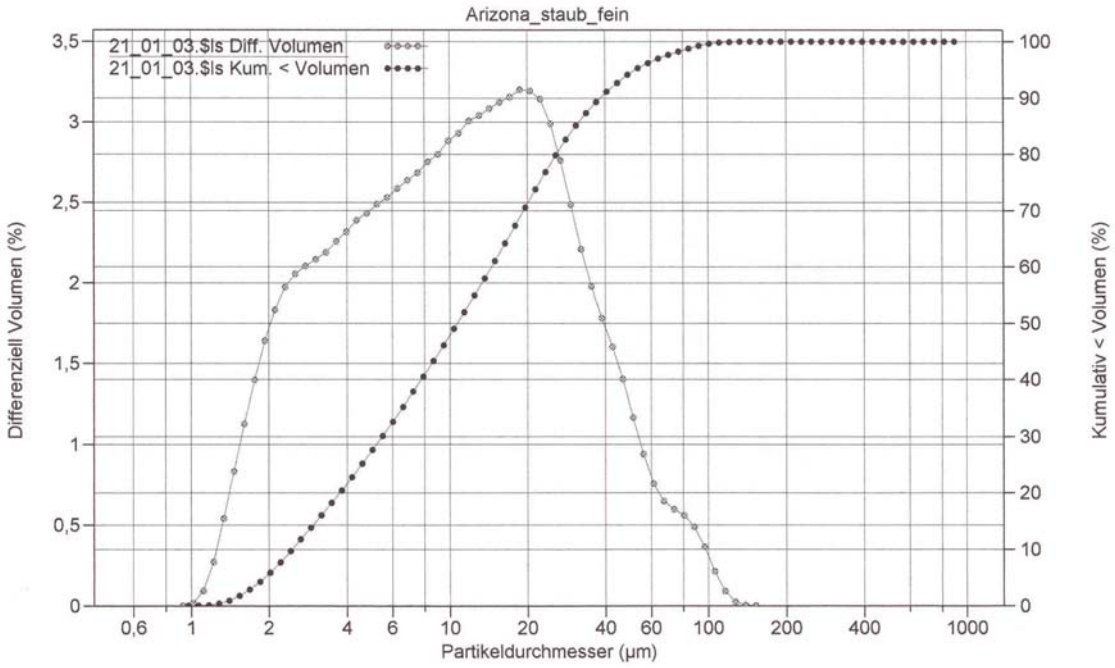

Figure 13: Particle size distribution (volume) Arizona dust “fine”

5 Literatur

[1] DIN 40 050 Teil 9: *IP Schutzarten, Schutz gegen Fremdkörper, Wasser und Berühren Elektrischer Ausrüstung*, 1999

[2] SAE J 726 Rev. Juni 93: Air Cleaner Test Code, 1993

[3] ISO 12 103-1: Road Vehicles-Test dust for filter, Part 1: Arizona test dust, 1997

[4] DIN EN 60529: Schutzarten durch Gehäuse (IP-Codes), 2000

[5] P. A. Webb; C. Orr: *Analytical Methods in Fine Particle Technology* Micromeritics Instrument Corp., Norcross, USA, 1997

[6] DIN EN 725-9: *Prüfverfahren für keramische Pulver, Teil 9: Bestimmung der Schüttdichte,* 1997

[7] DIN EN 725-8: *Hochleistungskeramik, Prüfverfahren für keramische Pulver, Bestimmung der Klopfdichte,* 1997

[8] DIN 66 131, *Bestimmung der spezifischen Oberfläche von Feststoffen durch Gasadsorption nach Brunauer, Emmett und Teller (BET)*, Grundlagen, in: DIN-Taschenbuch 133, *Partikelmesstechnik*, Beuth Verlag, Berlin, 1997; 96 - 99

[9] Brunauer, S.; Emmett, P. H.; Teller, E.: Journal of the American Chemical Society, 60 (1938) 309

[10] Allen, T.: *Particle Size Measurement*, Chapman and Hall Verlag; London, 1990, Chapter 16, 540 – 596

[11] Lowell, S.: *Introduction to Powder Surface Area*, Wiley&Son, New York, 1979

[12] D. Klank: *Bestimmung von Spezifischen Oberflächen unterschiedlicher Größenordnung,* In: U. Teipel (Ed.) Produktgestaltung in der Partikeltechnologie, Fraunhofer IRB – Verlag, Stuttgart, 2006, 545 - 558

[13] U. Teipel: *Energetic Materials: Particle Processing and Characterization,* Wiley –VCH Verlag, Weinheim, 2005

[14] U. Teipel: *Problems in Characterizing Transparent Particles by Laser Light Diffraction Spectrometry,* Journal of Chemical Engineering Technology 25 (2002) 1; 13 - 21